# KOBELCO TECHNOLOGY REVIEW

No. 35 Jun. 2017

***Feature-Ⅰ: Material Processing Technologies***
***Feature-Ⅱ: New Materials and Technologies for Automobiles***

## Contents

### Feature-Ⅰ Material Processing Technologies



### Feature-Ⅱ New Materials and Technologies for Automobiles





Published by

**Technical Development Group**
**Kobe Steel, Ltd.**

5-5, Takatsukadai 1-chome,
Nishi-ku, Kobe, HYOGO 651-2271, JAPAN
http://www.kobelco.co.jp

Editorial Office: **Shinko Research Co., Ltd.**
2-4, Wakinohama-Kaigandori 2-chome,
Chuo-ku, Kobe, HYOGO 651-8585,
JAPAN
Fax: +81-78-261-7843
E-mail: rd-office@kobelco.com

# Development of Steel Castings and Forgings for Vessels

Nobuyuki FUJITSUNA
Technical Development Dept., Steel Casting & Forging Div., Iron & Steel Business

*KOBE STEEL has been developing crankshafts, as well as other steel castings and forgings for ships, to make ships more energy efficient and reliable. This paper introduces technologies relevant to crankshafts, namely, super clean steel, technology for improving the fatigue strength of forged steel crank-throws and improved techniques of non-destructive inspection. Also introduced is the development status of highly strengthened intermediate shafts and high-strength steel for rudders.*

## Introduction

Kobe Steel produces steel castings and forgings, such as cast steel products for rudders, as well as forged steel products including intermediate shafts, propeller shafts and rudder stocks, with the main focus on crankshafts (**Fig. 1**).

Nowadays, the environmental regulations for vessels are being strengthened step by step, as seen in the regulations on $NO_x$/$SO_x$ and the introduction of the energy efficiency design index (EEDI),[1] promoting new ship designs as typified by eco-ships, hardware development, including new energy-saving engines, and low-speed cruising.[2]

With such trends in the vessel industry, we have been improving the quality of vessel components to contribute to the energy saving and reliability improvement of ships. This paper introduces the recent technological development on vessel components produced by Kobe Steel.

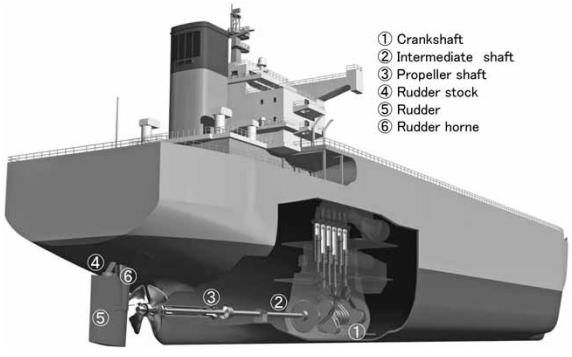


Fig. 1 Marine parts using casting and forging

## 1. Crankshafts

Diesel-engine crankshafts are positioned as one of the most important components and fall into the two categories of built-up type crankshafts for two-stroke engines (**Fig. 2**) and solid type crankshafts for four-stroke engines (**Fig. 3**).

Fig. 2 Built-up type crankshaft

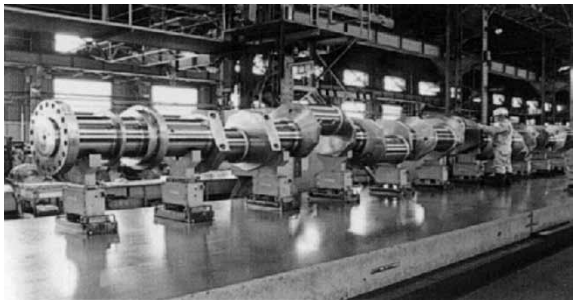

Fig. 3 Solid type crankshaft

### 1.1 Solid type crankshafts

Four-stroke engines employing solid type crankshafts are used for auxiliary machinery of onboard power generators, as well as for onshore power generators, and require crankshafts with high fatigue strength. The design fatigue strength of crankshafts used for marine diesel engines is stipulated by Equation (1) according to the unified rules (UR) of the International Association of Classification Societies (IACS): [3]

$$\sigma_{DW} = k \cdot (0.42\sigma_B + 39.3) \cdot \left(0.264 + 1.073D^{-0.2} + \frac{785 - \sigma_B}{4900} + \frac{196}{\sigma_B}\sqrt{\frac{1}{R}}\right) \quad \cdots (1)$$

$k$: process-dependent coefficient;
$\sigma_B$: tensile strength;
$D$: shaft diameter; and $R$; fillet radius.

The process-dependent coefficient ($k$) is given as 1.05 in the case of continuous grain flow (CGF) forging. The CGF forging includes RR forging and TR forging. **Fig. 4** shows the RR forging adopted by Kobe Steel.

The fatigue strength of materials is known to be affected significantly by the size of internal defects,

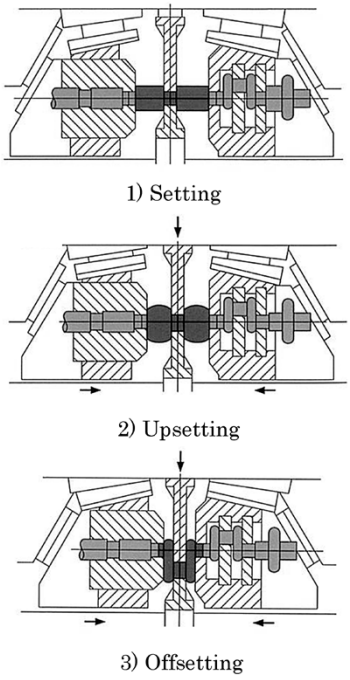


Fig. 4 RR forging

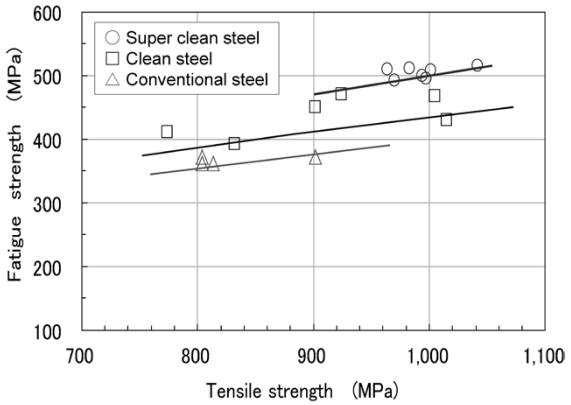


Fig. 5 Fatigue strength of super clean steel for solid type crankshaft

such as non-metallic inclusions, and to decrease with increasing defect size.[4] With the aim of reducing non-metallic inclusions that can become the origin of fatigue fracture, we have reduced impurities (S, O), optimized the refining conditions, and improved the ingot-making conditions, thus developing a super-clean technology.[5), 6] **Fig. 5** compares the fatigue strength of super-clean steel with that of conventional steel (tap degassing (TD) processed) and the currently-used steel (clean steel.) The super-clean steel exhibits a fatigue strength 20% or more higher than that of the currently-used clean steel and nearly 40% higher than that of the conventional TD processed steel. On the basis of these results, we applied to the classification societies for approval to use the value of $k$=1.15 for the k-factor in Equation (1) and have received approval for $k$=1.15 from all the classification societies. Consequently, it is expected that the use of crankshafts produced by the super-clean steel process would make possible an increase in the design fatigue strength and enable the manufacture of smaller engines with higher output. In addition, very-high-cycle fatigue characteristics of crankshafts are being evaluated from the aspect of long-term reliability, and the results that are being obtained indicate that the 40CrMo8 steel (tensile strength: 1,000MPa class) developed by Kobe Steel does not exhibit very-high-cycle fatigue fracture.[7)]

In addition, with the aim of achieving even higher fatigue strength, we are developing a high-strength steel with tensile strength of 1,050MPa or higher and technology for imparting compressive residual stress by cold rolling.

### 1.2 Built-up type crankshaft

Built-up type crankshafts are used for two-stroke diesel engines, the major machinery for rotating propellers; and each comprises a shaft portion, called a "journal," and an eccentric portion, called a "throw": these portions are assembled together by shrink fitting as shown in **Fig. 6**. For the sake of productivity, Kobe Steel has mainly used cast steel for throws and has worked on the improvement of material properties and reduction of internal defect, which is intrinsic to castings.[8), 9)] However, the company fully adopted forged steel throws in 2009 in response to anticipated future requirements for more stringent quality control and higher strength. Since then, technological development has been carried out to improve the productivity and quality of forged steel throws.

**Fig. 7** shows two methods of forging steel throws. A bending method, in which a plate material is folded by pressing, is commonly used to produce them; however, this forging method requires high-level skills, in ensuring symmetry, for example. Against this backdrop, Kobe Steel developed a die forging method. In die forging, a round slice of bar material is inserted into a die. As a result, the stock material is confined in the die to form crank webs in backward extrusion. This newly developed forging method is independent of skill and stably produces near-net shapes with high symmetry, while significantly improving the productivity. **Fig. 8** shows the cross-sectional macrostructure of a throw produced by this die forging (hereinafter referred to as a "die-forged throw.") The symmetry is excellent and no grain flow is observed in the fillet. A dark portion of a grain flow corresponds to microsegregation, in which an alloying element is concentrated, and is prone to form inclusions.

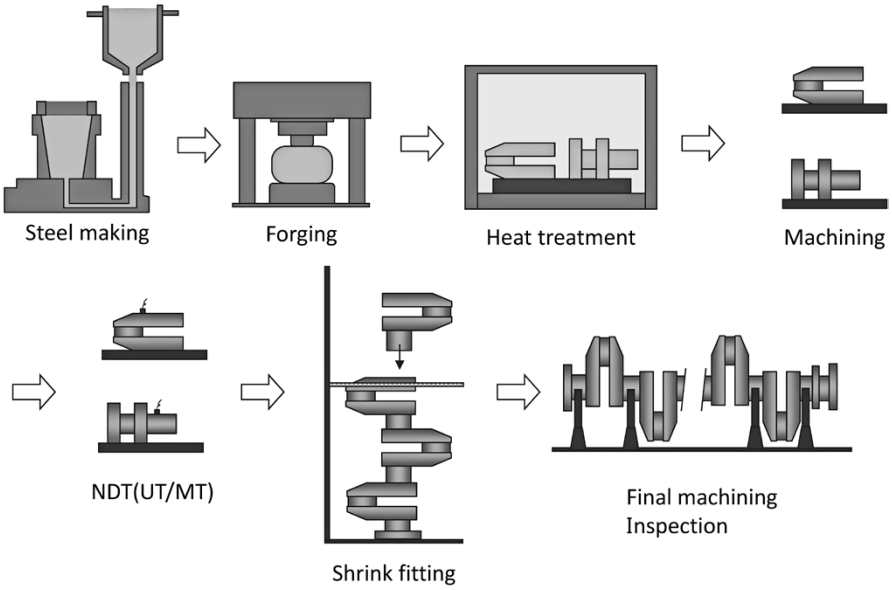


Fig. 6 Manufacturing of built-up type crankshaft

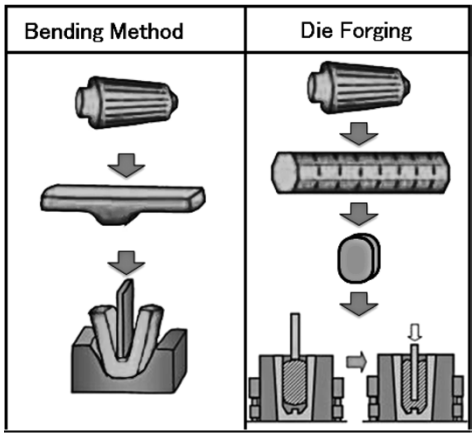


Fig. 7 Forging method of crank-throw

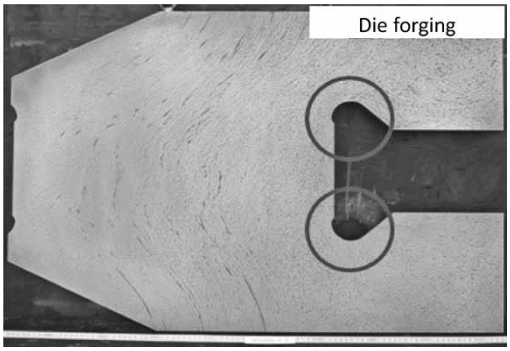


Fig. 8 Cross section of throw made by die forging

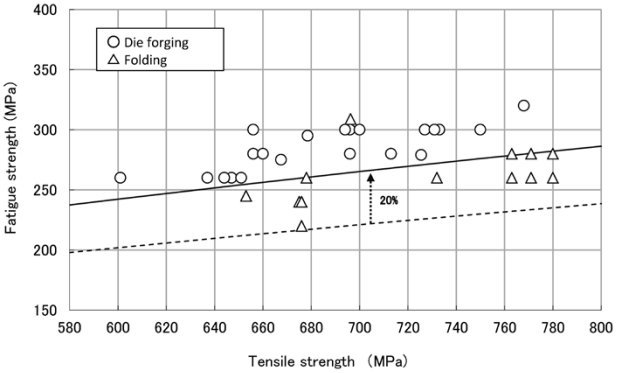


Fig. 9 Fatigue strength of forged throw

Because of the forging method, the fillet of a die-forged throw has no grain flow crossing there and is formed of a highly-clean portion without an inclusion due to microsegregation. It can be said that an effect is exerted that is similar to that of the CGF forging in solid type crankshafts. **Fig. 9** shows the result of a fatigue test on a die-forged throw, in which sulfur (S) has been reduced to improve the cleanliness. Also shown in the figure is the result of a test on a fold-forged throw. Including the effect of reduced sulfur, the die-forged throw shows an approximately 20% improvement over the fold-forged throw. On the basis of this result, we have obtained special approval for a k-factor of $k$=1.05 in the equation of the fatigue strength calculation (Equation (1)) from Class NK (Nippon Kaiji Kyokai), the ship classification society of Japan.

In the case of the grades of steel used for built-up type crankshafts, a smaller crankshaft having a cylinder diameter of approximately 400mm or less uses low alloy steel with a tensile strength of 800MPa, while a medium or larger sized crankshaft having a cylinder diameter of approximately 500mm or greater mainly uses carbon steel. This is due to the fact that, in the case of built-up type crankshafts produced by shrink fitting, low alloy steel has a higher risk of quenching cracks as the throw becomes larger in size. Therefore, we are working to develop a low alloy steel that can achieve higher

productivity.

### 1.3 Non-destructive testing technology for crankshafts

In order to secure the reliability of a crankshaft, its internal quality must be stringently controlled, and this is particularly so for its fillet, to which high stress is applied. This requires a well-established inspection technology. The conventional method has been ultrasonic inspection using manual scanning probes. Meanwhile, we have developed[10), 11)] and adopted automatic ultrasonic inspection systems for built-up type crankshafts and solid type crankshafts.

**Fig.10** shows the scanning system for an automatic ultrasonic inspection system for the throws of built-up type crankshafts. This system comprises a pin scanning unit (Fig.10 (A)) and a fillet scanning unit (Fig.10 (B)), wherein these two units are coupled by a roller chain so that they can be fixed at positions opposing one another at 180 degrees with a pin in the middle. In this configuration, the units can automatically run (rotate) around the pin to detect flaws. The pin scanning unit includes an oblique angle probe for detecting near-surface layers and a vertical probe for detecting deep portions, wherein the unit reciprocally scans in the axial direction of the pin. The fillet scanning unit includes an oblique angle probe having a convex curved surface that fits along the rounded portion of a fillet and an oblique angle probe for detecting flaws in the linear slope, wherein the unit scans the area predetermined for each fillet type in a playback manner. The flaw detection units for both pins and fillets move at a constant pitch along the circumferential direction at the end of one scan and complete the flaw detection of the entire area of a pin and fillet by making one round. In terms of defect detectability, the system can detect a flat bottom hole (FBH) with a diameter of 1.0mm.

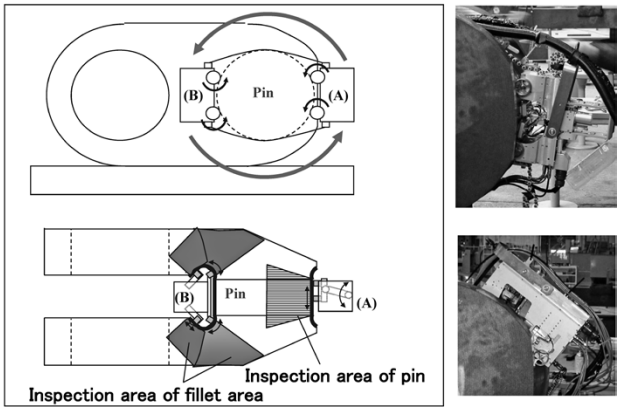


Fig.10 Scanning system for automatic ultrasonic inspection of throw

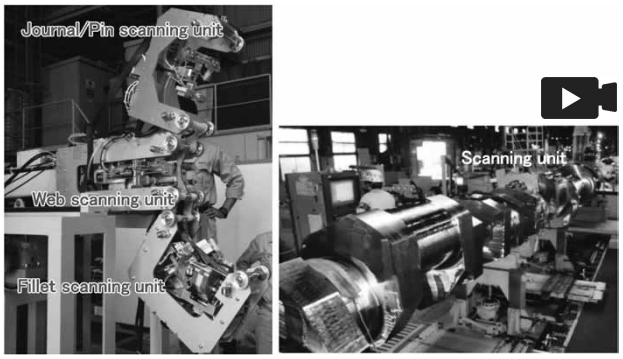


Fig.11 Scanning mechanism of automatic ultrasonic inspection for solid type crankshaft

For solid type crankshafts, we have developed an automatic ultrasonic inspection system with a resolution that can detect an FBH with a diameter of 0.5mm.[11)] **Fig.11** shows the scanning mechanism of the newly developed system and the system in operation. A scanning head includes a unit for scanning the parallel portions of pins/journals, a unit for scanning fillets and a unit for scanning throw arms, and carries out the inspection while tracking and rotating around the crankshaft. The fillet scanning unit of this system includes a plurality of ultrasonic transducers arranged in an array and adapts a phased array method, which can generate various ultra sonic pulses.

These automatic ultrasonic inspection systems are connected to a computer system, in which data are stored as digital data to ensure the traceability, including the confirmation of defects in a relevant crankshaft.

## 2. Intermediate shafts

Intermediate shafts transmit engine output to propellers. Since they are subjected to vibrations from engines and vibrations associated with propeller motion, they are required to have excellent torsional fatigue strength. The diameter of an intermediate shaft is calculated in accordance with Equation (2) defined by classification rules, and the maximum tensile strength usable is stipulated not to exceed 800MPa.[12)]

$$d = F \cdot k \cdot \sqrt[3]{\frac{P}{n_0} \cdot \frac{1}{1-\frac{d_i^4}{d_o^4}} \cdot \frac{560}{\sigma_B + 160}} \quad \cdots\cdots\cdots\cdots\cdots (2)$$

where F: constant depending on the types of shaft components;

$k$: shape factor;

$n_0$: revolution per minute; $p$, rated power;

$d_1$: diameter of the shaft center bore; and

$d_0$: shaft component diameter.

Although the reasons for setting the upper

limit of tensile strength at 800MPa is not clear, it is assumed to be attributable to the fact that the torsional fatigue strength in the region beyond 800MPa had not been clarified. Against this backdrop, we evaluated the torsional fatigue characteristics of 40CrMo8 steel, which was developed by the company and has achieved results in solid type crankshafts. As shown in **Fig.12**, it has been confirmed that the torsional fatigue strength exhibits no reduction and increases proportionally with the increase of tensile strength. Also confirmed was that the notch sensitivity and the safety factor stipulated by classification rules against vibration stress are equivalent to those for conventional steel.[13)]

On the basis of these results, the Class NK (Nippon Kaiji Kyokai) approved the use of the 40CrMo8 up to 950MPa grade for the strength calculation. In addition, via the Class NK (Nippon Kaiji Kyokai), the IACS added APPENDIX I to UR M68 in April 2015 to provide special approval for using the alloy steel having a strength between 800MPa and 950MPa as the material for intermediate shafts.

An intermediate shaft with increased strength is expected to increase the engine output and to reduce the number of or eliminate vibration suppression devices, because the material strength is increased without changing the shaft diameter as shown in **Fig.13** (A), and the allowable vibration stresses ($\tau_1$, $\tau_2$) are raised. Also, a shaft diameter reduced by increased strength results in a lower natural frequency for a given engine output, which is considered to shift the barred range towards the low rotation side (Fig.13 (B).) In the figure, the speed ratio, $\lambda$, of the horizontal axis represents the ratio to the rated maximum revolution (revolution/rated revolution.) As a result, it is considered that the normal revolution can be reduced while providing an extra margin for low-speed cruising.

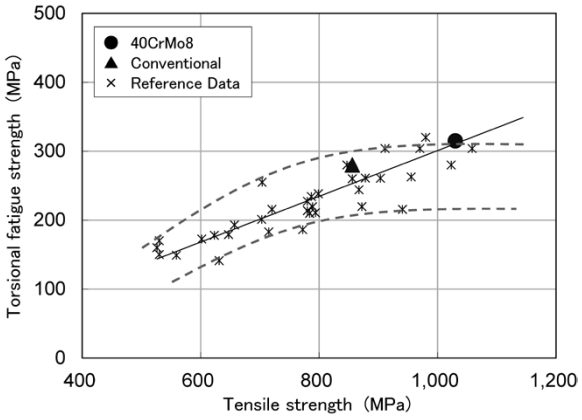


Fig.12 Relationship between tensile strength and torsional fatigue strength

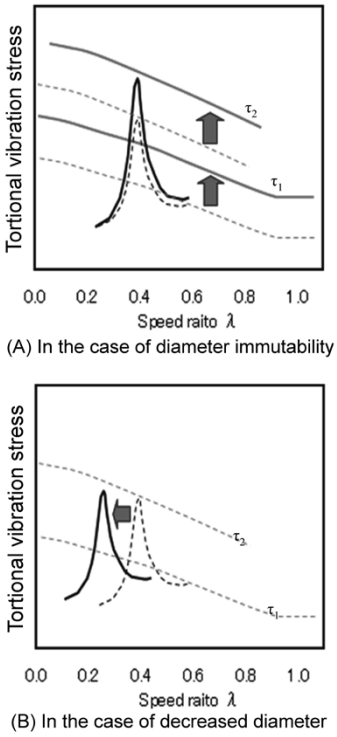


Fig.13 Effect of applying high-strength intermediate shaft

## 3. Rudder components

A rudder is a device for controlling the course of a vessel. Various types and structures of rudders have been devised for the abilities of slewing and thrusting. **Fig.14** shows a mariner rudder as a typical example. Here, the rudder stock and pintle, which constitute the slewing shaft (rudder shaft), are made of steel forgings, whereas the bearing portions of a rudder and rudder horn are made of steel castings. In some cases, the rudder horn is made of solid type steel castings.

Reducing the rudder thickness ($t$) decreases velocity resistance of a vessel and thus is considered to improve the fuel mileage. In order to reduce the rudder thickness ($t$), it is considered to be effective, from the Fig.14 bottom (cross-sectional view), to reduce the diameters of the pintle and rudder horn, that is, to increase the strength of the steel castings and forgings for rudders. It should be noted that the classification rules require rudder stocks and pintles to have weldability and stipulate that their carbon content be 0.23% or less.[14)] A low-alloy steel (steel name: KSFA65W-S), as shown in **Table 1**, has been developed as a high-strength material that satisfies the above requirement and has the high yielding point required for designing; the alloy obtained special approval from major classification societies. This steel has been used for many rudder stocks and pintles actually used on-board.

As for steel castings, the classification rules

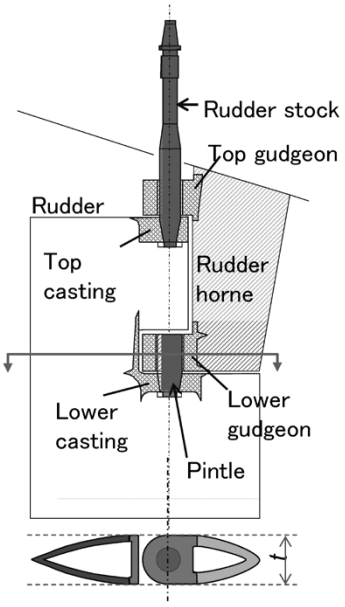


Fig.14 Schematics of cross section of mariner rudder

Table 1 Mechanical properties of low alloy steel KSFA65W-S for rudder-stock and pintle

| Tensile strength (MPa) | Yield strength (MPa) | Elongation (%) | | Reduction of area (%) | |
|---|---|---|---|---|---|
| | | Longitudinal | Tangential | Longitudinal | Tangential |
| 640–790 | 445 min. | 17 min. | 12 min. | 50 min. | 35 min. |

Table 2 Mechanical properties of low alloy cast steel for rudder parts

| Grade | Tensile strength (MPa) | Yield Strength (MPa) | Elongation (%) | Absorption energy at 0℃ (J) |
|---|---|---|---|---|
| SCAH450W | 450 min. | 255 min. | 20 min. | 27 |
| SCAH480W | 480 min. | 275 min. | 20 min. | 27 |
| SCAH550W | 550 min. | 355 min. | 18 min. | 27 |
| SCAH620W | 620 min. | 430 min. | 17 min. | 27 |

restrict their composition range.[14] Four grades of materials, as shown in **Table 2**, which are based on SCW620 steel casting for welded structure according to JIS, have obtained material approvals. The steel castings have a structure in which the castings are welded with thick steel plates. Optimization is being carried out to eliminate preheating of welding in order to facilitate plate working and with consideration to workability in attaching solid type rudder horns to the sterns of vessels. This project is almost completed.

## Conclusions

This paper introduces the development status of Kobe Steel's technologies for steel castings and forgings for vessels.

We will continue to develop technological seeds that contribute to increasing the value of vessels (improvements in fuel consumption, quality and reliability) on the basis of the material technology, component-forming technology and inspection technology introduced in this paper, and strive to contribute to the development of shipping and shipbuilding industries by responding to customers' needs.

## References

1) S. Ishida. *Journal of the Japan Institution of Marine Engineering*. 2011, Vol. 46, No. 6, pp. 46-48.
2) M. Kondo et al. *Journal of the Japan Institution of Marine Engineering*. 2011, Vol. 46, No. 2, pp. 5 -9.
3) *Calculation of Crankshaft for I.C. Engines*. Unified Requirement M53s of International Associations of Classification Societies Ltd.
4) Y. Murakami, *Metal fatigue: Effects of Small Defects and Nonmetallic Inclusions*. Yokendo, 1993, p. 265.
5) Fujitsuna et al. *17th International Forgemasters Meeting*. 2008, p. 390.
6) T. Shinozaki et al. *R&D Kobe Steel Engineering Reports*. 2009, Vol. 59, No. 1, pp. 94-97.
7) R. Yakura et al. *27th CIMAC Congress*. 2013, Paper No. 442.
8) Y. Yoshida et al. *R&D Kobe Steel Engineering Reports*. 2005, Vol. 55, No. 3, p. 7.
9) Y. Yoshida et al. *R&D Kobe Steel Engineering Reports*. 2005, Vol. 55, No. 3, p. 13.
10) A. Okamoto et al. *R&D Kobe Steel Engineering Reports*. 2005, Vol. 55, No. 3, p. 16.
11) Hamano et al. *19th International Forgemasters Meeting*. 2014, p. 520.
12) *Dimensions of propulsion shafts and their permissible torsional vibration stresses*. Unified Requirements M68 of International Associations of Classification Societies Ltd.
13) T. Ikegami et al. *10th International Symposium on Marine Engineering (ISME2014)*.
14) Class NK (Nippon Kaiji Kyokai). *Rules for the Survey and Construction of Steel Ships Part K MATERIALS*.

# Effect of Inclusion Size on Fatigue Properties in Very High Cycle Region of Low Alloy Steel Used for Solid type Crankshaft

Ryota YAKURA*1, Mariko MATSUDA*1, Dr. Tatsuo SAKAI*2, Dr. Akira UENO*2

*1 Technical Development Dept., Steel Casting & Forging Div., Iron & Steel Business
*2 Dept. of Mechanical Engineering, College of Science and Engineering, RITSUMEIKAN Univ.

*A study was conducted to grasp the fatigue properties, including the properties in a very highcycle fatigue region, of a low-alloy steel used for the solid type crankshaft of a 4-cycle diesel engine. Fatigue tests were conducted on specimens, some of which were taken from a solid type crankshaft and others taken from a round forged bar. The relation between the inclusion size at crack initiation sites and the fatigue property was studied on the basis of fracture mechanics. The study developed a relation equation between the fatigue life and inclusion size, as well as a relation equation between the threshold stress intensity range and inclusion size, for fracture initiated from the surface and internal inclusions. These equations show that decreasing inclusion size improves not only the fatigue strength working against surface fracture but also that attributable to internal fracture.*

## Introduction

Higher output and smaller size are desired for 4 cycle diesel engines for marine and onshore power generators.[1)-4)] This requires greater strength in solid type crankshafts for 4-cycle diesel engines. Therefore, low alloy steel having a tensile strength of 900-1,100MPa is being mainly used as the material.

Kobe Steel is focusing on the development of technologies for increasing fatigue strength, in addition to the strength of the material. Large steel forgings such as solid type crankshafts inevitably contain inclusions. These inclusions are known to become the initiation sites of fatigue cracks and decrease the fatigue strength in accordance with their sizes.[5)] The company has therefore decreased the amount and size of the inclusions contained in steel forgings and thus developed super clean steels with improved fatigue strength.[6)-8)] These steels are being applied to solid type crankshafts.

A solid type crankshaft is subjected to as many as $10^9$ cycles of stress during the entire service life of a 4-cycle diesel engine. The fatigue up to $10^9$ cycles of stress is called very high cycle fatigue, which is the focus of many studies.[9)] Although the materials of solid type crankshafts require understanding of their fatigue characteristics up to a very high cycle region, there are only a few examples of such studies.[10), 11)] Against this backdrop, fatigue tests were performed on low alloy steels for solid type crankshafts to confirm the presence of fatigue fractures in the very high cycle region and the effect of inclusion size on fatigue limits. A study was conducted on the relationship of fatigue life and fatigue limit to inclusion size.

## 1. Features of fatigue fractures in very high cycle region

Conventional thought has been that the fatigue fracture of steel does not occur unless the stress exceeds the fatigue limit appearing at $10^7$ stress cycles (hereinafter simply referred to as "fatigue limit") More recent studies, however, have clarified the existence of phenomena in which fatigue fractures occur at $10^7$ to $10^9$ cycles under stress lower than the fatigue limit, particularly in the case of high strength steel; this phenomenon is referred to as very high cycle fatigue.

The usual fatigue fractures are initiated from metal surfaces or from inclusions existing in surface layers (hereinafter referred to as "surface inclusions"); meanwhile, in the case of very high cycle fatigue fractures, the initiation sites of cracks are generally believed to be inclusions below surface layers (hereinafter referred to as "internal inclusions.")[9)] Such very high cycle fatigue fractures, initiated from internal inclusions, are considered to occur more often in bearing steel,[12)] spring steel[13)] and tool steel,[14)] for example, or in high strength steel having a tensile strength of 1,200MPa or greater.[15)] It is not clear, however, if very high cycle fatigue fractures occur in the low alloy steels for solid type crankshafts, which exhibit a tensile strength of approximately 900-1,100MPa.

## 2. Research and test method

### 2.1 Test materials

Test materials were made from steel ingots weighing 12 to 65 tonnes. The test steels included 40CrMo8, developed by Kobe Steel, as well as 34CrNiMo6, 36CrNiMo4 and 42CrMo4 (DIN standard steel). **Table 1** shows the target compositions of these steels and the amount ranges

Table 1 Target chemical composition of test steels

(mass%)

| Material | C | Si | Mn | Ni | Cr | Mo | S | O |
|---|---|---|---|---|---|---|---|---|
| 40CrMo8 | 0.38 | 0.25 | 0.90 | - | 2.00 | 0.25 | <60 ppm | <50 ppm |
| 34CrNiMo6 | 0.34 | 0.25 | 0.65 | 1.50 | 1.50 | 0.25 | | |
| 36CrNiMo4 | 0.36 | 0.25 | 0.65 | 1.00 | 1.00 | 0.25 | | |
| 42CrMo4 | 0.42 | 0.25 | 0.75 | - | 1.10 | 0.23 | | |

of S and O. In the case of 40CrMo8, adjustment was made on the amounts of S and O, as well as on slag compositions, etc., to control the size of inclusions, and both super clean steel (S<20 ppm, O<15 ppm) and conventional grade steel were prepared.

These steel ingots were hot-forged at a forging ratio of 3.0 or greater to form round bars with diameters of $\phi$450-620mm. In addition, two steel ingots of 40CrMo8, one consisting of super clean steel and the other consisting of conventional grade steel, each weighing approximately 65 tonnes, were hot-forged into solid type crankshafts with a principal axis diameter of 480mm.

The formed materials were subjected to quenching and tempering. The round bars were tempered to the tensile strength range of 800 to 1,100MPa, while the crankshafts were tempered to a tensile strength class of 1,000MPa (in the range of 950 to 1,050MPa).

Test specimens were prepared as shown in **Fig. 1**. In the case of the crankshafts, specimens were collected from their pin fillet, where the greatest load would be applied during operation; and, in the case of the round bars, each specimen was taken such that it was equivalent with the specimens from crankshaft pin fillets in terms of the depth from the surface and the direction of grain flow against the longitudinal direction of the specimen.

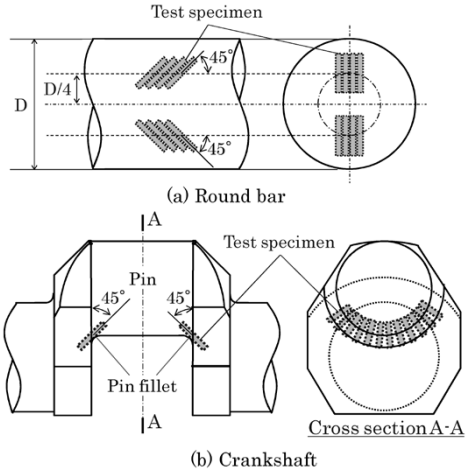


Fig. 1 Preparation of specimens

## 2.2 Fatigue test

### 2.2.1 High cycle fatigue test

Rotating bending fatigue tests were performed on the super clean steel and conventional grade steel to compare their fatigue limits up to $10^7$ cycles. In addition, the specimens collected from the crankshafts were subjected to axial load fatigue tests.

The rotating bending fatigue tests were conducted at a frequency of 60Hz on smooth specimens, each taken from the round bar and having a parallel portion of $\phi$10 x 30mm. A difference method was applied for the tests to determine the fatigue limit $\sigma_w$ for each specimen. More specifically, each fatigue test was conducted at stress amplitude $\sigma_a$, and if no failure occurred at 3 x $10^6$ cycles, the $\sigma_a$ was increased by increments of 20MPa, continuing the test until failure occurred. The failure stress ($\sigma_a$) minus 20MPa was determined to be $\sigma_w$. This method enables a directly study of the relationship between $\sigma_w$ and the inclusion size.

An axial load fatigue test was performed using a smooth specimen having a parallel portion of $\phi 10 \times 30$mm, at a stress ratio of -1. The tests were conducted at frequencies of 30 to 45Hz and were aborted at $10^7$ cycles.

### 2.2.2 Very high cycle fatigue test

In order to compare the fatigue characteristics up to the very high cycle region of super clean steel and conventional grade steel, cantilever rotating bending fatigue tests[16] were performed. Each specimen was taken from the crankshaft material, as in the case of the axial load fatigue test specimens, and had a sandglass shape with a minimum cross-sectional diameter of $\phi$4mm. The tests were conducted at a frequency of 52.5Hz and were aborted at $10^9$ cycles. It should be noted that all the above fatigue tests were performed in air at ambient temperature.

## 2.3 Observation of fracture surface and measurement of inclusion size

The fracture surfaces of failed specimens were observed by SEM. When the initiation site of a fatigue crack was an inclusion, the shape of the inclusion was approximated by a circumscribing ellipse, and the square root of the ellipse area, $\sqrt{area}$, was regarded as the value representing the inclusion size. The value of $\sqrt{area}$ is known to be an effective parameter for evaluating the effect of inclusion size on fatigue strength.[5]

## 3. Test results

### 3.1 Results of high cycle fatigue tests

**Fig. 2** shows the fatigue limits ($\sigma_w$) obtained by the rotating bending fatigue test, for the 40CrMo8 super clean steel compared with the conventional grade steel, including 40CrMo8 and other three grades, all in the 800-1,100MPa strength range. Although dispersion was observed in the data of both the super clean steel and conventional grade steel, increasing the tensile strength tended to increase fatigue limits. It was found that, although the upper limits of the dispersion were similar for the super clean steel and conventional grade steel, the lower limit was higher for the super clean steel. In other words, the $\sigma_w$ of the super clean steel is said to be consistently higher than that of the conventional grade steel.

**Fig. 3** shows the results of axial load fatigue tests on the super clean steel and conventional grade steel of 40CrMo8. The axial load fatigue tests were performed, focusing on the stress amplitudes that are considered, from the results of the rotating bending fatigue tests, to be in the vicinity of the fatigue limits. The axial load fatigue tests have confirmed two fracture modes; in one, the fatigue cracks are initiated from surface inclusions and, in the other, they are initiated from internal inclusions. The fatigue fractures initiated from surface inclusions mainly occurred at under $10^6$ cycles, whereas all the fatigue fractures initiated from internal inclusions occurred at $10^6$ cycles or higher. Referring to the minimum stress amplitudes at which failures occurred, the amplitudes were 545MPa and 380MPa for the super clean steel and conventional grade steel, respectively, in the case of fractures initiated from surface inclusion, and were 545MPa and 380MPa for the super clean steel and conventional grade steel, respectively, in the case of fractures initiated from internal inclusions. In either case, the super clean steel exhibited a higher stress amplitude.

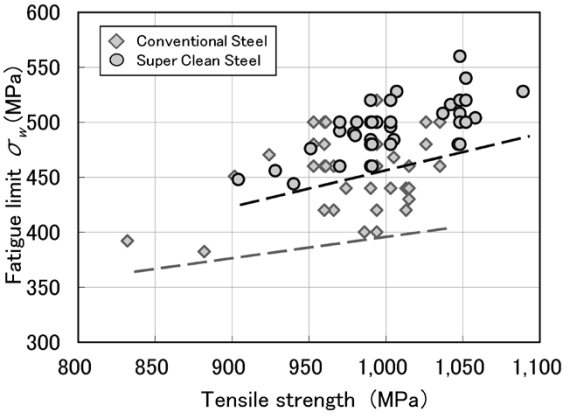

Fig. 2 Results of rotating bending fatigue tests

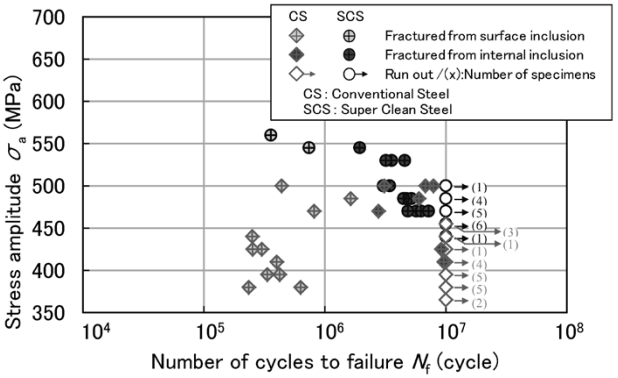

Fig. 3 Results of axial load fatigue tests on 40CrMo8

### 3.2 Results of very high cycle fatigue tests

The super clean steel and conventional grade steel of 40CrMo8 were subjected to cantilever rotating bending fatigue tests and the results are shown in **Fig. 4**. The super clean steel and conventional grade steel exhibited a $\sigma_w$ of 582.5MPa and 525MPa, respectively, the former being approximately 11% higher than the latter. All the fatigue cracks initiated from the metal surface in the case of the super clean steel, but from the surface inclusions in the case of the conventional grade steel. There was no fracture initiated from an internal inclusion, as seen in the axial load fatigue test, and the same can be said of fatigue fractures in the $10^{6\text{-}9}$ cycle range.

### 3.3 Results of fracture surface observation

**Fig. 5** shows the examples of fracture surfaces in backscattered electron images captured by SEM. As described above, three types of fatigue-crack initiation sites were observed: namely, metal surfaces (Fig. 5 (a)), surface inclusions (Fig. 5 (b)) and

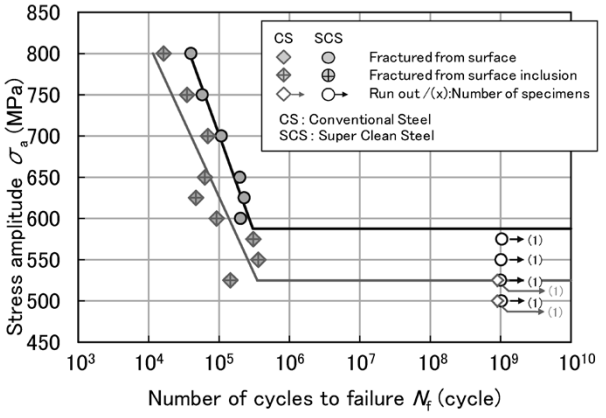

Fig. 4 Results of cantilever rotating bending fatigue test on 40CrMo8

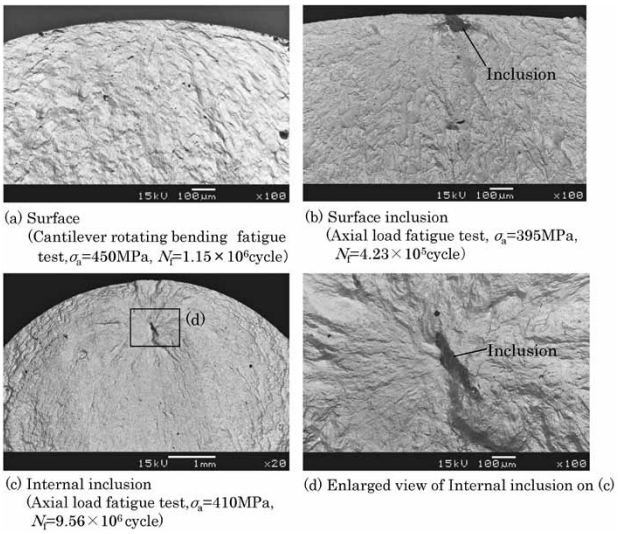


(a) Surface (Cantilever rotating bending fatigue test, $\sigma_a$=450MPa, $N_f$=1.15×10$^6$cycle)
(b) Surface inclusion (Axial load fatigue test, $\sigma_a$=395MPa, $N_f$=4.23×10$^5$cycle)
(c) Internal inclusion (Axial load fatigue test, $\sigma_a$=410MPa, $N_f$=9.56×10$^6$ cycle)
(d) Enlarged view of Internal inclusion on (c)

Fig. 5 Examples of fatigue crack initiation sites

internal inclusions (Fig. 5 (d), which is an enlarged view of (c) with focus on the inclusion in (c)). The sizes of the inclusions ($\sqrt{area}$) were approximately 20 to 60 $\mu$m for the super clean steel and 20 to 150 $\mu$m for the conventional grade steel.

## 4. Discussions

### 4.1 S-N relationship corresponding to fracture modes

**Fig. 6** shows the collective results of the cantilever rotating bending fatigue tests and axial load fatigue tests. In Fig. 6, the super clean steel and conventional grade steel are not distinguished, and different data points are used depending on the test methods and fracture modes. It appears from Fig. 6 that an S-N relationship holds for each of the fatigue crack initiation sites, namely, metal surfaces (Surface), surface inclusions (Surface inclusion) and internal inclusions (Internal inclusion). The fatigue life was shortest for fatigue cracks initiated from surface inclusions, shorter for those initiated from metal surfaces, and longest for those initiated from internal inclusions. The fractures initiated from surface inclusions exhibited a lower minimum failure stress than did the fractures initiated from internal inclusions. The possibility cannot be denied, however, that fracture initiated from an internal inclusion may occur in the cycle range beyond $10^7$ at a stress amplitude lower than the minimum failure stress determined for the fractures initiated from surface inclusions, since the axial load fatigue tests were aborted at $10^7$ cycles. In the case of the cantilever rotating bending fatigue tests, no fatigue fracture was due to an internal inclusion in the long-life range ($10^{6\text{-}9}$ cycles); however, the specimen size,

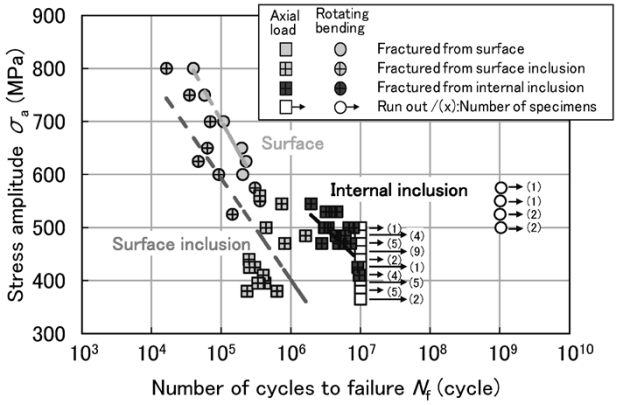


Fig. 6 Results of axial load and cantilever rotating bending fatigue tests on 40CrMo8

which is smaller than the one for the axial load fatigue tests, may have resulted in a smaller number of internal inclusions, which may have led to the non-appearance of any fracture initiated from an internal inclusion. In other words, it was not yet clear, at this point, whether any fracture initiated from an internal inclusion occurs in the range beyond $10^7$ cycles and what the S-N relationship would be. Against this backdrop, the following study was conducted to predict the behavior of fractures initiated from internal inclusions in the range beyond $10^7$ cycles.

### 4.2 Relationship between fatigue life and inclusion size

The initial stress intensity factor range, $\Delta K$, assuming the inclusion to be a crack, is expressed by Equation (1) based on $\sqrt{area}$ and stress amplitude, $\sigma_a$:[5]

$$\Delta K = M\sigma_a(\pi\sqrt{area})^{1/2} \quad \cdots\cdots (1),$$

wherein M is the correction coefficient for the stress intensity factor and is known to be 0.65 for fatigue cracks initiated from surface inclusions and 0.50 for those initiated from internal inclusions.[5] Also, it is believed that a double logarithmic linear relationship, as expressed by Equation (2), holds between the $\Delta K$ determined by Equation (1) and a parameter, $N_f/\sqrt{area}$, determined by dividing fatigue life $N_f$ by $\sqrt{area}$:[10]

$$\Delta K = \alpha\,(N_f/\sqrt{area})^{\beta} \quad \cdots\cdots (2).$$

On the basis of the results of the axial-load and cantilever rotating bending fatigue tests on 1,000MPa class 40CrMo8, as well as the results of the fracture surface observation by SEM, the relationships between $\Delta K$ and $(N_f/\sqrt{area})$ were plotted; the results are shown in **Fig. 7**. It was estimated from Fig. 7 that the $\alpha$ in Equation (2) is 25 for fractures initiated from surface inclusions and 44 for fractures initiated from internal inclusions, while $\beta$ is -0.21

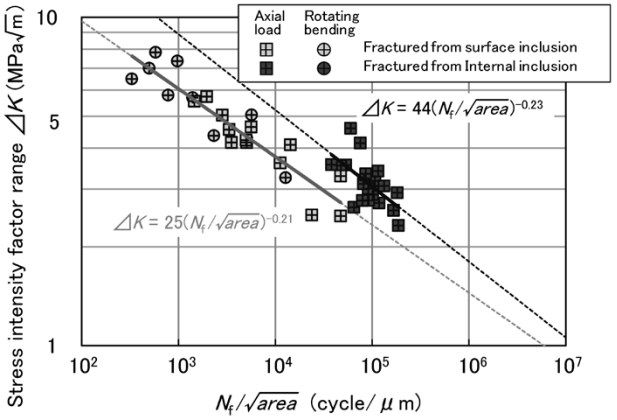


Fig. 7 Relationship between $\Delta$K and ($N_f/\sqrt{area}$) for 40CrMo8

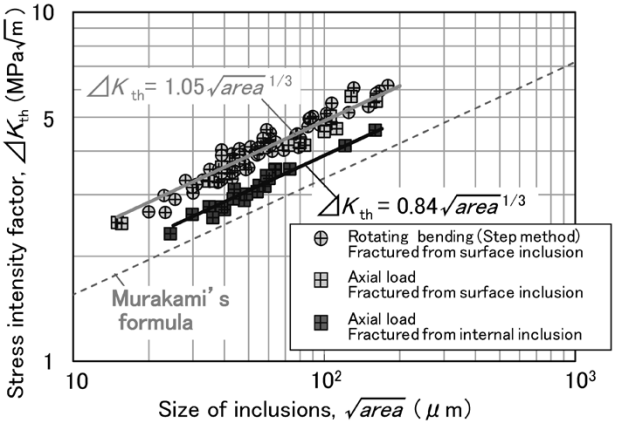


Fig. 8 Relationship between $\Delta K_{th}$ and $\sqrt{area}$ for 40CrMo8

for fractures initiated from surface inclusions and -0.23 for fractures initiated from internal inclusions. On the basis of Equation (2), as well as $\alpha$ and $\beta$ determined from Fig. 7, $N_f$ for surface and internally-initiated fractures can be estimated for any given $\sigma_a$ and $\sqrt{area}$.

### 4.3 Relationship between fatigue limit and inclusion size

In general, the fatigue limit of steel is believed to correspond, not to the generation limit of cracks, but rather, to the arrest limit of crack propagation.[5] Therefore, clarifying the relationship between the lower limit of the stress intensity factor range, $\Delta K_{th}$, the threshold for cracks to start propagation, and $\sqrt{area}$ clarifies the effect of inclusion size on fatigue limit.

**Fig. 8** shows the results of the rotating bending fatigue test and axial load fatigue test on 1,000MPa class 40CrMo8, as well as the plots of $\Delta$K, calculated by Equation (1) on the basis of the SEM fracture surface observation, against the experimental values of $\sqrt{area}$.

The rotating bending fatigue tests, based on a difference method, provide $\sigma_w$ and for each specimen. These values are assigned to $\sigma_a$ and $\sqrt{area}$ of Equation (1), which provide $\Delta$K that can be regarded as the threshold, $\Delta K_{th}$, at which fatigue cracks start to propagate.

Meanwhile, $\Delta$K calculated by assigning the failure stress, $\sigma_f$, obtained by the axial load fatigue tests, and $\sqrt{area}$ value into $\sigma_a$ and $\sqrt{area}$ of Equation (1) cannot be regarded as $\Delta K_{th}$ per se. In this study, however, the above described $\Delta$K is treated as $\Delta K_{th}$ to formulate the relationship between $\Delta K_{th}$ and $\sqrt{area}$ for fractures initiated from internal inclusions, due to the facts that the axial load fatigue tests were performed under the stress amplitudes considered to be in the vicinity of the fatigue limit, and that the data points for the fractures initiated from surface inclusions of the difference method and axial load fatigue test were in agreement.

Because a tendency similar to Murakami's equation,[5] expressed by Equation (3), was recognized for both the fractures initiated from the surface and those initiated from internal inclusions in Fig. 8, $\Delta K_{th}$ was assumed to be proportional to $(\sqrt{area})^{1/3}$ to provide Equation (4).

$$\Delta K_{th} = 3.3 \times 10^{-2} (HV+120 (\sqrt{area}))^{1/3} \quad \cdots\cdots (3)$$

$$\Delta K_{th} = \gamma (\sqrt{area})^{1/3} \quad \cdots\cdots (4)$$

From Fig. 8, the coefficient $\gamma$ for fractures initiated from surface inclusions was estimated to be 1.05, while the one for fractures initiated from internal inclusions was estimated to be 0.84 in the case of 1,000MPa class 40CrMo8. Furthermore, from Equation (4), $\Delta K_{th}$ for fractures initiated from internal inclusions can be estimated for any given $\sqrt{area}$, and it is thus possible to calculate $\sigma_w$, as will be described in the next section.

### 4.4 Estimation of S-N curve and estimation on the effect of inclusion size

On the basis of Equations (1) and (2), which relate $\Delta$K to $N_f$ and $\sqrt{area}$, along with Equation (4), expressing the relationship between $\Delta K_{th}$ and $\sqrt{area}$, S-N curves can be calculated for fractures initiated from both surface and internal inclusions having any given size.

Firstly, the inclusion size is assumed to be $\sqrt{area}$, and a stress amplitude $\sigma_{a,i}$ is assigned to Equation (1) to calculate the stress intensity factor range, $\Delta K_i$, corresponding to $\sigma_{a,i}$. Assigning the calculated $\Delta K_i$ and $\sqrt{area}$ to Equation (2) determines the number of cycles to failure, $N_{f,i}$ corresponding to $\sqrt{area}$ and $\sigma_{a,i}$. Determining $N_{f,i}$ for other $\sigma_{a,i}$ values in a similar manner enables the calculation of an S-N curve within a finite life region, as shown by the curve ① in **Fig. 9**. Next, using Equation (1) to determine the

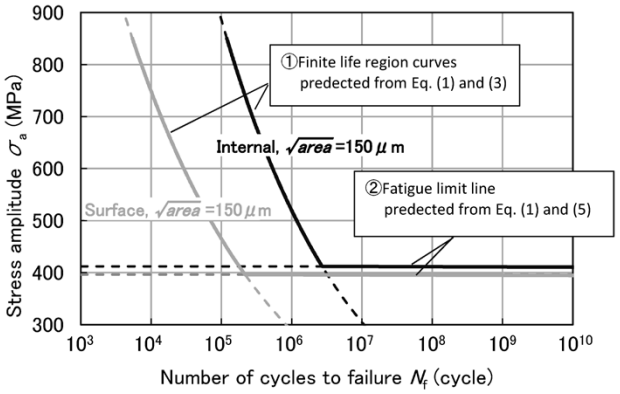


Fig. 9 Method of calculating S-N curves

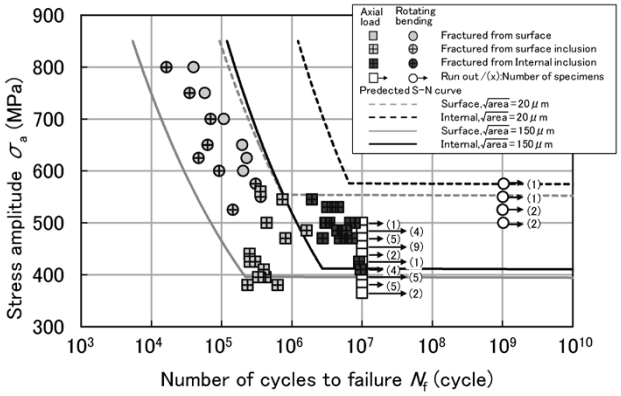


Fig.10 S-N curves calculated for 40CrMo8

stress amplitude corresponding to the threshold stress intensity range $\Delta K_{th}$, which is given by assigning $\sqrt{area}$ to Equation (4), $\sigma_w$ and the straight line ② are obtained. As shown in Fig. 9, eliminating the portion of the curve ① below the intersection between curve ① and straight line ②, along with the left side portion of the straight line ②, provides an S-N curve.

**Fig.10** shows estimated S-N curves. Since the sizes of inclusions observed on the fracture surface of the fatigue specimens fell in the range of $\sqrt{area}$ = 20-150 $\mu$m, the S-N curves for fractures initiated from the surface and internal inclusions were calculated under the two conditions of the lower limit, 20 $\mu$m, and the upper limit, 150 $\mu$m.

The results show that almost all data points for the fractures initiated from the surface and internal inclusions fall between the S-N curves calculated for $\sqrt{area}$ = 20 $\mu$m and $\sqrt{area}$ = 150 $\mu$m of respective fracture mode. Furthermore, the maximum value of $\sigma_a$ (=575MPa), at which no failure occurred at $10^9$ cycles of the cantilever rotating bending fatigue test, roughly matched $\sigma_w$ (the horizontal portion) of the S-N curve calculated for the fracture initiated from an internal inclusion of $\sqrt{area}$ = 20 $\mu$m. From the above results, the S-N curves calculated by the present technique are believed to be reasonable.

On the basis of the calculated S-N curves in Fig.10, the following can be said for the fatigue characteristics, including the very high cycle region, of 1,000MPa class 40CrMo8. First, the comparison of the S-N curves calculated for $\sqrt{area}$ = 20 $\mu$m and 150 $\mu$m shows that the position of the S-N curves for $\sqrt{area}$ = 20 $\mu$m is position on the long-life side of the figure with a higher $\sigma_w$, than the one for $\sqrt{area}$ = 150 $\mu$m in the case of fractures initiated from a surface as well as those initiated from internal inclusion. This result indicates that super clean steel, having reduced inclusion size, can have improved fatigue limits, not only for the fractures initiated from surface inclusions, but also for the fractures initiated from internal inclusions. In addition, the comparison between the S-N curves calculated for the fracture initiated from an internal inclusion and fracture initiated from a surface inclusion, both the inclusions having the same $\sqrt{area}$, shows that a fracture initiated from an internal inclusion indicates a $\sigma_w$ higher than that of a fracture initiated from a surface inclusion. In other words, in the case where inclusions of the same size exist in the surface layer and interior, no fatigue fracture occurs from the internal inclusion under a stress equal to or below $\sigma_w$ for the fracture initiated from a surface inclusion. Furthermore, each S-N curve has a sloped portion and horizontal portion intersecting at a position lower than $10^7$ cycles. This implies that, in the high cycle region at or beyond $10^7$ cycles, neither fracture initiated from the surface nor fracture initiated from internal inclusion will occur.

## Conclusions

Fatigue characteristics including the very high cycle region were studied for super clean steel and the conventional grade steel used for solid type crankshafts. The effect of inclusion size on the fatigue life and fatigue limit was also studied. The following describes the results obtained:

1) Cantilever rotating bending fatigue tests, up to the maximum of $10^9$ cycles, showed no fatigue fracture at or beyond $10^7$ cycles for both the super clean steel and conventional grade steel.
2) A relational expression was obtained for the relationship between the fatigue life, $N_f$, and inclusion size, $\sqrt{area}$, for fractures initiated from surfaces and internal inclusions of a low alloy steel manufactured by Kobe Steel for solid type crankshafts. A relational expression was also obtained for the threshold stress intensity range, $\Delta K_{th}$, and inclusion size, $\sqrt{area}$.
3) The relational expressions in 2) enable the calculations of S-N curves for both the fractures initiated from the surface and from an internal

inclusion for the inclusion size range of $\sqrt{area}$ = 20-150 $\mu$m.

4) It is considered that reducing the inclusion size can improve not only the fatigue limit due to fractures initiated from surface inclusions, but also the fatigue limit due to fractures initiated from internal inclusions.

## References


1) M. Makabe. *Proceedings of 75th Conference on Marine Engineering*. 2006, p.77.
2) F. Koch. *The new MAN B&W L21/31 Engine-Design Development and Experience*. 2004, No.174.
3) J. Kytola. *Development of the Waertsilae 4-stroke enginerange*. 2004, No.123.
4) Y. Miyawaki et al. *The new DAIHATSU DC-17 4-stroke medium speed diesel engine*. 2004, No.101.
5) Y. Murakami. *Metal Fatigue: Effects of Small Defects and Nonmetallic Inclusions*. 1993.
6) T. Shinozaki et al. *R&D Kobe Steel Engineering Reports*. 2009, Vol.59, No.1, pp.94-97.
7) T. Shinozaki, et al. *International Symposium on Marine Engineering*. 2009.
8) R. Yakura, et al. *CIMAC Congress (2013)*. Paper No.442.
9) Tatsuo Sakai. *Journal of Solid Mechanics and Materials Engineering*. 2009, Vol.3, No. 3, pp.425-439.
10) S. Omata et al. *Journal of the Japan Institute of Marine Engineering*. 2003, Vol. 38, No.7, pp.55-62.
11) R. Yakura et al. *Proceedings of the 63rd JSMS Annual Meetings*. 2014, Presentation Number 206.
12) T. Sakai et al. *Journal of Society of Material Science Japan*. 2000, Vol.49, No.7, pp.779-785.
13) T. Abe et al. *Transactions of the Japan Society of Mechanical Engineers (A)*. 2001, Vol.67, No.664, pp.112-119.
14) K. Shiozawa et al. *Proceedings of the annual meeting of JSME/MMD*. 2001, pp.243-244.
15) K. Kanazawa et al. *NRIM Fatigue Data Sheet Technical Document*. 1989, No.9.
16) T. Yamamoto et al. *Proceedings of VHCF-5*. 2011, pp.439-444.

# Kobe Steel's Original Titanium Alloys Developed in the Past 20 Years

Dr. Hideto OYAMA
Titanium Division, Iron & Steel Business

*In the past 20 years, Kobe Steel has developed and commercialized various titanium alloys. AKOT is a corrosion-resistant alloy, in which Cr has the important role of enriching Pd and Ru on the corroded surface. Ti-1.2ASN is a heat-resistant alloy that can be used at temperatures up to 800℃, in which oxidation resistance has been improved by the addition of Al and Si, and grain growth is inhibited by silicide. Ti-9 is a quasi Ti-6Al-4V alloy that is as coilable as CP-titanium. Its Al content has been suppressed to 4.5% to enhance cold rollability, and Si has been added to ensure the ductility of welds. KS EL-F is a quasi Ti-6Al-4V and is as hot-forgeable as CP-titanium, in which C is exploited to achieve high strength at temperatures up to approximately 500℃ and to reduce flow stress during hot-forging.*

## Introduction

Titanium has come to be widely known as a lightweight, non-corroding metal; however, there are cases where the metal corrodes in severely corrosive environments. Basically, metallic titanium is obtained by reducing titanium oxide and can easily be oxidized and become brittle when exposed to the atmosphere. Thus, some environments are difficult for simple commercially-pure (CP) titanium to withstand. Alloy Ti-6Al-4V is a typical titanium alloy commonly used for aircraft parts; however, it suffers from poor hot/cold workability, which often results in low productivity.

In the past 20 years, Kobe Steel has developed various original titanium materials for solving these problems, while as much as possible avoiding an increase in cost, in the hope that titanium would be used in a wider range of environments. This paper outlines these titanium materials.

## 1. Anti-crevice-corrosion alloy： AKOT

Crevice corrosion occurs easily in severe environments, such as a highly concentrated chloride environment at elevated temperatures. Alloys including Ti-0.15Pd have been developed to resist such crevice corrosion.[1] Since platinum group elements are very expensive, many researchers have focused on reducing the additive amount of platinum group elements as much as possible.[2)-4)] Under such circumstances, Kobe Steel developed Ti-0.4Ni-0.015Pd-0.025Ru-0.14Cr, named AKOT.[5)]

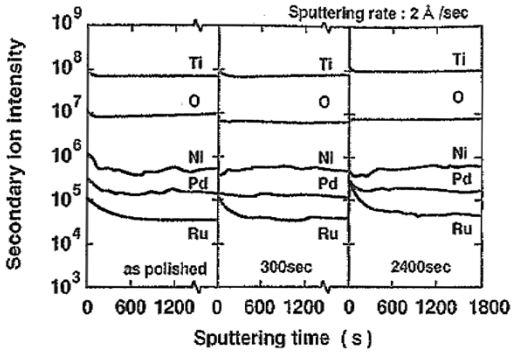


Fig. 1 SIMS depth profiles of Ti-0.41Ni-0.01Pd-0.02Ru alloy immersed in boiling 10 mass% hydrochloric acid solution

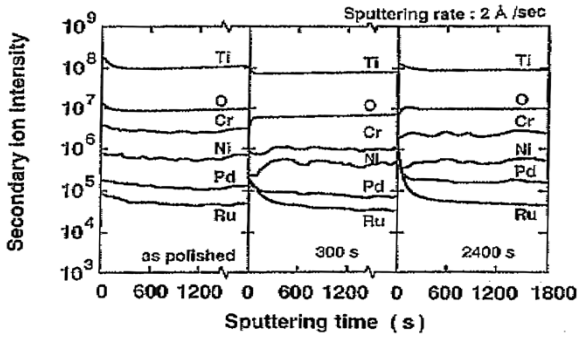


Fig. 2 SIMS depth profiles of additive elements in Ti-0.41Ni-0.01Pd-0.02Ru-0.14Cr alloy immersed in boiling 10 mass% hydrochloric acid solution

**Figs. 1** and **2** are the results of secondary ion-microprobe mass spectrometry (SIMS) performed on Ti-0.41Ni-0.01Pd-0.02Ru alloy and Ti-0.41Ni-0.01Pd-0.02Ru-0.14Cr alloy, respectively, showing the concentration depth profiles of the additive elements in the alloys, which were immersed in 10mass% boiling hydrochloric acid solution for 0s (as polished), 300s and 2,400s. In both alloys, the platinum group elements, Pd and Ru, are enriched near the surface, and this enrichment tends to become more pronounced with the addition of Cr. On the basis of this knowledge, the additive amounts of Ni, Pd and Ru were optimized to develop AKOT. AKOT has been used in severe atmospheres, such as that found in soda electrolysis.

## 2. Titanium alloys, Ti-1.5Al, Ti-1.2ASN and Ti-0.9SA, for mufflers

CP titanium has been used for motorcycle mufflers since the early 1990s. Kobe Steel was ahead

of the rest of the world in starting to develop high-temperature resistant alloys for mufflers in order to widen the applicability of titanium materials and commercialized Ti-1.5Al [6] in the year 2000. A motorcycle muffler cools down in the air more easily than does a muffler for four-wheel vehicles. Hence, the company continued developing muffler alloys that can withstand even higher temperatures. The major challenge in developing a temperature resistant muffler material is to prevent embrittlement due to oxidation and grain coarsening at elevated temperatures. Trying to solve this problem with a minimal addition of alloying elements presents another challenge, since a large amount of added elements deteriorates the formability indispensable to this application.

Against this backdrop, Kobe Steel continued a study on the minor addition of Al and Si on the basis of the fact that the oxidation of Ti-1.5Al is more suppressed than that of CP titanium and that Si forms silicide that suppresses grain growth, as described later. As a result, the company developed Ti-1.2ASN, a muffler alloy that can be used at temperatures up to 800℃.[7] The alloy was adopted in the Toyota Supercar, Lexus LFA, in 2010. Furthermore, attempts have been made to expand the application, not only to supercars, but also to a wide variety of vehicles. Expensive Nb, which was used in Ti-1.2ASN, was eliminated, and the amounts of additive elements were adjusted to improve the formability by lowering the annihilation temperature of silicide such that the formation of silicide can be controlled during annealing in a continuous annealing/pickling line. This effort resulted in the development of Ti-0.9SA.[8]

**Fig. 3** compares the thickness reduction and grain size of CP titanium, Ti-1.5Al, and Ti-1.2ASN after exposure to air at 800℃ for 200 hours. The CP titanium exhibits a significant thickness reduction due to the exfoliation of oxidation scale with more pronounced coarsening of crystal grains, whereas Ti-1.5Al exhibits suppression in both the formation of oxidation scale and crystal grain growth. Furthermore, Ti-1.2ASN exhibits almost no thickness reduction with the grain coarsening being effectively suppressed thanks to the presence of silicide. **Fig. 4** compares CP titanium with Ti-1.2ASN in the state of oxidation scale after the above described exposure to high-temperature air. The CP titanium exhibits thickly formed oxidation scale with a number of voids, whereas the oxidation scale formed on Ti-1.2ASN is dense and thin. The reason is considered to be as follows: as shown in **Fig. 5**, the electron-probe micro analyzer (EPMA) images taken from beneath the oxidation scales after the exposure to high-temperature air shows Al and Si, despite being minor additive elements, enriched on the metal surface, preventing Ti from diffusing to the surface.

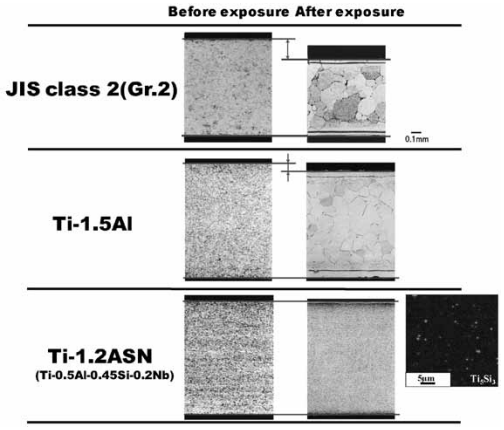


Fig. 3 Comparisons of wall thinning and grain growth behavior in JIS class 2, Ti-1.5Al and Ti-1.2ASN materials after exposure at 800℃ for 200 hours in air

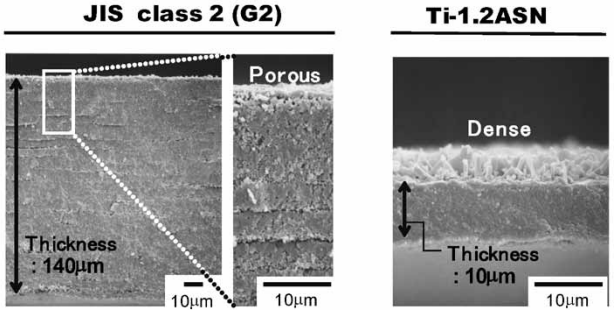


Fig. 4 Comparison of oxidation scale in JIS class 2 CP-Ti and Ti-1.2ASN after exposure at 800℃ for 200 hours in air

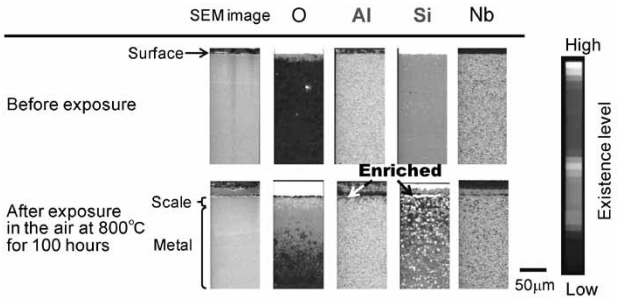


Fig. 5 EPMA mappings of Ti-1.2ASN after exposure at 800℃ for 200 hours in air

## 3. Alloys compensating for the weakness of Ti-6Al-4V alloy: Ti-9, KSEL-F and Ti-531C

As described in the introduction, titanium alloy is represented by Ti-6Al- 4V alloy, whose workability is rather poor under either hot or cold working. Due to this, when, for example, a thin sheet is manufactured, a rolling method called pack-rolling is adopted. In this method, a rolling stock with a

certain degree of thickness is completely surrounded by steel sheets so as to maintain the temperature during rolling. This rolling technique requires a complicated process that is one of the major factors increasing the cost. In order to overcome this problem, Kobe Steel has developed an alloy equivalent of Ti-6Al-4V, Ti-9, which can be coil-rolled as in the case of CP titanium.[9), 10)] In addition, poor hot-workability results in cracking during hot-forging, leading to an increase in the number of forging steps. To cope with this issue, Kobe Steel has developed another Ti- 6Al- 4V equivalent alloy, KS EL-F,[11)] which is just as forgeable as CP titanium, and also developed Ti-531C,[12)] whose composition has been adjusted to improve the machinability of KS EL-F.

**Fig. 6** shows the tensile properties of a coil of Ti-9. Although anisotropy in strength due to unidirectional rolling is observed, an elongation of 7-8% or greater has been obtained even in the T direction, which exhibits higher strength. Ti-9 has a composition of Ti-4.5Al-2Mo-1.6V-0.5Fe-0.3Si-0.03C, in which the amount of Al is kept at 4.5% to secure cold-rollability. Other elements have also been optimized in view of the strength and post-welding characteristics.

**Fig. 7** compares KS EL-F（Ti-4.5Al-4Cr-0.5Fe-0.2C) with Ti-6Al-4V alloy in tensile strength at ambient to elevated temperatures. KS EL-F has a reduced amount of Al, an element that increases high-temperature strength, with an increased amount of C to compensate for the decrement in strength. This alloy exploits the fact that C, an interstitial element, contributes to solid-solution strengthening in a relatively low temperature range, however, this solid-solution strengthening effect is decreased significantly at the elevated temperatures at which hot forging is performed. A large amount of C is added in the vicinity of the solid-solubility

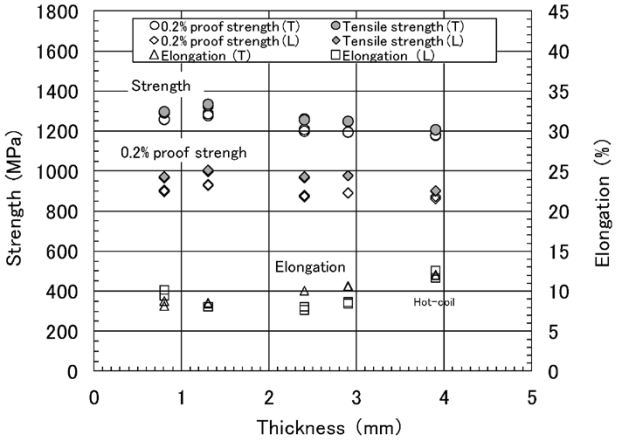


Fig. 6 Tensile properties of first strip of Ti-9

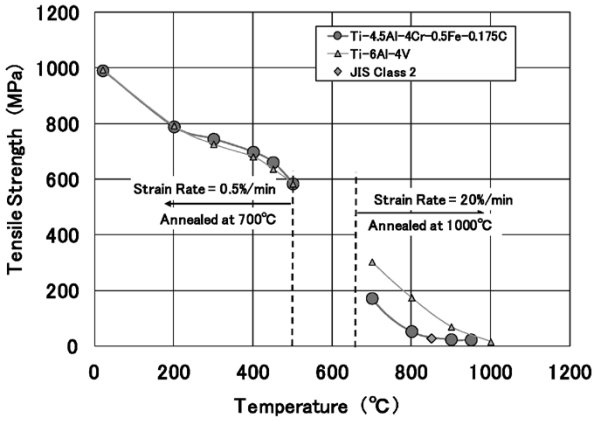


Fig. 7 Temperature dependence of tensile strength of KS EL-F

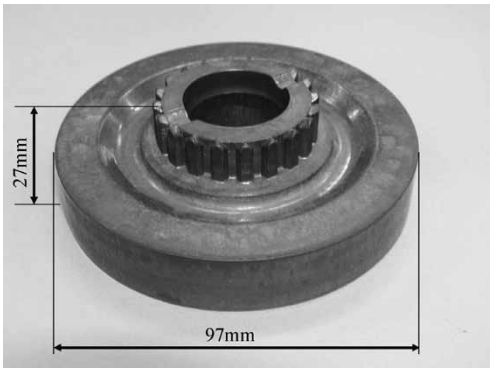


Fig. 8 Gear part forged from 45 mm diameter and 66 mm length billet of KS EL-F in mass production line for steel (SCM415) in single heat process

limit in the $\beta$ phase, while other additive elements are selected from low cost options whenever possible. As shown in Fig. 7, the strength is at a level similar to that of Ti-6Al-4V up to approximately 500℃; however, the strength decreases significantly at temperatures of 700℃ or higher, offering excellent hot workability. KS EL-F can be hot-forged into a part with a shape such as that shown in **Fig. 8** in a single heating cycle.

There may be TiC found in KS EL-F, due to production hysteresis. Although it has been confirmed that TiC does not inhibit mechanical properties, including fatigue strength, an increased amount of TiC has been demonstrated to decrease machinability as shown in **Fig. 9**. The effect of the amount of Cr and Fe on the solid solubility limit of C in $\beta$ phase was therefore calculated as shown in **Table 1**. Two compositions, F-1 and F-2, in which a part of Cr is replaced by Fe, were selected and compared with KS EL-F and Ti-6Al-4V in terms of machinability. As a result, F-1 and F-2 have been demonstrated to exhibit machinability superior to that of KS EL-F, as shown in **Fig.10**. On the basis of these results, the composition was finalized as Ti-4.5Al-2.5Cr-1.25Fe-0.1C (Ti-531C.)

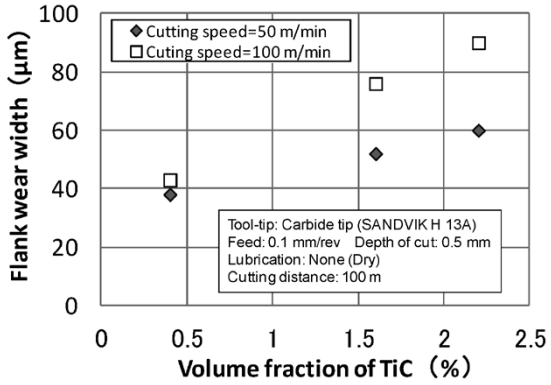


Fig. 9 Influence of TiC volume fraction on flank wear width of cutting tool tip

Table 1 Alloy compositions and their calculated solubility limits of C into β phase

(mass%)

| Alloy | Al | Cr | Fe | C | Solubility limit of C |
|---|---|---|---|---|---|
| KS EL-F | 4.5 | 4 | 0.5 | 0.15 | 0.14 |
| F-1 | 4.5 | 2.5 | 1.25 | 0.15 | Not calculated |
| F-2 | 4.5 | 1 | 2 | 0.15 | 0.198 |

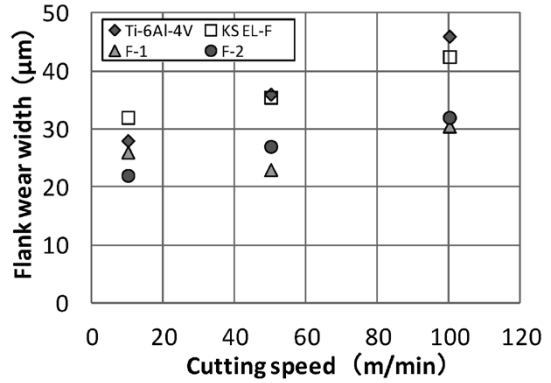


Fig.10 Comparison of flank wear width of cutting tool tip in F-1, F-2, KS EL-F and Ti-6Al-4V

## Conclusions

Some of the titanium materials that Kobe Steel originally developed in the last 20 years have been outlined in terms of technical points, including the concept of alloy development. These alloys were developed with the aims of expanding the applicability of titanium materials and satisfying customers. Kobe Steel will strive to develop titanium materials that adequately meet the needs of customers by further enhancing the technologies of the titanium materials developed thus far and by expanding the field of view, including the technologies of multi-material utilization.

## References


1) M. Stern et al. *J. Electrochem Society. 1959*, Vol. 106, No. 9, pp.759-764.
2) R. S. Class. *Elcromica Acta*. 1983, 28, pp.1507-1513.
3) K. Taki. *Titanium-Zirconium*. The Japan Titanium Society, 1988, 36, pp.29-33.
4) R. W. Schutz et al. *Proceeding of the 12th International Corrosion Congress*, NACE. Houston, TX, September 1993, 3 A, p. 1213.
5) T. Yashiki et al. *Titanium'95 Science and Technology*. The Institute of Metals. London, UK, 1996, 1871-1878.
6) N. Matsukura et al., *R&D Kobe Steel Engineering Reports*. 2004, Vol. 54, No. 3, pp.38-41.
7) T. Yashiki. *Ti-2007 Science and Technology, JIM. Japan,* 2007, pp. 1387-1390.
8) K. Tada et al. *R&D Kobe Steel Engineering Reports*. 2010, Vol.60, No.2, pp.42-45.
9) H. OYAMA et al. *R&D Kobe Steel Engineering Reports*. 1999, Vol.49, No.3, pp.53-56.
10) S. Kojima et al. *Ti-2003 Science and Technology*. WILEYVHC Verlag GmbH & Co. KGaA, Weinheim. 2004, pp.3097-3102.
11) S. Kojima et al. *Ti-2003 Science and Technology*. WILEYVHC Verlag GmbH & Co. KGaA, Weinheim. 2004, pp.3089-3095.
12) S. Murakami. *Titanium*. 2015, Vol.63, No.2, pp.104-107.

# High Heat-transfer Titanium Sheet-HEET®- for Heat Exchangers

Keitaro TAMURA*1, Yoshio ITSUMI*1, Dr. Akio OKAMOTO*1, Dr. Hideto OYAMA*2, Dr. Hirofumi ARIMA*3, Dr. Yasuyuki IKEGAMI*3

*1 Titanium Plant, Titanium Div., Iron & Steel Business
*2 Titanium Div., Iron & Steel Business
*3 Institute of Ocean Energy, Saga University

*A plate-type heat exchanger (PHE) that uses seawater as a cooling/heating medium is widely employed by chemical plants, power-generating facilities and large transport ships. Titanium is a common material for these heat exchangers, particularly for their primary members, including a heat exchanging plate and piping, thanks to its excellent corrosion resistance to seawater. Improving the heat-transfer performance of PHE enables the reduction in number and size of the plate used in PHE and thus enables the entire facility to be downsized. Kobe steel have developed a high heat-transfer titanium plate-HEET®-which has a heat-transfer performance that is significantly improved by fine irregularities imparted on its surface. The surface area increased by the fine irregularities, along with the promoted nucleate boiling, has improved the heat-transfer and particularly increased the evaporative heat transfer by approximately 20% or more.*

## Introduction

Titanium has excellent corrosion resistance against seawater. Therefore, it is frequently applied to the primary members, such as heat-exchanging plates and piping, of plate-type heat exchangers (PHEs) that use seawater for cooling and heating. Such PHEs are commonly found in chemical plants, power-generating facilities, and large transport ships, etc.[1] **Fig. 1** shows the structure and operating principle of a PHE. A PHE is an apparatus for exchanging heat between seawater and a medium to be heated or cooled by the seawater and comprises a plurality of plates, wherein seawater is made to flow in the opposite directions on both the side of each plate. As shown in **Fig. 2**, there are three types of heat transfer that are responsible for heat exchange: namely, liquid-single-phase forced-convection heat transfer, in which hot water discharged from a factory, for example, is cooled by cold seawater; evaporation heat transfer, in which working fluid is converted into gas by warm seawater as in the case of ocean thermal energy conversion; and condensation heat transfer, in which working gas is converted into liquid. Improving the performance of each type of heat transfer improves the efficiency of heat exchangers. Also, decreasing the number and size of plates used in a PHE enables downsizing of the entire facility.

Various research and development have so far been carried out to improve the efficiency of heat exchangers. As for the methods of improving the heat transfer from the plate material, particularly in the case of evaporation heat transfer, there has been reported a method of thermally spraying stainless steel particles on a plate surface to make it porous,[2] and a method utilizing the electrodeposition of copper to form a coating film with fine asperities on the surface.[3] It has been confirmed that, in these methods, the fine asperities on a surface act as boiling nuclei to promote nucleate boiling and thus improve evaporation heat transfer. All these methods, however, suffer from problems in long-term stability, e.g., the exfoliation of

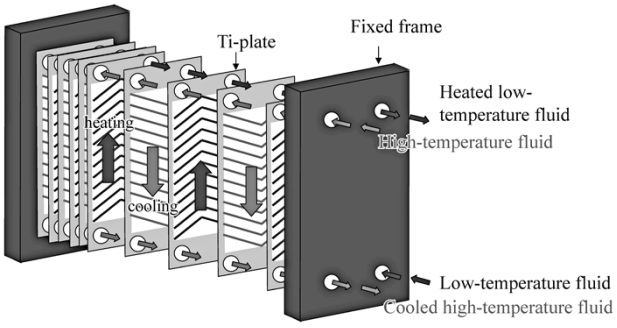


Fig. 1 Structure and principle of plate-type heat exchanger

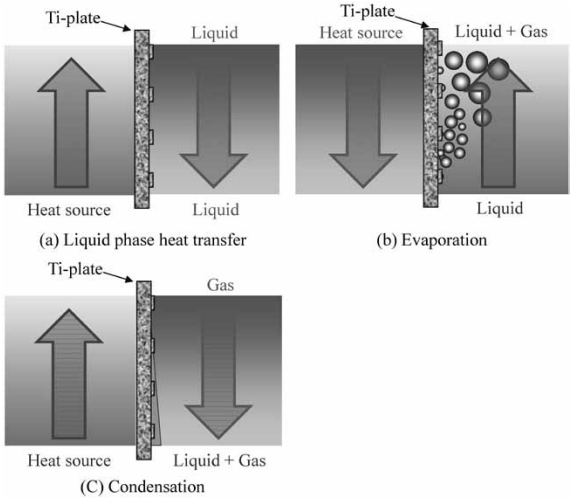


Fig. 2 Outline of heat transfer types

surface asperities, and in the processing cost and productivity.

As a way of solving these problems, Kobe Steel has proposed a method of forming fine asperities on a surface of a titanium sheet using a transfer-printing rolling technology.[4] **Fig. 3** shows the outline of this technology. Transfer-printing rolling is a technology in which a roll having fine recesses on its surface is used to roll a titanium sheet and the recesses result in asperities being formed on the surface of the sheet. A titanium sheet having fine grooves (groove width: 200 $\mu$m, mound width: 100 $\mu$m, depth: 30 $\mu$m) imparted by this technology, as shown in **Fig. 4**, has been confirmed to improve evaporation heat-transfer performance by 10% to 40% compared with commonly used smooth-surfaced sheets, when the fine grooves are arranged so as to be perpendicular to the flow.[4]

Actual PHE plates are press-formed so as to have a complex corrugated pattern, such as the herringbone pattern shown in **Fig. 5**, to improve heat-exchange efficiency and mechanical durability. The undulating shape of the plates causes the flow inside a PHE to change direction; hence it is desirable for a plate to have a shape (pattern) that allows a high heat exchange effect in all flow directions. Against this backdrop, Kobe Steel has developed a high heat-transfer titanium sheet (hereinafter referred to as "HEET®" [note]), having a polka-dot pattern in which cylindrical fine asperities are arranged in a staggered manner. The company has started mass production of the sheet. **Fig. 6** shows the surface morphology and cross-sectional structure of the coil of HEET obtained by transfer-printing rolling. The asperities are so arranged as to cover the entire surface of the sheet and have a uniform shape with their height being approximately 25 $\mu$m.

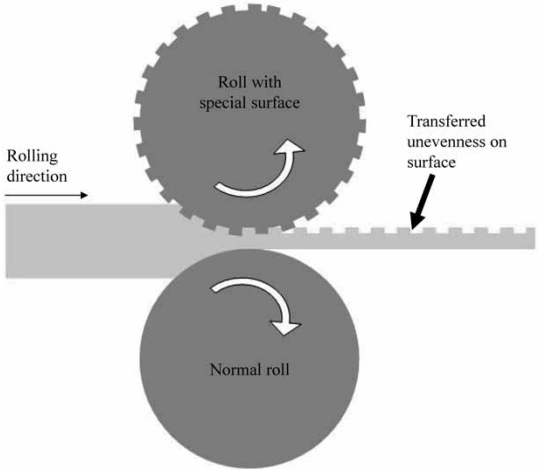


Fig. 3 Outline of transfer-printing rolling technology

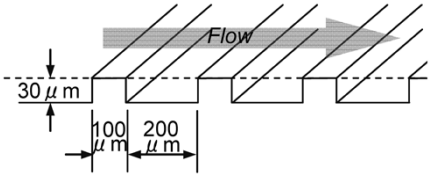


Fig. 4 Schematic of fine grooves

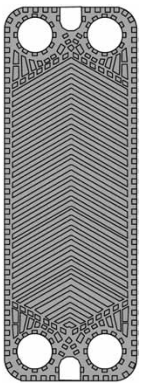

Fig. 5 Pattern diagram of typical heat exchanger plate

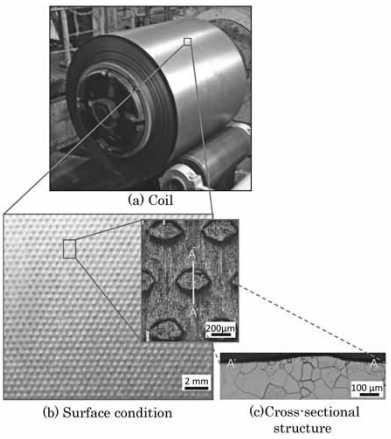


Fig. 6 Coil, surface condition and cross-sectional structure of high-heat-transfer titanium (HEET)

HEET has been adopted in the ocean thermal energy conversion (OTEC) demonstration plant on Kume Island, Okinawa, which is gaining attention as a source of renewable energy and has been in continuous operation since 2013. This paper introduces the effect of HEET in improving heat transfer performance, as well as the results of the heat-transfer performance evaluation of the PHE in the actual ocean thermal energy conversion demonstration plant.

## 1. Heat-transfer performance evaluation test

### 1.1 Sample preparation

The following explains the production method of HEET. Firstly, CP titanium (ASTM G1) material was hot- and cold-rolled into a sheet having a

[note] HEET is a registered trademark (No. 85652095) of Kobe Steel.

predetermined thickness, and cylindrical fine asperities, arranged in a staggered manner as shown in Fig. 6, were transfer-printed on a surface of the sheet. The sheet, with a thickness of 0.6mm, was subjected to heat treatment and flatness correction before being cut into a plate of HEET having a width of 80mm and length of 200mm to be used for the evaluation of thermal conductivity. A conventional smooth-surfaced normal titanium plate of the same size was also prepared as a reference material.

The HEET material was also wound to form a welded cylinder with an outer diameter of 19mm, a wall thickness of 0.6mm and a length of 550mm, whose outer surface being the sheet surface with fine asperities.

### 1.2 Method of evaluating heat transfer performance

The plates of HEET and normal titanium plate were used for the test of evaporation heat transfer. **Fig. 7** is a schematic diagram of the heat transfer test. Heat exchanger No. 1 was used as an evaporator, to which a plate of either smooth-surfaced titanium or HEET was affixed. In the case of HEET, the working fluid, Freon R134a, was made to flow on the surface with asperities, and hot water was made to flow on the other surface such that heat exchange occurred while evaporating R134a. The evaporated R134a was cooled and liquefied by a condenser to be recirculated in the apparatus. The heat-transfer surface was 50×150mm, and temperatures were measured at the inlet and outlet of each evaporator. Using the measured temperatures, heat quantity, $Q$, and logarithmic average temperature difference, $\Delta T_m$, were determined on the basis of Equations (1) and (2):

$$Q = l_h \rho_h c \ (T_{h1} - T_{h2}) \quad \cdots\cdots (1)$$

$$\Delta T_m = \frac{(T_{h1} - T_{h2})}{\ln \frac{(T_{h1} - T_2)}{(T_{h2} - T_1)}} \quad \cdots\cdots (2),$$

wherein $T_{h1}$ and $T_{h2}$ are, respectively, the input temperature and output temperature of the hot water; $T_1$ and $T_2$ are the respective input and output temperatures of R134a; $l_h$ is the flow rate of the hot water; $\rho_h$ is the density of the hot water; $c$ is the specific heat of the hot water; and $A$ is the heat-transfer area. From $Q$ and $\Delta T_m$ thus determined, the overall evaporative heat-transfer coefficient, $U$, was calculated using Equation (3).

$$U = \frac{Q}{A \Delta T_m} \quad \cdots\cdots (3)$$

The effect of HEET on condensation heat transfer and liquid-single-phase forced-convection heat transfer was also investigated. In the test of condensation heat transfer, Heat Exchanger No. 2 in Fig. 7 was used as a condenser, to which a plate of either normal titanium or HEET was fixed. In the case of HEET, the working fluid, R134a, was made to flow on the surface with asperities, and cold water was made to flow on the other surface so as to perform heat exchange. Whereas, in the test of liquid-single-phase forced-convection heat-transfer, a plate of either normal titanium or HEET was fixed on Heat Exchanger No. 1 in Fig. 7 and, in the case of HEET, cold water was made to flow on the surface with asperities and hot water was made to flow on the other surface so as to perform heat exchange. In each of the tests, temperatures were measured at the inlet and outlet of respective heat exchanger, as in the case of the evaporative heat transfer test, and the overall heat-transfer coefficient, U, was determined on the basis of Equations (1) to (3). **Table 1** summarizes the conditions of these tests.

In the case of evaporation heat transfer, an attempt was made to visualize the generation of bubbles during heat exchange, using the tube of HEET with fine asperities on its outer surface. **Fig. 8** shows the schematic diagram of the test and **Table 2** summarizes the testing conditions. A part

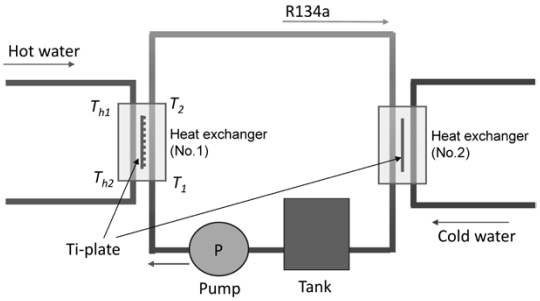

Fig. 7 Schematic diagram of heat-transfer testing apparatus

Table 1 Heat-transfer testing conditions

| | Hot water | | | Cold water | | | R134a | | |
|---|---|---|---|---|---|---|---|---|---|
| | Inlet temperature (℃) | Flow volume ($m^3$/s) | Flow rate (m/s) | Inlet temperature (℃) | Flow volume ($m^3$/s) | Flow rate (m/s) | Flow volume ($m^3$/s) | Mass flux ($kg/m^2s$) | Saturation pressure (MPa) |
| **Evaporation** | 35 | 3.0 | 0.6 | 10 | 5.0 | 0.8 | 0.1 | 23 | 0.5 |
| **Condensation** | 40 | 3.0 | 0.6 | 10 | 2.0 | 0.4 | 0.1 | 22 | 0.9 |
| **Liquid phase heat transfer** | 70 | 5.0 | 0.9 | 20 | 1.0 | 0.2 | | | |

Table 2 Visualization testing condition

| Hot water | | Cold water | | R134a | | |
|---|---|---|---|---|---|---|
| Inlet temperature (℃) | Flow volume ($m^3/s$) | Inlet temperature (℃) | Flow volume ($m^3/s$) | Evaporative temperature (℃) | Saturation pressure (MPa) | Heat flux ($kW/m^2$) |
| 40.0 | 25.0 | 6.0〜17.0 | 1.0~2.0 | 30.0〜33.0 | 0.65~0.74 | 20.0~40.0 |

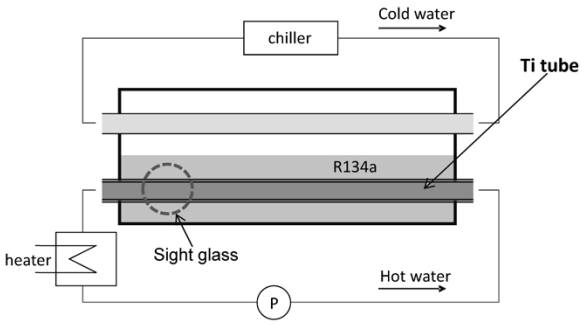


Fig. 8 Schematic diagram of visualization experiment

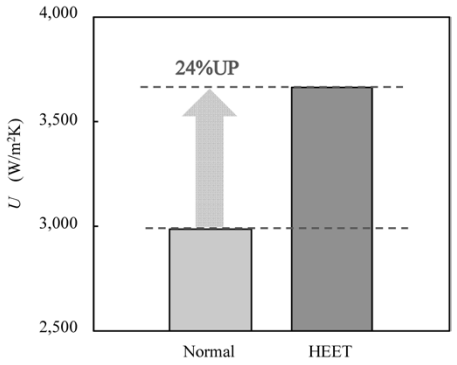


Fig. 9 Evaporation heat transfer performances of HEET and normal plate

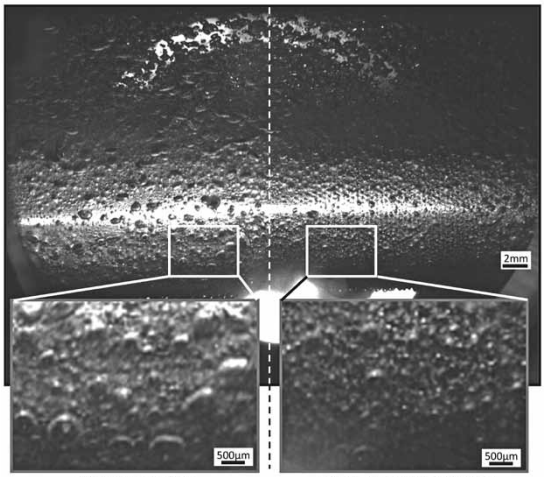


Fig.10 Boiling on surface with asperities and normal of welded tube

of the outer surface of the welded tube was polished such that the fine asperities were removed and the roughness was adjusted to be equal to that of the smooth surface. The welded tube was immersed in R134a and hot water was made to flow inside the welded tube so as to boil R134a on the outer surface of the welded tube. The testing apparatus was provided with an observation window from which the status of bubble generation from the surface with fine asperities and from the smooth surface was captured by a high-speed camera.

## 2. Results of heat-transfer performance evaluation

### 2.1 Evaporation heat transfer

**Fig. 9** shows the results of evaporative heat transfer tests performed on HEET and on smooth-surfaced plate. It has been confirmed that HEET exhibits a heat-transfer performance approximately 24% higher than that of the smooth-surfaced plate. Thanks to the fine asperities, HEET has a surface area approximately 6% greater than that of the normal sheet; however, the improvement effect of heat-transfer performance is greater than this increment of surface area. **Fig.10** shows the example of an image captured by a high speed camera showing boiling on the welded tube. To the left of the broken line at the center of the photo is the surface portion where the fine asperities were removed and the roughness was adjusted to make it equal to that of the smooth surface. It can be confirmed that a greater number of finer bubbles are generated on the surface of HEET, with its fine asperities, compared with the smooth surface. In general, boiling on a sheet surface occurs from fine scratches and cavities that serve as boiling nuclei to generate bubbles. On the other hand, in the case of HEET, the fine asperities are believed to perform the work of scratches and cavities, promote nucleate boiling and, as a result, improve the heat transfer performance.

### 2.2 Condensation and liquid-single-phase forced-convection heat-transfer

In the test of condensation heat transfer, the U values for the smooth-surfaced titanium plate and HEET are 910 $W/m^2K$ and 943 $W/m^2K$, respectively: HEET exhibits a performance improvement of approximately 6% compared with the smooth-surfaced plate. Also in the case of liquid-single-phase forced-convection heat-transfer, the U values

for the smooth-surfaced titanium plate and HEET are 2,050 W/m²K and 2,283 W/m²K, respectively: HEET exhibits a performance improvement of approximately 11% compared with the smooth-surfaced plate.

Although estimated, the mechanism of performance improvement exhibited in the test, is believed to be attributable to the increased surface area and the generation of turbulence causing the agitation of fluid inside the heat exchanger.

### 3. Verification of heat exchangers

In practical operation, a plurality of plates, each press-formed to have a complex corrugated pattern as shown in Fig. 5, are assembled into a PHE. To confirm the effect, therefore, an evaluation was conducted on a PHE having a size of approximately 700 × 2,400mm, which is the size of the PHE actually used for the ocean thermal energy conversion demonstration plant. The evaporation heat transfer performance was examined on a plate press-formed into a predetermined shape and was assembled into a heat exchanger. **Fig.11** shows the results. It has been confirmed that HEET achieves a performance improvement of approximately 20% in the actual PHE. **Fig.12** shows the 100kW-class ocean thermal energy conversion demonstration plant built in Okinawa in 2013. It has been confirmed, also in this plant, that HEET improves the evaporation heat transfer performance by 20%, verifying its effectiveness.

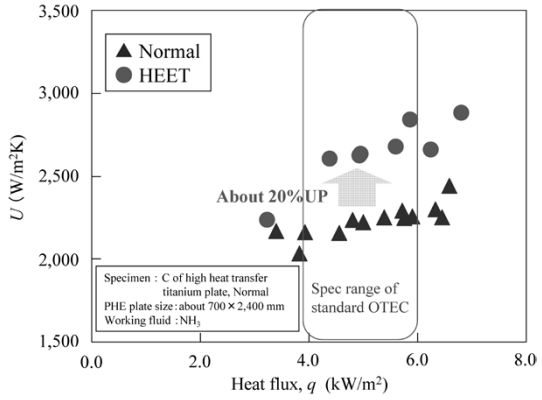


Fig.11 Relationship between overall heat transfer coefficient (U) of evaporation and heat flux (q) on PHE of OTEC

Fig.12 OTEC demonstration plant

### Conclusions

A high heat-transfer titanium sheet (HEET) exploits rolling transfer-printing technology to form fine asperities on its surface. These fine asperities improve heat transfer performance, probably by increasing the surface area and promoting nucleate boiling, and have been confirmed to improve the performance, particularly the evaporation heat transfer performance, by approximately 20% or greater.

Generally, a liquid film generated in condensation heat transfer covers the plate surface, deteriorating heat transfer performance, whereas the fine asperities on HEET are expected to promote the discharge of such a liquid film. Future studies will focus on the optimization of the shape of fine asperities and application to various types of heat exchangers.

Some of the achievements of this development have been obtained through the work on the 2011-2014 project of the New Energy and Industrial Technology Development Organization, "Technological research and development of natural energy including wind power, etc. / Research and development of ocean energy technology / Research and development of next generation ocean energy power generation technology (ocean thermal energy conversion)." We would like to express our appreciation here.

### References

1) H. Kusamichi et al. "Nihon no Chitan Sangyo to Sono Shinngijutu" AGNE Gijutsu Center Inc., 1996, p.18.
2) Y. Ikegami et al. Proceedings of 37th National Heat Transfer Symposium of Japan, 2000, p.825.
3) Furberg et al. ASME Journal of Heat Transfer. 2009, Vol.131, p.101010.
4) A. Okamoto et al. R&D Kobe Steel Engineering Report. 2010, Vol.60, No.2, p.60
5) The Japan Society of Mechanical Engineers. JSME test series, Heat Transfer Engineering. Maruzen Publishing Co., 2005, p.123.
6) S. Koyama et al. Refrigeration, 2000, Vol.75, No.874, p.654.

# Dust Core with Low Core-loss for High-frequency Applications

Hirofumi HOJO*1, Tomotsuna KAMIJO*1, Yuji TANIGUCHI*1, Nobuaki AKAGI*1, Hiroyuki MITANI*2

*1 Takasago Steel Powder Plant, Steel Powder Div., Iron & Steel Business
*2 Research & Development Planning Dept., Technical Development Group

*Dust cores produced by compacting insulation-coated powder allow a high degree of freedom in shaping and are expected to be useful for the downsizing of parts; however, they have issues of energy loss, or core loss. A study has been conducted on reactors and choke coils, which are used at relatively high frequencies, to improve their core-loss characteristics by focusing on the particle size of the powder. As a result, "MAGMEL MH20D" powder was developed by designing powder, taking into account, not only the magnetic characteristics, but also power characteristics, and by combining Kobe Steel's conventional techniques of heat-resistant coating and grain coarsening. The newly developed powder has improved the core loss, reducing it to 30% of that achieved by conventional products, and has been adopted for the reactors of solar-power systems.*

## Introduction

Electromagnetic components are required to have higher efficiency, to save energy and reduce the environmental burden, and smaller sizes to save space. Laminated cores consisting of electrical steel have conventionally been used for the iron cores of electromagnetic components; however, downsizing has been limited due to the anisotropy intrinsic to laminated structure and to shape limitations.

Dust cores, on the other hand, being manufactured by compacting powder, have no anisotropy and less restriction as to shape; thus their downsizing is expected. In fact, dust cores made of Fe-Si based alloy powder have been adopted for the booster reactors of hybrid vehicles.[1)] With the beginning of a subsidy program for solar power generation as a part of the Renewable Energy Promotion Policy, the demand for solar-power generation systems has been increasing, and this has promoted the application of dust cores for downsizing and improving the efficiency of components used in power generation systems.

Commercially pure (CP) iron powder, a raw material of dust cores, has higher compressibility and greater saturated magnetic flux density compared with alloy powders, which makes further downsizing of components possible. Its soft particles ensure excellent compactibility and have the advantage of being easy to handle in the process of core manufacturing. On the other hand, there has been an issue as to how to reduce core loss, or energy loss.

In order to reduce the core loss of CP-iron-based dust cores, a study was conducted on the effect of powder particle size on core loss. Knowledge gained through the research, as well as coating technology and crystal grain control technology established so far, has been used to develop "MAGMEL MH20D" powder, which has a core loss improved by 30% over that of conventional CP iron powder. Its core loss characteristics are comparable to those of some of the Fe-Si-based alloy powders. MAGMEL MH20D has been adopted as a raw material for the reactors of power conditioners used in solar power generation.

## 1. Challenges and developmental approaches for CP-iron-based dust core

The characteristics required for magnetic core material are high magnetic flux density and low core loss. As described above, dust cores based on CP iron powder have the disadvantage of significant core loss, despite their possessing magnetic flux densities higher than those of alloy powders. Core loss mainly consists of eddy-current loss and hysteresis loss. Eddy-current loss is a joule loss caused by eddy current generated when magnetization fluctuates, while hysteresis loss is an energy loss caused when a magnetic material is magnetized. **Fig. 1** illustrates these control factors. Dust cores have the capability of suppressing the inter-particle eddy current, which flows throughout the component as a result of insulation coating on the particle surfaces. In high-frequency regions, however, the proportion of eddy-current loss is

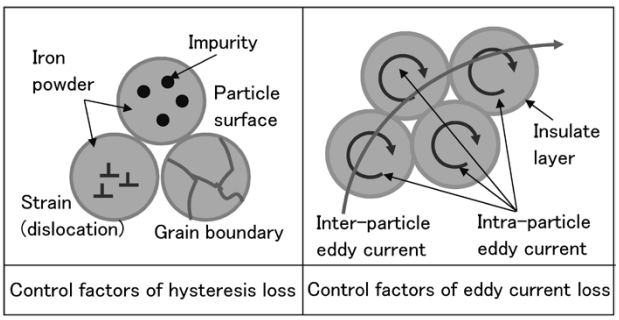


Fig. 1 Control factors of iron loss

increased as a whole loss. Therefore, in addition to inter-particle eddy current, intra-particle eddy current must also be suppressed. In the case of alloy powders, intra-particle eddy current is suppressed by increasing impedance by the use of additive elements, whereas, in the case of CP iron powder, it is difficult to control impedance with additive elements. Therefore, the only way of decreasing intra-particle eddy current is to decrease the particle size and thus restrict the flowing range of eddy current. Decreasing the particle size, however, increases the surface area, which can cause hysteresis loss to increase. Therefore, it is important to study both effects to determine the optimum particle size.

To this end, the effect of the particle size of iron powder on the core loss and powder characteristics was studied so as to determine the optimum particle size for achieving low core loss in the high-frequency region. The subsequent sections include the introduction of "MAGMEL MH20D" for high-frequency application, which was developed on the basis of the study results.

## 2. Investigative method

Kobe Steel's atomized CP iron powder was sieved to remove coarse particles providing raw iron powders having an average particle size of 30$\mu$m to 85$\mu$m (D50: the value of the particle diameter at 50% in the cumulative distribution obtained by sieving.) Processing liquid mainly comprising phosphoric acid was used to form an inorganic coating on the particle surfaces of these iron powders. Subsequently, it was coated with silicone resin to produce insulation-coated iron powder with an inorganic/organic double layer.[2] Each of the coated iron powders was filled into a powder-lubricated die and the powder-filled die was heated to 303K to form ring compacts ($\phi$45mm OD; $\phi$33mm ID; 6mm H) under a pressure of 1,176MPa. These compacts were heat-treated at 873K for 1.8 ks in a nitrogen atmosphere. Each iron-loss measurement sample was prepared by forming a primary coil and a secondary coil, winding 50 and 10 turns of wire, respectively, on the corresponding heat-treated ring compact; while each BH-curve measurement sample was prepared by forming a primary coil and a secondary coil, winding 400 and 25 turns of wire, respectively, on the corresponding heat-treated ring compact.

The flow rate of coated powder was measured in accordance with the JIS Z 2502：2012, "Metallic powders-Determination of flow rate by means of a calibrated funnel." The BH curve of each sample was measured up to a maximum excitation magnetic field of 10 kA/m; while the core loss was measured for an excitation magnetic flux density of 0.1 T under a varying frequency of 1 k to 100 kHz.

## 3. Results and discussion

### 3.1 Effect of iron-powder particle size on magnetic characteristics

The eddy-current loss of a dust core consists of inter-particle eddy-current loss, due to eddy current flowing throughout the core, and intra-particle eddy current loss, due to eddy current flowing inside each particle (Fig. 1.) The inter-particle eddy current loss can be suppressed by providing insulation coating on iron powder particles, whereas intra-particle eddy current loss can be controlled by sizing the particle, i.e., changing the area where electric current flows. However, this changes the surface area of particles at the same time. The surface area of particles is one of the factors affecting hysteresis loss; hence both the eddy current loss and hysteresis loss must be taken into account in the effect of particle size.

**Fig. 2** (a) shows the relationship between average particle size and core loss. It has been clarified that the core loss decreases with decreasing particle size. This trend is more pronounced at higher frequencies. On the basis of the frequency dependence of core loss, the eddy current loss was separated from hysteresis loss and the results are shown in Figs. 2 (b) and (c.) The eddy-current loss decreases with decreasing particle size, as in the case of core loss, whereas hysteresis loss changes only slightly with the change of particle size. This shows that the core loss decreases predominantly with decreasing eddy-current loss.

**Fig. 3** shows the dependence of coercivity on particle size. The coercivity increases with decreasing particle size, indicating that decreasing particle size, i.e., increasing surface area of particles, is a factor inhibiting the migration of domain walls.

The coercivity is generally known to be proportional to hysteresis loss, and there is a discrepancy between the particle-size dependence of hysteresis loss shown in Fig. 2 and the particle-size dependence of coercivity shown in Fig. 3. This discrepancy can be explained on the basis of the excitation condition of each characteristic measurement. The excitation condition of core-loss measurement is 0.1 T in terms of excitation magnetic flux density. On the other hand, in the case of coercivity measurement, which is a static magnetic measurement, the excitation magnetic field is

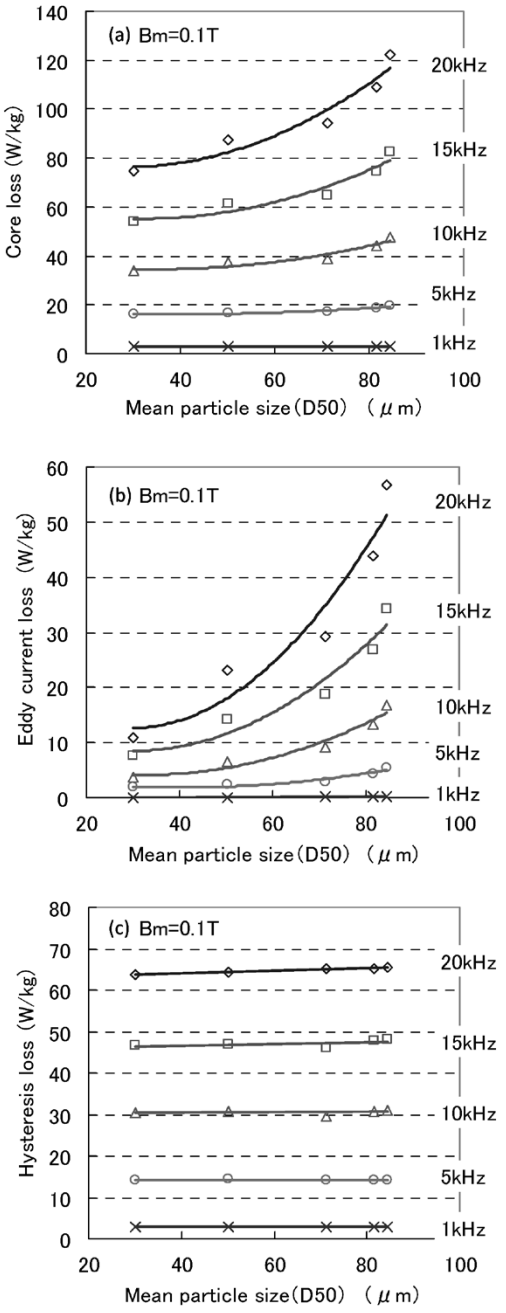


Fig. 2 Relationship between particle size and core loss
a) Core loss, b) Eddy current loss, c) Hysteresis loss

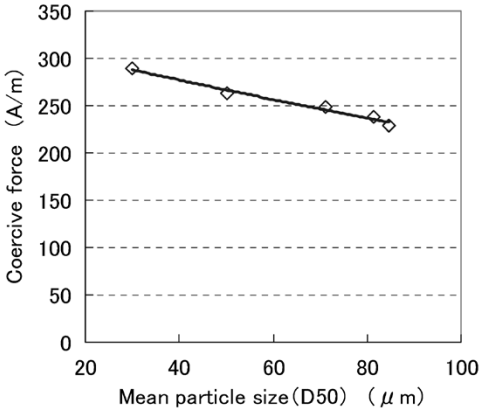


Fig. 3 Relationship between particle size and coercivity

10 kA/m. These excitation conditions are plotted on a BH curve, as shown in **Fig. 4**. The magnetic flux density for the coercivity measurement is approximately 1.4 T, which is greatly different from that of the core-loss measurement. This is indicative of a difference in the migration of domain walls: the domain walls barely migrate during the core-loss measurement; whereas, they migrate widely during coercivity measurement, since magnetization close to saturation occurs. It is believed that, when the migration of domain walls is small, the intra-particle factor inhibiting the domain wall migration governs; however, as the domain wall migration becomes greater, the surface begins to have a more significant effect. **Fig. 5** shows the particle size dependence of coercivity under different excitation conditions. As shown in this figure, no particle size dependence of coercivity is observed for the low excitation magnetic flux density of 0.1 T.

From the above, it is believed that, under the excitation condition in question (approximately 0.1 T), only the decreasing effect of eddy-current loss can be observed without the increase in hysteresis-loss due to decreasing particle size.

### 3.2 Effect of particle size of iron powder on powder characteristics

The flow rate is one of the key characteristics

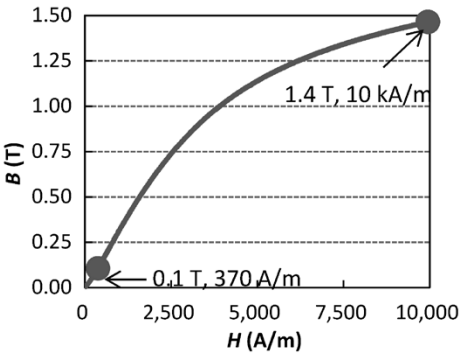


Fig. 4 Excitation condition

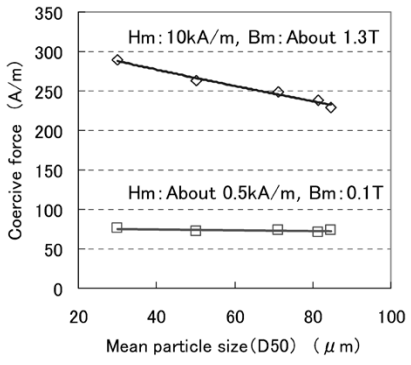


Fig. 5 Relationship between particle size and coercivity

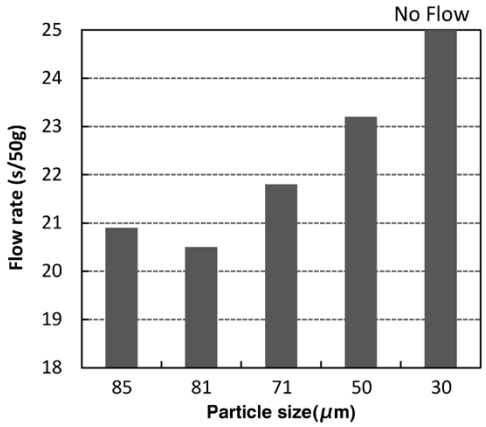


Fig. 6 Relationship between particle size and flow rate

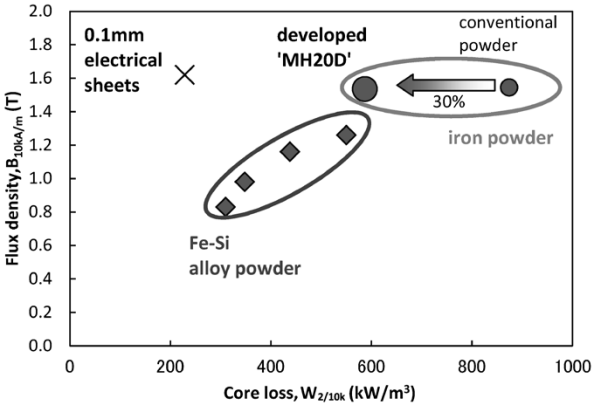


Fig. 7 Comparison of material characteristics

affecting the productivity of component production, involving storage, handling and die filling. In general, finer powder has a larger surface area, enhancing adhesion and cohesion while deteriorating the flow rate. This, therefore, is a trade-off relationship with the eddy-current loss described in the previous section. **Fig. 6** shows the relationship between the particle size and flow rate, in which the particle size was changed by sieving. The flow rate increases (the fluidity deteriorates) with decreasing particle size, and no flow occurred for the average particle size of 30 $\mu$m. On the basis of this result, the particle size of approximately 50 $\mu$m has been adopted as the practical minimum that allows the flow through the Hall flow meter, to achieve the balance between eddy-current loss and flow rate.

## 4. Summary

Targeting the high-frequency low magnetic-flux density region, a study was conducted on the particle size of CP-iron powder suitable for dust core. MAGMEL MH20D has been developed on the basis of the study, while exploiting "highly heat-resistant insulation coating technology"[2] and "crystal grain coarsening technology for powder."[3] **Table 1** summarizes the characteristics of a heat treated core, and **Fig. 7** compares the characteristics of MAGMEL MH20D with that of Fe-Si based alloy powder.[4] By combining these technologies, the core loss, which having been an issue, has been decreased by approximately 30%, while the high magnetic flux density, an advantage of CP iron powder, is maintained. This has realized core-loss characteristics that are comparable with those of some Fe-Si based alloy powders. The newly developed powder has been adapted to the reactors of power conditioners used in solar power generation.

## Conclusions

It has been confirmed that the newly developed material can expand the applicability of CP iron powder to applications in which electrical steel sheets have conventionally been used. The advantages of dust cores over laminated cores include high yield, i.e., no material being left over due to punching, which contributes to reduced cost and resource saving. When compared with alloy powders, the newly developed powder has higher compressibility, which decreases compacting pressure by approximately 20% to 50%, saving energy cost. Although the application is currently limited to solar power generation systems, this powder is expected to be applied, for example, to inverters (general purpose, on-vehicle) using similar booster circuitry.

Table 1 Properties of 'MH20D' core

| Grade | Density | DC Magnetic properties | | | AC Magnetic Properties | | | Mechanical Properties |
|---|---|---|---|---|---|---|---|---|
| | | Flux Density $B_{10kA/m}$ | Maximum Permeability | Coercive force | Core Loss $W_{1/10k}$ | Hysteresis Loss $Wh_{1/10k}$ | Eddy current Loss $We_{1/10k}$ | Transverse Rupture Strength |
| | (Mg/m$^3$) | (T) | | (A/m) | (W/kg) | (W/kg) | (W/kg) | (MPa) |
| MH20D | 7.44 | 1.46 | 224 | 224 | 20.1 | 15.2 | 4.9 | 77 |

* Compaction: 1,176MPa with DWL compaction method at 403K
Heat treatment: 873K for 1.8ks in $N_2$

## References


1) S. Sugiyama et al. *SOKEIZAI*, 2010, Vol.51, No. 12, pp. 24-29.
2) Kobe Steel, "*IRON BASED SOFT MAGNETIC POWDER FOR DUST CORE, ITS PRODUCTION METHOD, AND DUST CORE*" Japanese Patent No. 4044591, 2006-09-11.
3) H. Hojo et al. *PM2010 POWDER METALLURGY World Congress & Exhibition. 2010*.
4) S. Takemoto. *Electric Furnace Steel*, 2011, Vol. 82, No. 1, pp. 57-65.

# Highly Heat-Resistant Aluminum Alloy "KS2000"

Toshiyuki TANAKA*1, Yasuki KAMITAKAHARA*2

*1 Casting & Forging Research Sect., Daian Plant, Aluminum & Copper Business
*2 Quality Assurance Sect., Daian Plant, Aluminum & Copper Business

*Rotating/sliding components that operate at elevated temperatures, such as impellers and pistons, require aluminum alloys having a heat resistance higher than that of conventional aluminum alloys. Kobe Steel has optimized the additive elements to finely disperse precipitates that improve hightemperature properties, the homogenization conditions to finely disperse crystallized products and the conditions of plastic deformation to refine grain size. The optimizing of the composition and processing conditions resulted in the development of a new aluminum alloy, "KS2000," having an excellent heat resistance compared with the conventional 2618 alloy.*

## Introduction

Aluminum alloy has a density of approximately 2.7 g/cm$^3$, which is about 1/3 that of iron, along with high specific strength (strength/specific gravity), and is easy to process by various methods including casting, forging, rolling and machining. Exploiting these advantages, aluminum alloys are being used in accordance with the properties required for transportation equipment, such as railway vehicles, motor vehicles and ships, as well as for various machinery parts and engine parts. Among these, mechanical members that rotate at high speed or slide at temperatures above the ambient temperature employ aluminum alloys having high temperature properties; such members include impellers used in generators/compressors, vacuum-pump rotors and engine pistons. For example, Al-Cu-Mg-Fe-Ni based 2618 alloy is widely used as an aluminum alloy in high-temperature environments and is one of the typical heat-resistant aluminum alloys applied, for example, to turbocharger impellers of various sizes, ranging from automobiles to vessels.

In recent years, there has been a trend toward improving the fuel efficiency of transportation equipment, which has led to turbochargers having higher compressibility and a higher flow rate. As a result, turbines are required to rotate at speeds higher than those of the conventional products, and intake-side impellers, which produce compressed air, are exposed to higher temperatures and load-pressures, requiring an aluminum alloy with even higher heat resistance.

This paper introduces heat-resistant aluminum alloy, KS2000, which was developed to meet these needs.

## 1. Features of highly heat resistant aluminum alloy, "KS2000"

The heat resistant aluminum alloy designated as 2618 alloy is a widely-used wrought alloy registered with the Aluminum Association in 1954. This alloy is designated as RR58 in the UK and AU2GN in France and was used for the structural members of the Concorde supersonic airliner. Kobe Steel applied this alloy to a hydraulic-equipment housing in the late 1960s and has applied it to automotive pistons and turbocharger impellers, etc., since the 1980s. The alloy is still being widely used as a stock material for items produced at Kobe Steel's Daian plant.

As described above, Kobe Steel began the development of heat-resistant aluminum alloy around the year 2000 in response to the increasing need for an aluminum alloy with high-temperature resistance; this resulted in the development of KS2000.[1)-4)] Its features are as follows:

1) The optimization of additive elements such as Cu, Ag and Mg has allowed the fine dispersion of Ω-phase precipitates, which improve high temperature properties, enabling the improvement of high temperature strength and creep properties to an extent that exceeds those of 2618 alloy.
2) The refinement of constituents by optimizing homogenization conditions, as well as forging conditions, has led to the discovery of process conditions that improve high-temperature fatigue properties.

## 2. Creep properties

Turbochargers for marine engines and diesel generators continue to rotate under high loads. As a result, each impeller blade is subjected to a large stress generated by centrifugal force, while the temperature on the intake side increases to a figure between 100 and 200℃, causing a concern about creep deformation. Therefore, creep is a key characteristic of the material used for intake-side impellers.

The composition of the newly developed material, aimed at improving high-temperature strength, has been adjusted on the basis of the concept that the addition of Cu and Mg increases the density of fine Al-Cu based precipitates and

the addition of Ag promotes the formation of precipitates having excellent high-temperature properties. **Table 1** shows typical compositions representing the features of 2618 alloy and KS2000. Also, **Fig. 1** shows the transmission electron micrographs of 2618 alloy and KS2000, both after T61 aging. Regarding the formation of precipitates from a supersaturated solid solution of Al-Cu-Mg based alloys, the precipitation process depends on the Cu/Mg ratio (weight ratio) of the alloys.[5] More specifically, the $\theta$-phase precipitates when Cu/Mg > 8, the *S*-phase precipitates when Cu/Mg < 1.5, and the competitive precipitation of three phases, $\alpha$, $\theta$ and *S*, occurs when 1.5 < Cu/Mg < 8. The 2618 alloy has a Cu/Mg ratio of approximately 2, and most precipitates are *S*'-phase. In the micrograph of 2618 alloy in Fig. 1 (a), *S*'-phase is observed extending in the $[1\bar{1}0]$ and $[00\bar{1}]$ directions.

KS2000, on the other hand, has a Cu/Mg ratio of approximately 20, which is in the region where $\theta$'-phase generally precipitates; but KS2000 exhibits different precipitation behavior because of the addition of Ag. As shown in Fig. 1 (b), in addition to the $\theta$'-phase extending in the $[1\bar{1}0]$ and $[00\bar{1}]$ directions, a new precipitation phase extending in the $[1\bar{1}\bar{2}]$ and $[\bar{1}1\bar{2}]$ directions is observed. This precipitation phase is called $\Omega$-phase and is believed to increase the alloy's strength and heat resistance.[6),7)] Regarding the precipitation of $\Omega$-phase, Hono proposed heterogeneous nucleation of Ag-Mg co-clusters on the basis of his analysis using a three-dimensional atom probe (3DAP), etc.[8)] More specifically, $\theta$-phase and $\Omega$-phase are thermodynamically equivalent; however, $\theta$-phase grows incoherently with $\alpha$-phase in non-specific directions, whereas $\Omega$-phase is an equilibrium phase that homogeneously precipitates coherently with the {111} plane of the $\alpha$-phase, in which Ag-Mg co-clusters serve as precursors. Thus, $\Omega$-phase is considered to improve the high-temperature properties of the alloy, since it is an equilibrium phase having excellent stability at high temperatures and is coherent with the $\alpha$-phase, as described above.

**Fig. 2** shows the transmission electron micrographs of 2618 alloy and KS2000 after T61 artificial aging and subsequent exposure at 180℃ for 400 h. In the case of 2618 alloy shown in Fig. 2 (a), *S*'-phase is coarsened into a lath-like shape, indicating that the precipitation-strengthening effect of *S*'-phase has been decreased by the heating. On the other hand, in the case of KS2000 shown in Fig. 2 (b), there is no significant change in the size of $\Omega$-phase from the T61 as-aged condition, despite some coarsening of $\theta$'-phase. **Table 2** summarizes the yield strength of 2618 alloy and KS2000 at ambient temperature and after heating at 150℃ for 100h, along with their

Table 1 Typical chemical composition (wt.%)

| Alloys | Fe | Cu | Mg | Ni | Ag |
|---|---|---|---|---|---|
| 2618 | 1.0 | 2.5 | 1.5 | 1.0 | — |
| KS2000 | — | 6.5 | 0.3 | — | 0.5 |

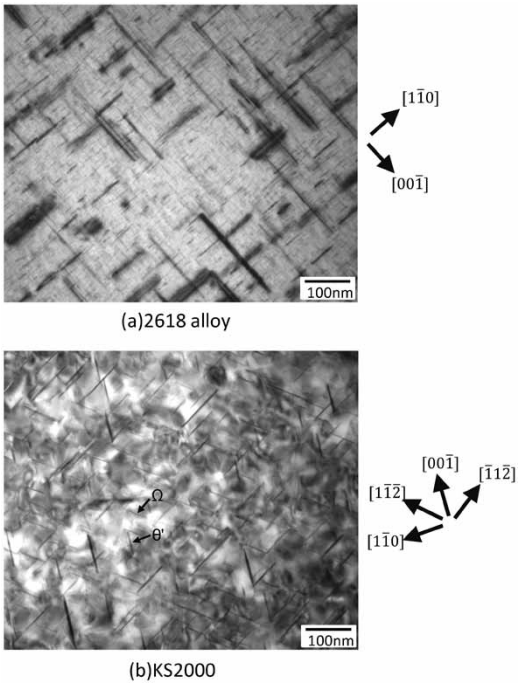


Fig. 1 Transmission electron micrographs after T61 artificial aging

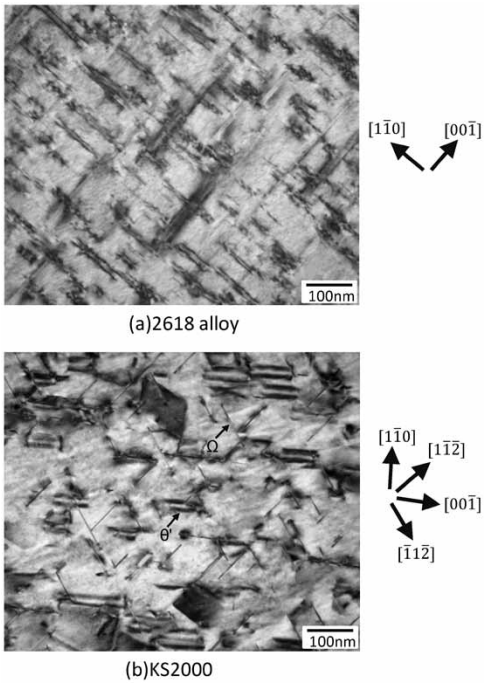


Fig. 2 Transmission electron micrographs after T61 artificial aging followed by exposure at 180℃-400h

Table 2 Properties of yield strength and creep of each alloy

| Alloys | | 2618-T61 | KS2000-T61 |
|---|---|---|---|
| Yield strength (MPa) | RT | 360 | 430 |
| | 150℃, 100h | 330 | 375 |
| Creep rupture time (h) | 180℃, 235MPa | 165 | 710 |

creep properties under the testing conditions of 180℃, 235MPa. As shown in Table 2, the creep-rupture time of KS2000 is longer than that of 2618 alloy. Thus, the Ω-phase, having high thermal stability, suppresses the intra-granular slip, enabling KS2000 to exhibit excellent high-temperature tensile properties and creep properties.

## 3. High-temperature fatigue properties

Turbochargers are used not only in ships and generators, but also in automobiles. Unlike the turbochargers in ships and generators, which continue to rotate under steady-state conditions, automotive turbochargers are subjected to significant variations of rotation in coordination with the engine output set by accelerator operation. Therefore, their impellers are exposed to stress variations and stress amplitudes associated with acceleration and deceleration, thus calling for fatigue strength at high temperatures. Thus, the materials used for rotating bodies are required to have not only creep properties, but also a certain level of high-temperature fatigue properties.

As described in the previous section, KS2000 contains a larger amount of Cu and a decreased amount of transition elements such as Fe and Ni. In addition, the composition with added Ag has improved the creep properties, thanks to the precipitation of the Ω-phase. In terms of fatigue strength, however, KS2000 has been found inferior to 2618 alloy at both ambient and high temperatures as long as the alloy is simply forged and heat-treated after casting. The following reasons are considered: i) KS2000 contains Cu in an amount exceeding the maximum solubility limit, resulting in the coarsening of constituents, which provide origins of fatigue fracture; and ii) coarse crystal grains are formed due to the small amount of transition element, which is a factor reducing fatigue strength.

Considering the high temperature applications of KS2000, it is required to achieve fatigue properties that are at least equivalent to those of 2618 alloy, while maintaining the creep properties that have been obtained. To this end, as described in the following section, optimum manufacturing conditions have been devised to improve the high-temperature fatigue properties of KS2000.

### 3.1 Refinement of constituents

**Fig. 3** shows scanning electron micrographs of 2618 alloy and KS2000, in which the latter was subjected to axial fatigue testing before the constituents were refined, and each micrograph was captured around the starting point of the fatigue fracture in axial fatigue tests. In 2618 alloy, the fracture originates in a cleavage crack, an indication of intra-granular fracture, whereas in KS2000, the origin has turned out to be a constituent particle. **Fig. 4** shows the optical micrographs of both fatigue test samples. In KS2000, the constituents are larger than those in 2618 alloy and their distribution is inhomogeneous. In addition, energy dispersive X-ray spectroscopy (EDX) has shown that the constituents observed in KS2000 are Al-Cu based. According to Kuroki et al., refining the eutectic Si/Fe-based compound in an aluminum alloy casting improves the fatigue strength.[9] Against this backdrop, a study was conducted to refine constituents by raising the temperature of homogenization so as to dissolve Al-Cu base constituents into the matrix phase. In the case of Al-Cu based alloys, including KS2000, excessively high soaking temperature results in eutectic melting. Therefore, the soaking temperature has been optimized on the basis of Thermo-Calc, a thermodynamics equilibria calculation software, and the results of a heating test performed on small test pieces. The reduction of constituents has

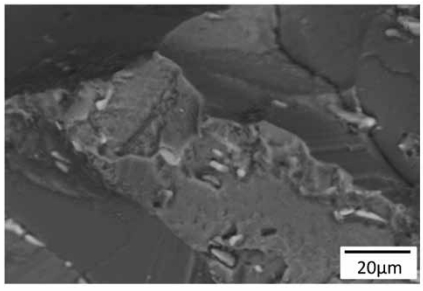


(a) 2618 alloy

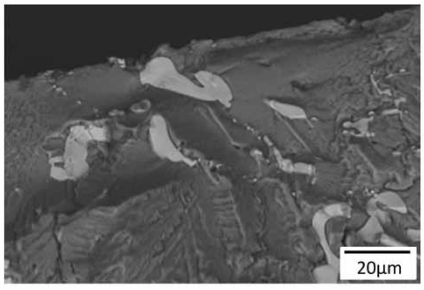


(b) KS2000 under unoptimized condition of homogenization

Fig. 3 Scanning electron micrographs around starting point of fatigue fracture of axial fatigue tests

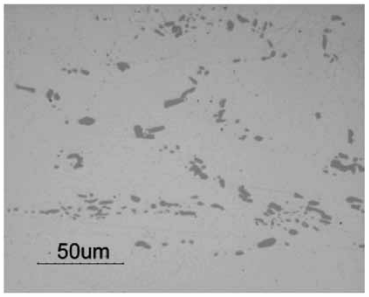


(a) 2618 alloy

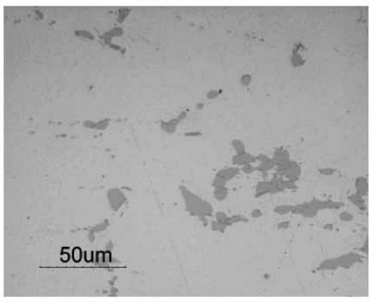


(b) KS2000 under unoptimized condition of homogenization

Fig. 4 Optical micrographs of fatigue testing sample

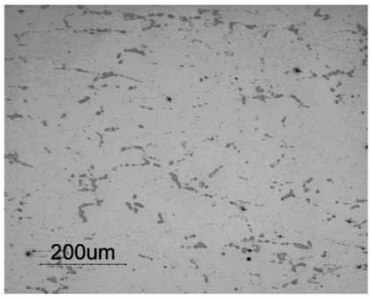


(a) Unoptimized condition of homogenization

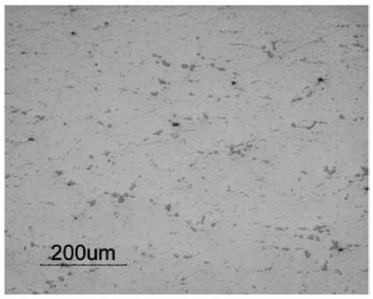


(b) Optimized condition of homogenization

Fig. 6 Optical micrographs of KS2000 forging

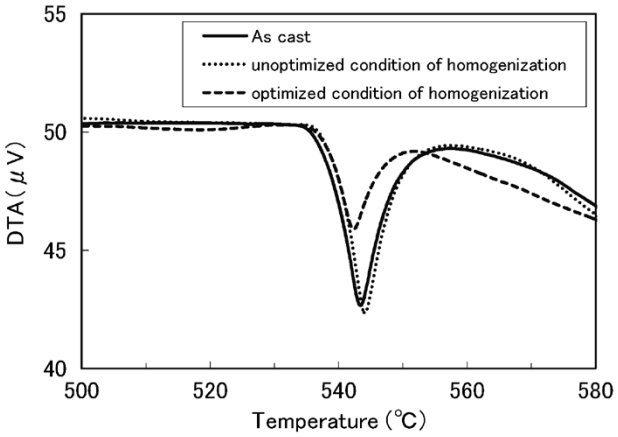


Fig. 5 Differential thermal analysis in each material condition

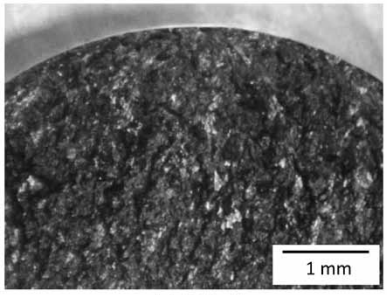


(a) 2618 alloy

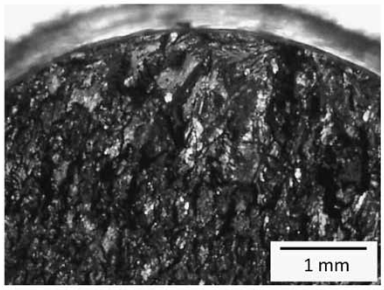


(b) KS2000 under unoptimized condition of forging

Fig. 7 Fractograph in rotary bending fatigue tests

been evaluated by differential thermal analysis. **Fig. 5** shows the results of differential thermal analysis performed on the as-cast sample, along with the samples from before and after the soaking temperature optimization. The endothermic peak before soaking temperature optimization is not much different from the peak for the as-cast, and the endothermic peak is decreased by the optimization of the soaking temperature. This indicates that a certain portion of Al-Cu based constituents has dissolved into the matrix phase, decreasing the constituents. **Fig. 6** shows the optical micrographs of KS2000 forgings before and after the optimization of the soaking temperature. In comparison with Fig. 6 (a), before the optimization, Fig. 6 (b), after the optimization, shows more disrupted networks of constituents, which are reduced in size. Therefore, it has been clarified that appropriate adjustment of soaking temperature enables the distribution control of Al-Cu based constituents.

### 3.2 Refinement of crystal grains

Rotary bending fatigue tests were conducted on a 2618 alloy test sample and KS2000 test sample, the latter having refined constituents as described in the previous section. **Fig. 7** shows the fatigue fracture surfaces of these samples. It is shown that both the alloys exhibit cleavage cracking, with KS2000 exhibiting more remarkable cleavage cracking.

**Fig. 8** shows the optical micrographs of crystal grains. Some of the crystal grains of KS2000 are larger than 1mm, while the grains of 2618 alloy fall between approximately 100 and 200 $\mu$m. Hatanaka et al. studied the relationship between the crystal grain and fatigue strength of Al-2.4Mg alloy and showed that refined crystal grains improve fatigue strength.[10] It is generally believed that, in the high-cycle range of a fatigue test performed with low stress, the propagation of micro-cracks smaller than 1mm is a major factor in the fatigue. Suresh concluded that such micro-cracks are greatly affected by crystal grains, and smaller crystal grains hinder the propagation of micro-cracks and extend the fatigue life.[11]

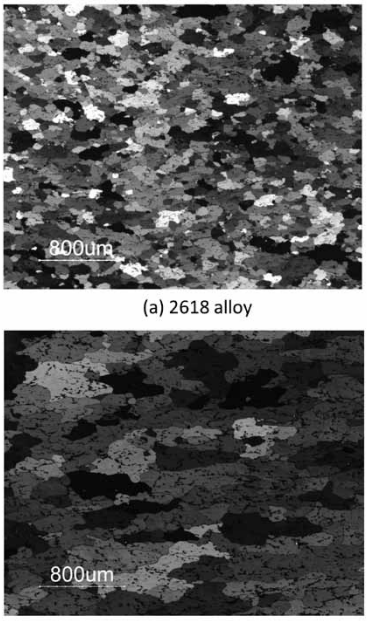

(a) 2618 alloy

(b) KS2000 under unoptimized condition of forging

Fig. 8 Optical micrographs of crystal grain

Thus, a study has been conducted to improve the fatigue strength of KS2000 by crystal grain refinement. Crystal grain refinement is effectively accomplished by adding transition elements to suppress the coarsening of crystal grains, or by increasing the dislocation density through plastic deformation. The addition of transition elements to the present alloy, however, makes the alloy more quench sensitive, making it difficult to achieve the required strength in large products, and increases the number of constituents, which may lead to decreased fatigue strength. Therefore, the study focused on the refinement of crystal grain by optimizing the forging conditions for applying plastic deformation.

The change in grain size during plastic deformation correlates with the dislocation density inside the material, and dislocation density depends on the amount of strain, strain rate and forging temperature. Hence a small hot-compression tester was used to study the relationship between the forging condition and grain size to understand how these factors affect grain size. **Fig. 9** shows how the forging temperature and equivalent plastic strain influence grain size after T61 artificial aging. These photographs show that the greater the equivalent plastic strain and the lower the forging temperature,

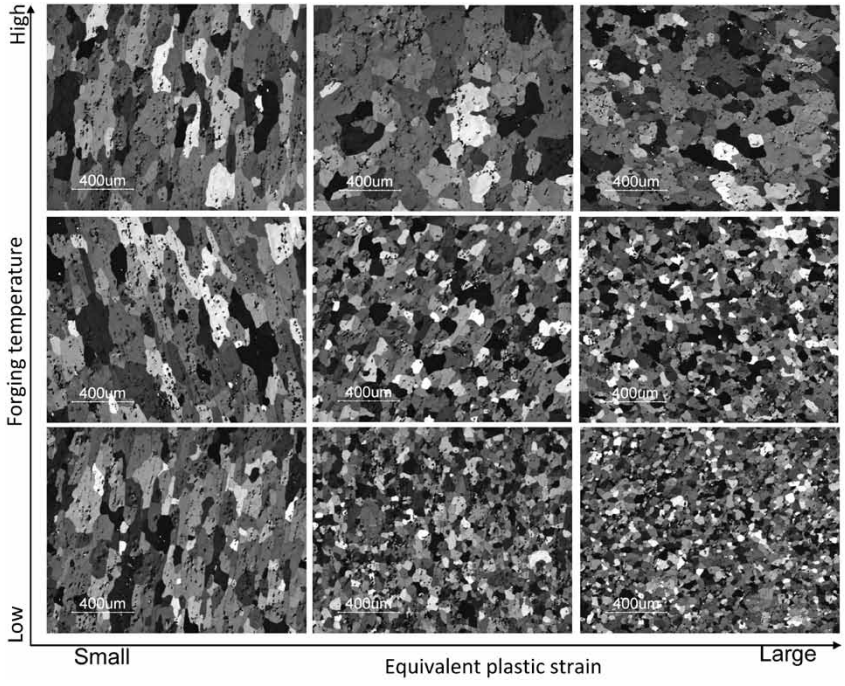


Fig. 9 Influence of crystal grain-size after T61 artificial aging in forging conditions

the finer the grain size becomes. On the basis of the test results shown in Fig. 9, further adjustment has been made in the mass manufacturing process, which has led to the establishment of optimum forging conditions for controlling the grain size of KS2000.

**Fig. 10** shows a fatigue fracture surface of KS2000 after the optimization of homogenization and forging conditions. **Fig. 11** shows the scanning electron micrographs of a fracture surface of samples before and after the optimization of forging conditions. The sample after the optimization of forging conditions exhibits a finer grain size, as fine as that of 2618 alloy shown in Fig. 7 (a), along with finer cleavage cracks, compared with the sample before the optimization.

**Table 3** summarizes the fatigue strength of 2618 alloy, as well as KS2000 before and after the optimization. As described above, a process that makes the fatigue strength of KS2000 comparable to

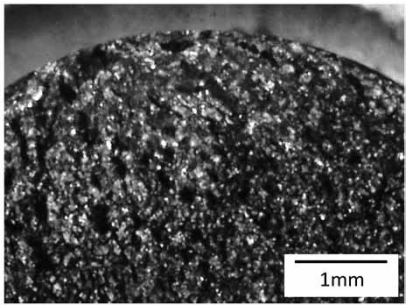


Fig.10 Fractograph in rotary bending fatigue test under optimized condition of forging

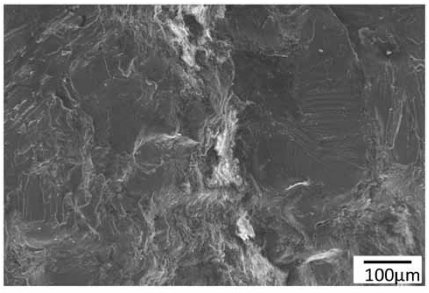


(a) Unoptimized condition of forging

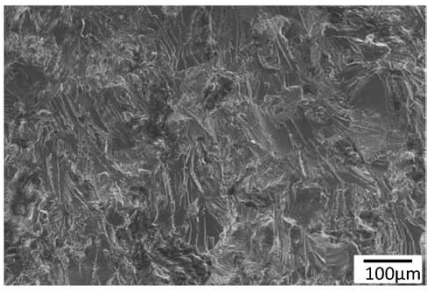


(b) Optimized condition of forging

Fig.11 Scanning electron micrographs around starting point of fatigue fracture of rotary bending fatigue tests

Table 3 Fatigue strength of each alloy

| Alloys | | 2618-T61 | KS2000-T61 | |
|---|---|---|---|---|
| | | | Unoptimized condition of forging | Optimized condition of forging |
| Fatigue strength (MPa) | RT, $10^7$cycles | 160 | 150 | 165 |
| | 180℃, $10^7$cycles | 120 | 110 | 120 |

that of 2618 alloy has been developed by:

i) the refinement of constituents through the optimization of homogenization conditions, and
ii) the refinement of grain size through the optimization of forging conditions.

## Conclusions

A process has been established to fully realize the properties of the newly developed KS2000, as a result of the composition adjustment for high-temperature properties and the optimization of homogenization and forging conditions for fatigue strength. The requirement for high-temperature properties is expected to become more stringent for aluminum alloys used in products such as rotating bodies. We will strive to develop materials meeting the customers' needs, approaching them from the aspects of both composition and process.

## References


1) *Japanese Patent No. 3997009 (2007)*
2) *Japanese Patent No. 4058398 (2008)*
3) *Japanese Patent No. 4088546 (2008)*
4) *Japanese Unexamined Patent Application Publication No. 2013-14835*.
5) Journal of Japan Institute of Light Metals. "*ALUMINIUM NO SOSHIKI TO SEISHITU*". 1991, pp.192-216.
6) I. P. Polmear. *Trans. Metall.* Soc. AIME. 1964, p.1331.
7) J. A. Taylor et al. *Metal Sci.* 1978, pp.478-482.
8) K. Hono. *Metal.* 2003, Vol.73, No.3, pp.201-209.
9) Kuroki et al. *Journal of Japan Institute of Light Metals.* 2000, Vol.50, No.3, pp.116-120.
10) Hatanaka et al. *Journal of the Japan Institute of Metals.* 1976, Vol.40, No.10, pp.1016-1024.
11) S. Suresh. *Fatigue of materials. Second edition.* Baifukan Co., Ltd., 2005, pp.535-539.

# Martensitic Steel Sheets of 1300 and 1500MPa Grades

Yukihiro UTSUMI*1, Atsuhiro SHIRAKI*1, Sae HAMAMOTO*1, Junichiro KINUGASA*2

*1 Sheet Products Development Dept., Research & Development Lab., Iron & Steel Business
*2 Materials Research Laboratory, Technical Development Group

*Super-high strength steel sheets of a strength exceeding 980 MPa have been used in reinforcement parts for automotive bumpers and door to meet strengthened collision safety standards and to decrease weight for the sake of emission reduction. A study has been conducted to improve the bending workability, resistance weldability, and delayed-fracture immunity required for the steel sheets used in parts produced through cold forming, such as bumper reinforcements. The study then led to the development of martensitic steel sheets of 1300 MPa and 1500 MPa grades. The newly developed steel has enabled the production of bumpers of 1300 MPa grade and 1500 MPa grade, the world's highest grades for cold worked bumper reinforcements, while also enabling 10 to 15% less weight compared with conventional bumper reinforcements.*

## Introduction

There has been a growing need for steel sheets and members of ultrahigh strength in satisfying stronger collision safety standards and the need for less weight for emission reduction purpose. Steel sheets of the ultrahigh strength level of more than 980 MPa are currently used to make reinforcement parts for automotive bumpers and doors.

This paper describes the martensitic steel sheets of 1300 and 1500 MPa grade, which have mainly been adopted in the use of the above applications.

## 1. Concept of steel sheet design

Bumper reinforcements (hereinafter referred to as bumper R/F) represent the reinforcing parts attached to the front and rear of vehicles, which help absorb the impact in collisions. They typically have a hollow square cross section or B-shaped cross section as shown in **Fig. 1**. Steel sheet coils are cut to a specified length, pierced, roll formed or press formed, and then assembled into the final shape through seam welding or spot welding, etc.[1] In the case of roll forming, they are bent according to the shape of the front or rear side of the vehicle after the forming and seam welding processes. Steel sheets used in bumpers therefore require the following characteristics.

(1) Bending workability of the base material (roll formability)
(2) Resistance weldability (wide range of suitable current with seam welding and spot welding, strength of welded joints, and bending workability of seam welds)
(3) Delayed-fracture immunity (characteristics specifically required for high-strength steel)

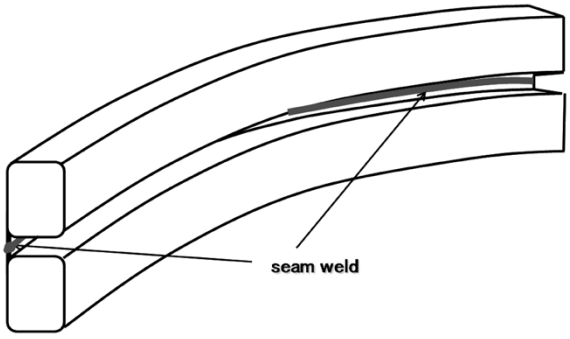


Fig. 1 Example of bumper reinforcements

### 1.1 Bending workability

In order to obtain excellent bending workability of the high strength of 1300 MPa and 1500 MPa grade martensitic steel, it is effective to form martensitic single phase structures, which provide uniformly high strength. However, martensitic structures as quenched can be brittle although of high strength, and therefore tempering is used to improve their ductility and toughness. Meanwhile, it is known that the bending workability is affected by the tempering temperature, and that it deteriorates in the tempering temperature range where so called low-temperature tempering embrittlement occurs.[2]

We therefore examined the effect of the tempering temperature on the tensile strength or bending workability (minimum bending radius) of 0.22% C martensitic steel sheets of 1.0 mm in thickness. **Fig. 2** shows the results. The results indicate that the same phenomenon occurs as described above, and that high strength and bending workability can be compatible in a tempering temperature range lower than that where the bending workability deteriorates.

### 1.2 Resistance weldability

High-tensile steel sheets have some problematic issues; that is, the suitable welding current range with spot welding (the current range after a specified nugget diameter is obtained until an expulsion,

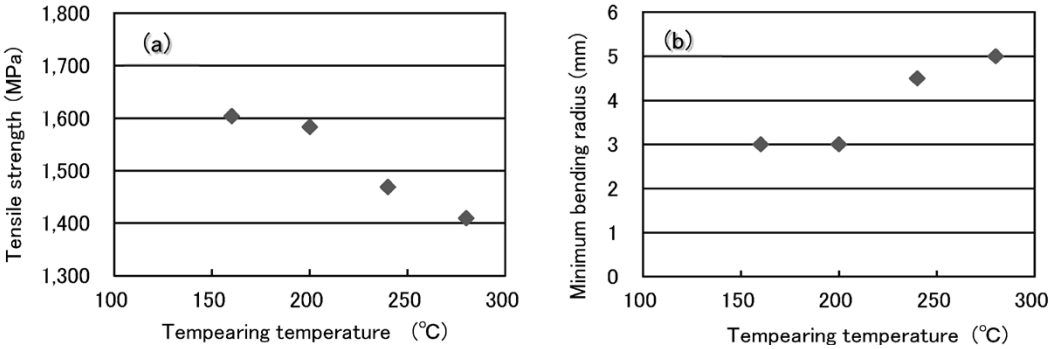


Fig. 2 Effect of tempering temperature on (a) tensile strength and (b) minimum bending radius

which is scattering of molten metal develops) decreases[3] and the cross tensile strength does not increase[4]. This phenomenon can also be observed in the same way with seam welding, which is another type of resistance welding. In order to expand the suitable welding current range, it is important to shift the expulsion development current to the high-current side, and it is effective to reduce the addition of the elements that increase the electric resistance of steel, including P, Si, Mn, etc.[5]

The characteristics required in bumper R/Fs, which have a closed cross section manufactured by roll forming, include peel strength and bending workability of seam welds. The relationship between peel strength and bending workability of seam welds and the additive elements was therefore examined. Laboratory-melted steel with the chemical composition shown in **Table 1** was hot rolled, pickled, cold-rolled, and then heat treated in a salt bath to manufacture martensitic steel sheets of 1.2 mm in thickness. The heat treatment included being held at 900℃ for 90 seconds to austenitize, and being water quenched and then tempered at 200℃ for 360 seconds. The resulting steel sheets were then seam welded with two sheets overlapped, and the peel strength of the seam weld was measured using the test shown in **Fig. 3**. In addition, a U-bend test of the seam weld was conducted at a right angle to the weld line using dies of 2 mm, 3 mm, 5 mm, and 10 mm in tip radius, as shown in **Fig. 4**, thereby determining the minimum bending radius where no cracks were caused in the weld. The correlation between these measurements and the chemical composition was then determined using multiple regression analysis. **Fig. 5** shows the results of measuring the peel strength of seam welds and **Fig. 6** the results of measuring the minimum bending radius of seam welds in a correlation of Ceq1 and Ceq2, as determined by multiple regression analysis, respectively.

The peel strength of seam welds has a correlation of Ceq1=C+Mn/5+Si/13, thus indicating that it improves as Ceq1decreases. Meanwhile,

Table 1 Chemical composition of steels

(mass%)

| C | Si | Mn | others |
|---|---|---|---|
| 0.12～0.26 | tr～1.4 | 0.5～2.1 | Ti,Nb,V,Cr,Mo,B,Cu,Ni |

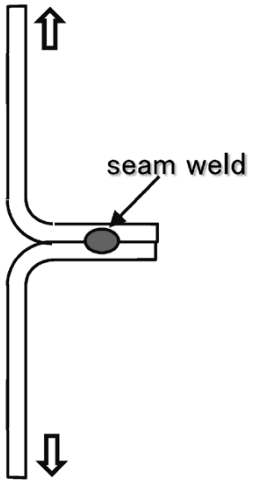


Fig. 3 Peel test of seam weld

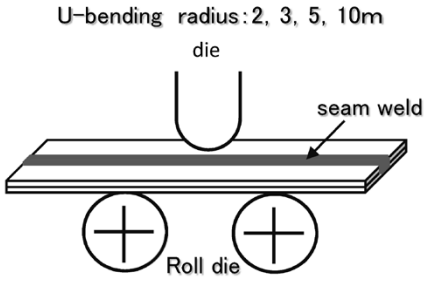


Fig. 4 Bending test of seam weld

the bendability of seam welds has a correlation of Ceq2=C+Mn/7.5, thus indicating that it improves as Ceq2 decreases.

### 1.3 Delayed-fracture immunity

It is well known that hydrogen embrittlement cracking tends to occur, i.e. the delayed fracture sensibility increases when the strength of steel is increased[6]. It is also agreed that the delayed-fracture immunity of steel sheets is affected not only by

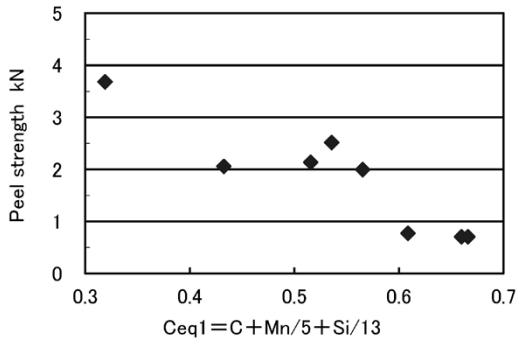


Fig. 5 Effect of chemical composition on peel strength of seam weld

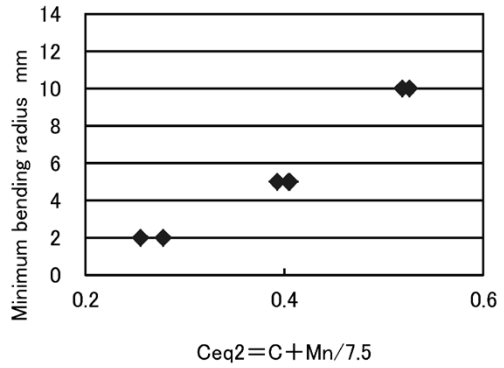


Fig. 6 Effect of chemical composition on minimum bending radius of seam weld

their strength but also their chemical composition, microstructure, etc. The delayed fracture of high-strength steel is a phenomenon wherein the hydrogen generated in connection with the corrosion reaction of the steel penetrates into it, and hydrogen embrittlement cracking of the steel occurs at a locally concentrated area in accordance with the tensile stress gradient. In other words, hydrogen embrittlement is understood to be a phenomenon caused by three different factors that are related to each other: (1) the penetrability of the hydrogen into the steel, (2) the diffusivity of the hydrogen in the steel, and (3) the hydrogen embrittlement sensibility of the structure of the steels.

Accordingly, effective measures to counteract each of the above factors involved in hydrogen embrittlement from the steel side to use include: (1) preventing the hydrogen from penetrating the steel by improving the corrosion resistance, (2) preventing the hydrogen from diffusing into the steel and concentrating in a tensile stress area by introducing trap sites, and (3) reducing the hydrogen embrittlement sensibility of steel itself through grain refining. The delayed-fracture immunity measures were used based on a laboratory examination conducted from the viewpoint as described above.

With martensitic structures it is known that not only the bendability but also the delayed-fracture immunity can be affected by the tempering temperature described above[7), 8)]. The results of the examination of this paper indicated that the delayed-fracture immunity also deteriorates within basically the same temperature range as the tempering temperature range in which the bending workability deteriorates, and that all the high strength, bending workability, and delayed-fracture immunity factors are compatible within a tempering temperature range lower than that temperature range.

Steel sheets typically get cut or pierced into a specified length or shape in being processed into a specific part. However, it is considered that delayed fractures tend to occur along the edge of such processed parts due to the very large plastic strain involved. This means that, of the three above described measures taken to counter delayed-fracture immunity, the measures to prevent the hydrogen from penetrating and diffusing into the steel are the most effective as the effect of the base metal structure control tends to be lost. Because of this an optimized composition design was adopted through selecting the applicable elements.

## 2. Characteristics of martensitic steel manufactured using an actual machine

The results of the laboratory examination were taken into account to manufacture 1300 MPa and 1500 MPa grade cold rolled steel sheets (thickness: 1.2 mm) using an actual machine. The qualities of appropriate bending workability, resistance weldability, and delayed-fracture immunity were taken into account in the design of the steel sheets, while also taking full advantage of the water quenching process that is a feature of Kobe Steel's continuous annealing line. **Fig. 7** shows a SEM image of the developed steel, and **Table 2** the mechanical properties. The bending workability included a 90° V-bend test and L-bend test (**Fig. 8**) in determining the minimum bending radius. **Table 3** shows the results. Both the 1300 and 1500 MPa grade steel sheets formed uniform martensitic single phase structures and featured favorable bending workability.

The spot weldability was evaluated through welding the test materials of 1.2 mm in thickness with a DR type electrode of 6 mm in tip diameter, a welding pressure of 4.1 kN, a welding time of 10 cycle/60 Hz, and welding current of 4 to 13 kA. **Fig. 9** shows the effect of the welding current on the tensile shear strength and cross tensile strength, respectively. **Table 4** shows the suitable welding current, and the nugget diameter, tensile shear strength, and cross tensile strength obtained within the range. The lower limit of the suitable welding

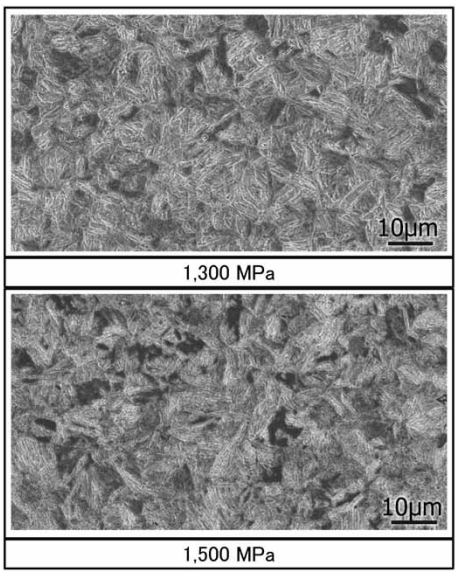


Fig. 7 SEM image of developed steels

Table 2 Typical mechanical properties of developed steels

| Developped steel | YS (MPa) | TS (MPa) | EL (%) |
|---|---|---|---|
| 1300 MPa | 1,180 | 1,370 | 7 |
| 1500 MPa | 1,280 | 1,570 | 6 |

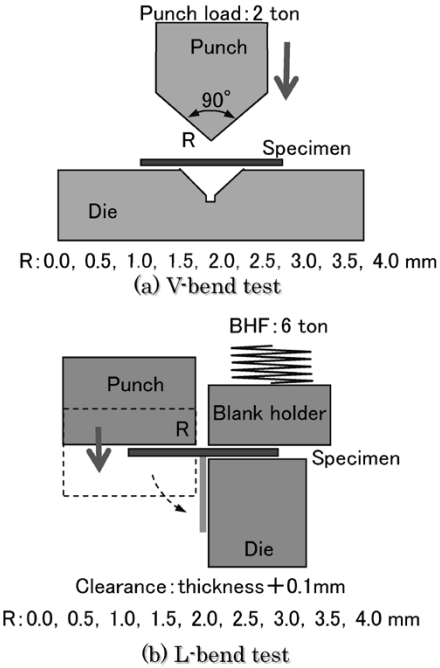


Fig. 8 Experimental procedure of (a) V-bend test and (b) L-bend test

Table 3 Typical bendability of developed steels

| Developped steel | 90°V bend test Minimum bend radius | | L bend test Minimum bend radius | |
|---|---|---|---|---|
| | Long. | Trans. | Long. | Trans. |
| 1300 MPa | 3.0 | 3.5 | 2.0 | 2.0 |
| 1500 MPa | 3.5 | 4.5 | 2.5 | 3.5 |
| DP980 MPa | 1.0 | 2.0 | 1.0 | 1.5 |

Rmin : Minimum bend radius
Thickness : 1.2 mm

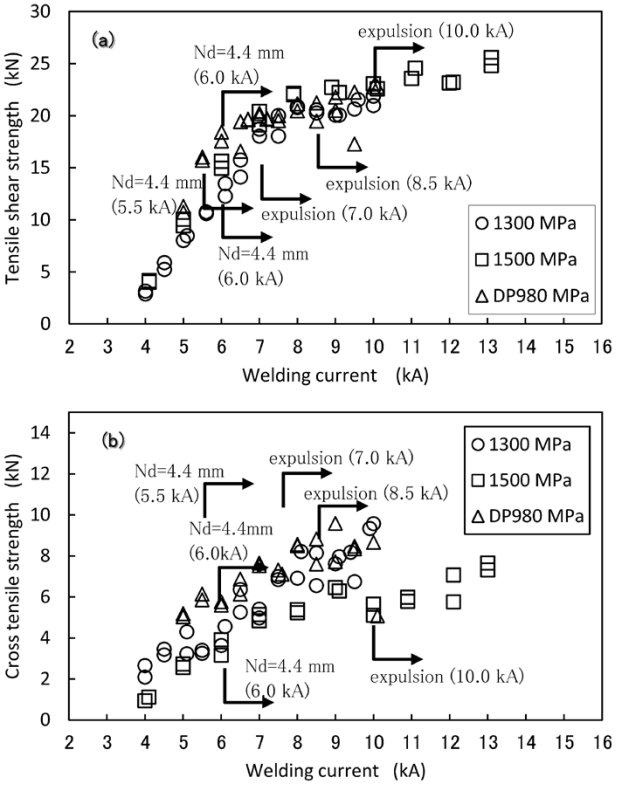


Fig. 9 Effect of welding current on (a) tensile shear strength and (b) cross tensile strength in developed steels

current range in this evaluation had the current value where the nugget diameter becomes equal to the minimum nugget diameter of 4.4 mm ($4\sqrt{t}$) in accordance with the requirements of JIS Z 3140, Class B. The list also includes results of evaluating high-ductility type DP steel sheets of 980 MPa grade.

The tensile shear strength of the 1300 and 1500 MPa grade steel sheets is almost the same as that of the 980 MPa grade steel sheets but the cross tensile strength tends to decrease in the order of the 980, 1300, and 1500 MPa grade steel sheets. The

Table 4 Suitable welding current for developed steels, and their nugget diameter, tensile shear strength and cross tensile strength

| Developped steel | Suitable welding current (kA) | Nugget diameter (mm) | Tensile shear strength ($\times 10^3$N) | Cross tensile strength ($\times 10^3$N) |
|---|---|---|---|---|
| 1300 MPa | 6.0～8.5 | 4.4($4\sqrt{t}$)～7.0 | 12.0～21.0 | 4.0～8.0 |
| 1500 MPa | 6.0～10.0 | 4.4($4\sqrt{t}$)～7.5 | 15.0～23.0 | 3.0～6.5 |
| DP980 MPa | 5.5～7.0 | 4.4($4\sqrt{t}$)～6.5 | 15.0～20.0 | 5.0～7.0 |

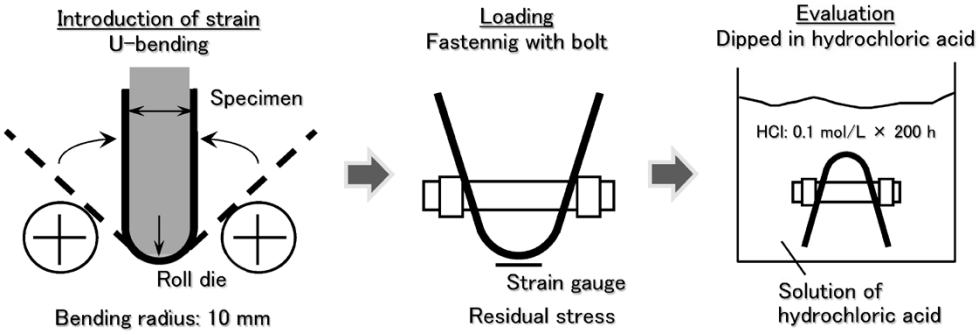


Fig.10 Experimental procedure of delayed-fracture immunity test

results agree with those of a study made by Oikawa, et al.[9], revealing that the tensile shear strength get saturated above 1,100 MPa and the cross tensile strength saturated around 590 to 780 MPa, with a decreasing tendency as the strength of the steel sheets increases in the case of the 780 MPa grade steel sheets.

The suitable welding current range is as wide as 2.5 kA for the 1300 MPa grade steel sheets and 4 kA for the 1500 MPa grade steel sheets, whereas it is 1.5 kA for the 980 MPa grade steel sheets. In addition, the nugget diameter obtained at the upper limit of the suitable welding current range is larger than that of the 980 MPa grade steel sheets. For this reason the cross tensile strength obtained at the upper limit of the suitable welding current range of the 1300 and 1500 MPa grade steel sheets is almost the same as that of the 980 MPa grade steel sheets. This then means that the practical weldability would appear to be almost the same as that of the 980 MPa grade steel sheets.

The delayed-fracture immunity was evaluated using a U-bend test (dipped in hydrochloric acid) as shown in **Fig.10**. To examine the crack initiation, strip test pieces were U-bent with a bend radius of 10 mm, and then dipped in 0.1 mol/L of hydrochloric acid for 200 hours, while loading stress of 1,300 MPa for the 1300 MPa grade steel sheets, and stress of 1,500 MPa for the 1500 MPa grade steel sheets. Note that strip test pieces are usually tested with their edges machined. However, some strip test pieces as shear cut and without their edges machined were also tested as generally steel sheet formed parts have cutting edges. The test results revealed that, both the 1300 and 1500 MPa grade steel sheets exhibited no cracks with both test pieces with the edge machined and as shear cut and without the edge machined, and thereby indicating that the delayed-fracture immunity is favorable.

The developed sheets make it possible to manufacture, by cold forming, bumpers from both 1300 and 1500 MPa grade steel sheets, the world's highest level of strength as a bumper R/F. Further more, they can be reduced by 10 to 15% of their weight when compared with conventional bumper R/F parts.

## Conclusions

Kobe Steel commercialized 1180 MPa grade cold rolled sheet steels, and has already produced and distributed them for use in bumper R/Fs. In response to the need for further higher levels of strength, this paper has introduced the newly developed 1300 and 1500 MPa grade martensitic steel sheets. The developed steel sheets have been adopted by some customers for use in making roll formed bumper R/Fs, and have started to be produced commercially.

A constantly important issue in the automobile industry is satisfying both better collision safety and less weight. The requirement with automotive body use is the application of 980MPa, 1180 MPa, and 1470 MPa grade steel sheets. The even high level of strength of up to 1,700 MPa is a challenge that will be addressed in the future.

Kobe Steel will continue to strive to develop materials that can contribute to the needs of even higher level of strength and better workability.

## References

1) M. Yamaguchi et al. "Life cycle inventory of aluminium and steel hood and bumper reinforcement for automobiles". *EcoBalance 2004, October 26*, 2004, Japan Aluminium Association, Aluminum and Environment, http://www.aluminum.or.jp/environment/index.html (accessed 2016-06-03).
2) Y. Nagataki et al. *Tetsu-to-Hagane*. 2013, Vol.99, No.3, p.71.
3) F. Tanaka et al. *Tetsu-to-Hagane*. 1982, Vol.68, No.9, p.1437.
4) M. Ono, *184th/185th Nishiyama Memorial Lecture*. p.139.
5) D. C. Ludwigson et al. *Metallurgical Transactions*, 1971, Vol.2, December, p.3500.
6) S. Matsuyama. *Delayed Fracture*. Nikkan Kogyo Shimbun, 1989.
7) S. Fukui. *Tetsu-to-Hagane*. 1969, Vol.55, No.2, p.151.
8) S. Matsuyama. *Tetsu-to-Hagane*. 1972, Vol.58, No.3, p.395.
9) H. Oikawa et al. *Nippon Steel Technical Reports*. 2006, No.385, p.36.

# Steel Sheets for Highly Productive Hot Stamping

Sae HAMAMOTO*1, Hiroyuki OMORI*1, Tatsuya ASAI*1, Naoki MIZUTA*2, Noriyuki JIMBO*2, Takayuki YAMANO*2

*1 Sheet Products Development Dept., Research & Development Lab., Iron & Steel Business
*2 Process Engineering Development Dept., Research & Development Lab., Iron & Steel Business

*Rapid progress is being made in the application of hot-stamped, super-high strength parts to automobile bodies. Hot stamping is a technology that can solve the problems associated with high-strength steel sheet, e.g., an increased forming load and deterioration of dimensional accuracy; however, the method has suffered from low press productivity and limitation in the shapes of parts. In order to overcome these issues, a steel sheet for hot stamping has been developed via compositional design. This paper introduces the characteristics of the newly developed steel sheet and its practical applications, including a demonstration of the multi-step hot stamping.*

## Introduction

High-strength steel sheets have increasingly been used for automotive structural members to comply with strengthened collision safety standards and to decrease the weight for emission reduction purposes. Kobe Steel has been providing various kinds of high-strength steel sheets for cold forming. Recently, it put 1180 MPa grade steel sheets into practical use, and they were adopted for automotive body structures for the first time in the world[1), 2)]. However, high-strength steel sheets for cold forming have an issue that the forming load is increased and the dimensional accuracy is reduced as the steel sheet strength is increased[3)]; accordingly, a limited amount of 1180 MPa grade steel sheets have been put into practical use.

To solve such the issue, the application of hot stamping has been expanded[4), 5)]. Hot stamping is a process in which steel sheets are heated up to an austenite range, hot formed, and then die-quenched to form martensite structures, which can easily increase the strength up to 1500 MPa grade. In general, steel sheets for hot stamping use 22MnB5 steel (boron steel); however, it takes time to quench it to ensure the strength, and the productivity rate is about one tenth of that of steel sheets for cold forming[6)]. Accordingly, improvements in hot stamping productivity by means of compositional design[6), 7)] or improved die quenching method[8)] have been proposed.

Focusing on the issue of steel sheets for hot stamping as described above, Kobe Steel developed a steel sheet for high productivity hot stamping by means of optimized compositional design, which is introduced in this paper.

## 1. Concept of compositional design of developed steel

In a hot stamping process using 22MnB5 steel, steel sheets are austenitized, die quenched, and then die opened after holding until they are cooled to 200℃ or less to form the martensite structure required for achieving a strength of 1,500 MPa, as shown in **Fig. 1**.[9)] For example, if the required strength can be achieved with die opening at 600℃, the holding time for die quenching could be significantly shortened to about 3 seconds, while the conventional holding time is about 15 seconds, allowing press productivity to be improved. In conventional hot stamping, the strength to be obtained after die opening is 1,500 MPa; therefore, the subsequent piercing and trimming require laser processing for reasons of die durability and delayed fracture in a cutting area, causing an increased cost due to decreased productivity and additional investment in equipment.

Meanwhile, if the holding time for die quenching can be shortened, the steel sheet temperature after forming would still be high, and a low-strength state could be maintained. Then, multi-step hot stamping becomes possible, where piercing and trimming are performed in one press machine continuously after forming. This is expected to improve significantly the productivity of hot stamped parts.

Then, cold rolled steel sheets (thickness: 1.4 mm) with chemical compositions shown in **Table 1** were

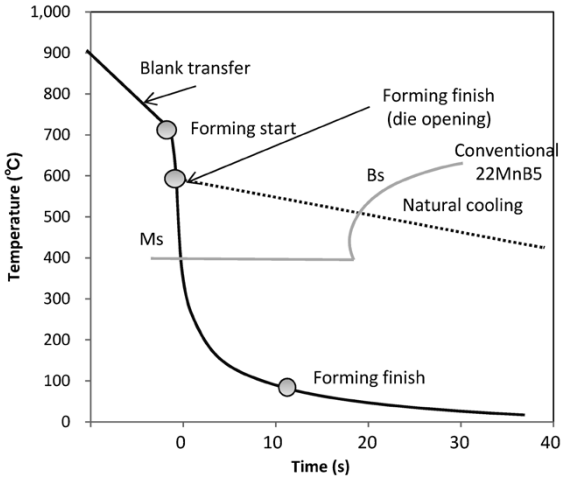


Fig. 1 Steel temperature change in conventional hot stamping

Table 1 Chemical composition of steels

(mass%)

| | C | Si | Mn | Cr | Ti | B |
|---|---|---|---|---|---|---|
| Conventional 22MnB5 | 0.23 | 0.02 | 1.3 | 0.2 | 0.02 | 0.0029 |
| Hi-Mn | 0.23 | 0.20 | 2.1 | – | 0.02 | 0.0015 |
| Hi-Si | 0.22 | 1.19 | 1.3 | 0.2 | 0.03 | 0.0025 |
| Developed steel | 0.22 | 1.20 | 2.2 | – | 0.02 | 0.0015 |

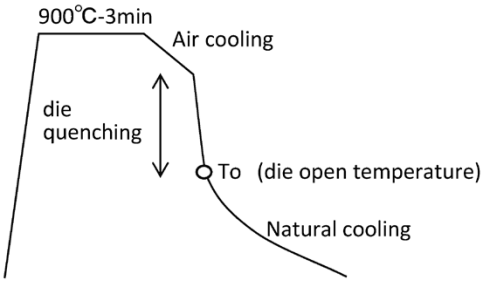


Fig. 2 Experimental method

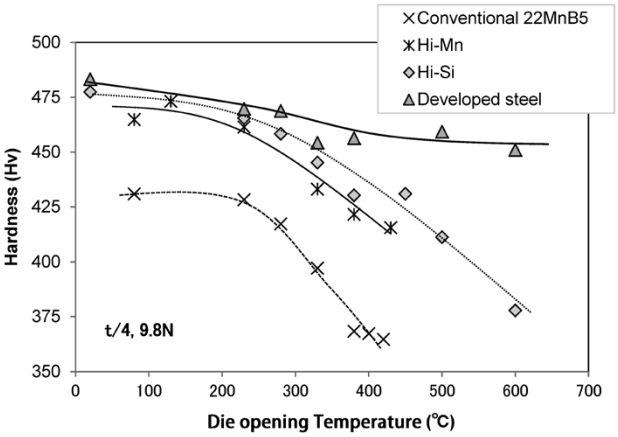


Fig. 3 Effect of die opening temperature on hardness

heat treated as shown in **Fig. 2**, and examined for the effect of die opening temperature (To) on hardness. **Fig. 3** shows the results. In this development, we focused on the addition of Mn and Si in order to inhibit the ferrite and bainite transformation. Si is also capable of increasing the temper softening resistance of martensite.

Hi-Mn steel with increased Mn, compared with 22MnB5 steel, is capable of increasing hardness at any die opening temperature. However, in order to obtain a reliable hardness of 450 HV or more, which is equivalent to a strength of 1,500 MPa, it is necessary to cool down to 200℃ or less. Hi-Si steel with increased Si gives the same results as Hi-Mn steel. By contrast, the developed steel sheet with increased Si and Mn shows excellent hardenability, with a hardness of 450 HV or more being obtained even at a die opening temperature of 600℃, with a small change in hardness depending on the die opening temperature. Thus, the developed steel sheet, which can ensure hardness without

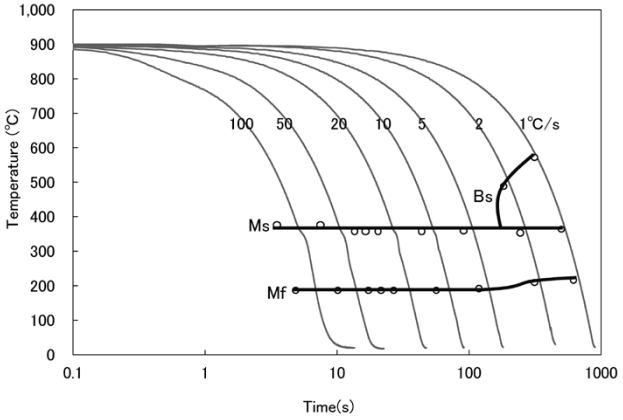


Fig. 4 CCT diagram of the developed steel

die quenching, allows the holding time for die quenching to be significantly shortened, and further processing to be added within one press machine.

**Fig. 4** shows the CCT diagram of the developed steel sheet. With the developed steel sheet, the ferrite and bainite transformation is inhibited by the addition effect of Mn and Si, and the critical cooling rate is about 5℃/s, while it is about 30℃/s in the case of conventional 22MnB5 steel.

In order to achieve a stable hardness in stamped parts, the dependency of the cooling rate below the Ms point (the secondary cooling rate) should be low. Accordingly, the effect of the secondary cooling rate on hardness was examined, using test material manufactured from a cold rolled steel sheet, which was heated up to 900℃, quenched to 380℃, and then cooled at different secondary cooling rates ($CR_2$) as shown in **Fig. 5**. **Fig. 6** shows the results. While hardness is significantly decreased by the effect of the secondary cooling rate in the case of 22MnB5 steel, the cooling rate dependency is small, and the hardness is stable in the case of the developed steel. This seems to be due to the fact that in the case of the developed steel the temper softening resistance is increased by the addition of Si and the hardness is stable, while in the case of 22MnB5 steel the self-tempering of martensite progresses as the cooling rate is decreased.

With the developed steel, strength can be ensured by adding Mn and Si appropriately under a wide range of cooling conditions after heating, and a stable hardness can be obtained in a practical cooling rate range (5℃/s or more) below 380℃.

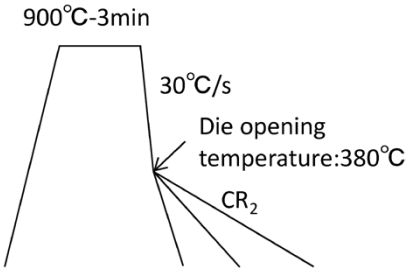


Fig. 5 Experimental method

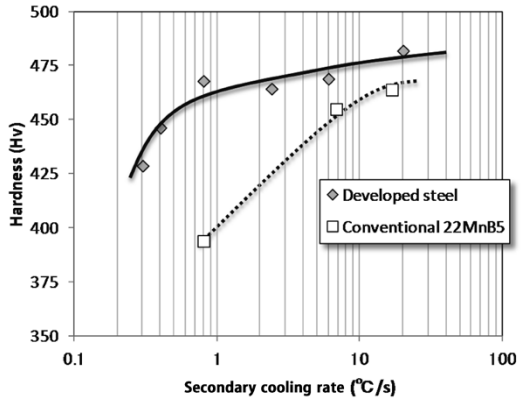


Fig. 6 Effect of secondary cooling rate on hardness

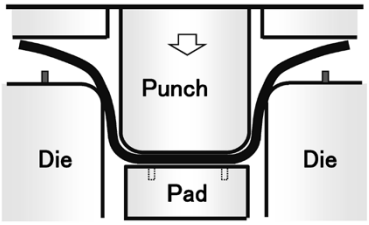


(a) Test forming tools

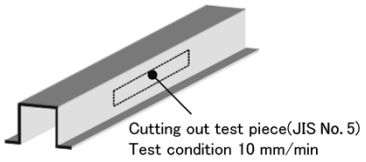


(b) Position of collecting test specimen

Fig. 7 Experimental methods for die pressing

Table 2 Effect of holding time for die quenching on mechanical properties

| | Holding time at die quenching (s) | Die opening temperature (℃) | YS (MPa) | TS (MPa) | EL (%) |
|---|---|---|---|---|---|
| Developed steel | 0 | about 600 | 1,056 | 1,504 | 10 |
| Conventional 22MnB5 | 15 | about 200 | 1,149 | 1,512 | 8 |
| | 0 | about 600 | 1,028 | 1,080 | 6 |

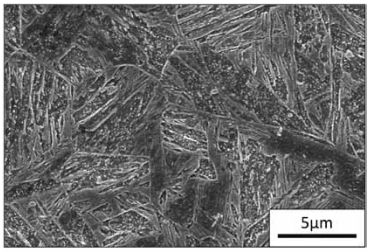


(a) Conventional 22MnB5
(holding time at Die quenching: 15 s)

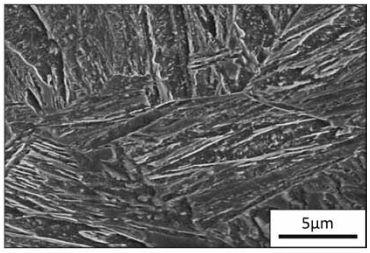


(b) Developed Steel
(holding time at die quenching: 0 s

Fig. 8 Microstructure of die quenched steel

## 2. Characteristics of developed steel sheet

### 2.1 Basic characteristics after hot stamping

We manufactured the JIS No. 5 test pieces from a cold rolled steel sheet of 1.4 mm in thickness, by heating it up to 900℃, forming it into the shape shown in **Fig. 7** (b) using the die shown in (a), and then cutting out the test piece from the position shown in (b). The holding time for die quenching was set to 2 levels: 0 second (without holding) and 15 seconds. The tensile test results using these test pieces are shown in **Table 2**. While 22MnB5 steel showed a strength of 1,500 MPa or more with a holding time for die quenching after hot stamping of 15 seconds, the developed steel showed a strength of 1,500 MPa or more even without holding time for die quenching.

**Fig. 8** shows the microstructures of 22MnB5 steel with holding time for die quenching for 15 seconds, and the developed steel without holding time for die quenching. Both steels have single phase structures of martensite; however, the developed steel produces less carbide compared to 22MnB5 steel. This seems to be due to the effect of Si inhibiting carbide. It presumably contributes to an increase in temper softening resistance, and makes it possible to obtain high-strength without holding time for die quenching.

### 2.2 Practical characteristics

In order to evaluate spot weldability, chemical conversion treatability and low-temperature toughness, we heated the developed cold rolled steel sheet of 1.4 mm in thickness (t) up to 900℃, forcibly cooled it to 380℃, and then cooled it naturally. We prepared the test material by removing the surface scale by shot blasting using iron balls of 0.3 mm in diameter at an air pressure of 0.4 to 0.5 MPa. It

has been proven that the tensile strength (TS) is of 1500 MPa grade.

We spot welded the test material in the conditions shown in **Table 3** to examine the effect of the current on the nugget diameter. **Fig. 9** shows the results. The welding current stands at 6.0 kA when the nugget diameter is $4\sqrt{t}$, and the welding current stands at 8.0 kA when expulsion is developed. This means that a suitable welding current range exists around 2.0 kA, which is comparable with that of conventional 22MnB5 steel and other high-tensile steels. **Fig.10** shows the effect of the welding current on cross tension strength. A stable cross tension strength of 7,000 N or more was obtained within the suitable welding current range, which is comparable with that of conventional 22MnB5 steel.

Chemical conversion treatability was evaluated using a commercial treatment solution (Surfdyne SD 6350 from Nippon Paint). **Fig.11** shows the phosphate film on the surface of the developed steel sheets. No lack of hiding (exposure of substrate) is observed, and the crystal grain size and form are also favorable.

Table 3 Spot welding conditions

| | |
|---|---|
| Elctrode tip | Dome type Cu-Cr, tip diameter: 6 mm |
| Elctrode force | 4,000 N |
| Welding time | 20 cycles (60Hz) |

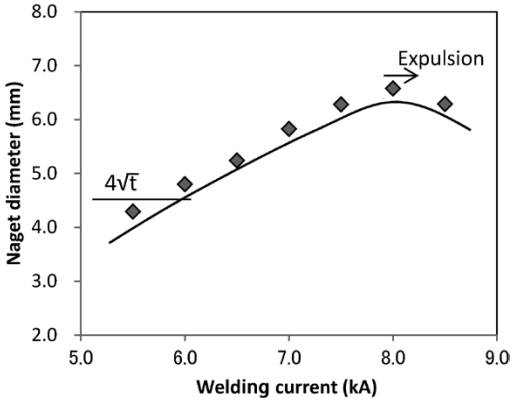


Fig. 9 Relationship between spot welding current and nugget diameter

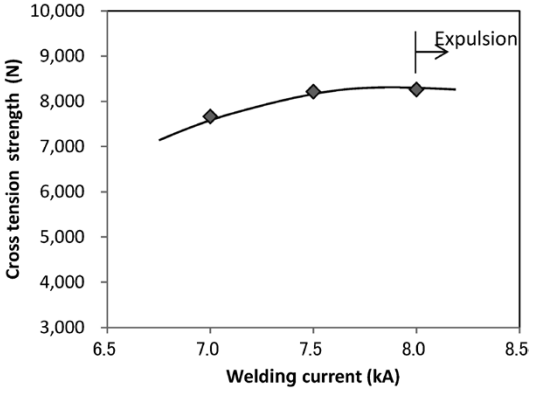


Fig.10 Relationship between spot welding current and cross tension strength

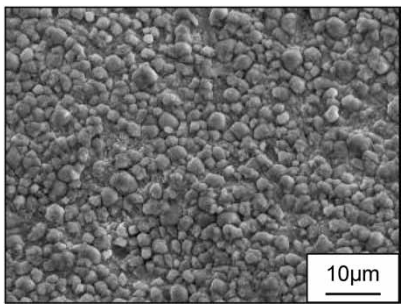


Fig.11 Micrograph of phosphate crystal on developed steel

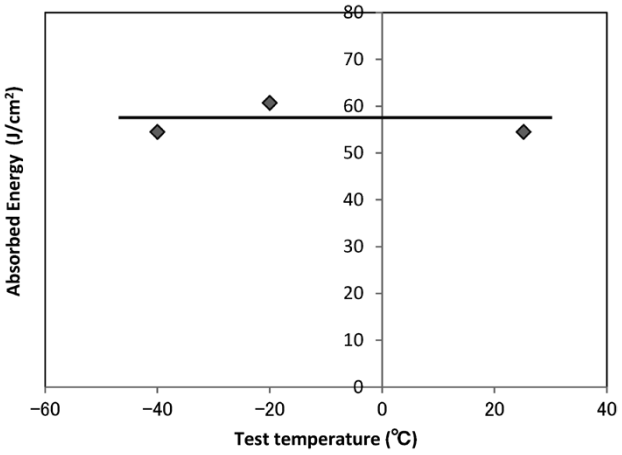


Fig.12 Results of Charpy test of developed steel

**Fig.12** shows the evaluation results on the JIS No. 4 Charpy test pieces manufactured. No brittle fracture surface is observed at any test temperature, and a comparable absorbed energy is shown at -40℃ and room temperature; accordingly, the practical characteristics of the low-temperature toughness are satisfied.

## 3. Evaluation of usefulness of developed steel sheet

### 3.1 Verification of multi-step hot stamping

It was expected that the excellent hardenability and hardness stability of the developed steel would also be effective in hot stamping where the contact with the die tends to be insufficient[10], including multi-step hot stamping and different-thickness welded parts in tailored blanks.

Accordingly, we conducted a verification experiment for multi-step hot stamping. In this verification, multiple die sets were manufactured to form into the part shape as shown in **Fig.13** - Stage #3 in 3 steps, which seems to be difficult to form in the conventional single step. Piercing and trimming were included in Stage #2 and Stage #3,

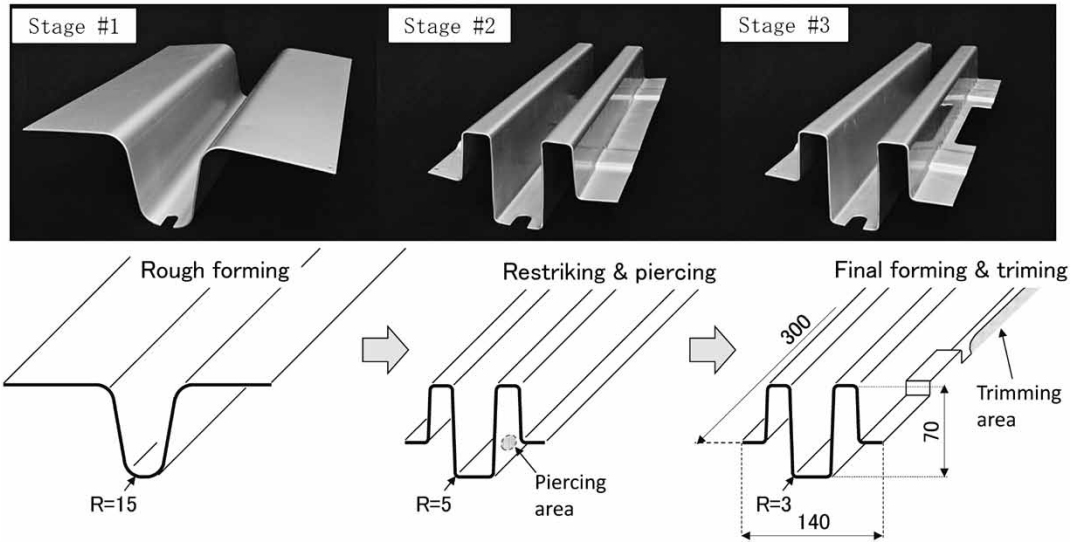


Fig.13 Changes in shape of member in multi-step hot stamping

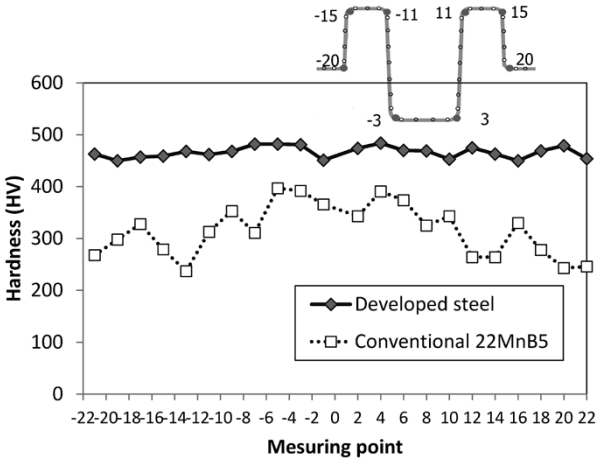


Fig.14 Hardness distributions of specimens

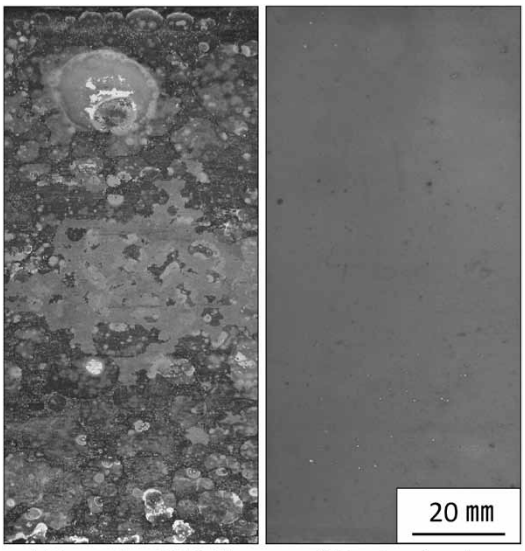


Fig.15 Sheet surface after die quenching

respectively. These die sets were mounted to a crank press machine. A blank of developed steel (1.4 mm in thickness) was heated to 900℃, and then transferred to the die in Stage #1. It was conveyed among the die sets using a robot, while the cycle time of the crank press machine was set to 20 shots per minute. The die opening temperature in Stage #3 was about 300℃, and the dimensional accuracy was favorable.

**Fig.14** shows the hardness distribution measured at various points on the parts obtained. The 22MnB5 steel formed in the same process as above did not satisfy the hardness of 450 HV at any measuring point, with a large variation in hardness within the part. Meanwhile, the developed steel showed a stable hardness of 450 HV or more throughout the part. This indicates that the developed steel sheet makes possible such multi-step hot stamping, and that not only complicated shapes but also piercing and trimming can be processed in a single press machine.

### 3.2 Surface characteristics of developed steel

Cold rolled steel sheets of 22MnB5 steel and the development steel were heated to 900℃ in an atmospheric furnace, air cooled, and then die quenched from 700℃ to room temperature. **Fig.15** shows the appearance of the surface of each steel sheet. While a large amount of scale is peeled off in the case of 22MnB5 steel, the developed steel is excellent in scale adhesion, which shows almost no peeling off. It is known that Si increases the high-temperature oxidation resistance of steel[11], and inhibits the production of oxidized scale. The developed steel sheet seems to have increased the adhesion, because scale was thinned by adding Si by 1.0% or more.

Such characteristics of the developed steel sheets are expected to prevent scale from peeling off in

the die in an actual press, and prevent any surface defects in stamped parts caused by scale inclusion.

## Conclusions

Kobe steel has developed a new steel sheet for highly productive hot stamping, and this paper has introduced its main characteristics. The developed steel sheet shows not only high productivity but also excellent hardness stability. In addition, it has also characteristics that satisfy customers' requirements, in terms of spot weldability, chemical conversion treatability and low-temperature toughness; therefore, it is expected to be used for multi-step hot stamping. Furthermore, it contributes to stabilizing the hot stamping process, because its excellent scale adhesion prevents scale from peeling off in the die.

Kobe Steel will continue striving to develop the steel sheets that satisfy its customers and contributes to expanding the application of high-strength steel sheets.

## References


1) T. Murata et al. *R&D Kobe Steel Engineering Reports*. 2016, Vol.66, No.2, pp.17-20.
2) E. Fukuhara et al. *Nissan Technical Review*. 2015, No.76, p.5.
3) A. Sato. *Journal of Japan Society for Technology of Plasticity*. 2005, Vol.46, No.534, p.548.
4) K. Nakajima. *CAMP-ISIJ*. 2004, Vol.17, p.980.
5) H. Kojima. *Press Working*. 2004, Vol.42, No.8, p.38.
6) T. Senuma et al. *Journal of Japan Society for Technology of Plasticity*. 2008, Vol.49, No.567, p.567.
7) T. Senuma et al., *Journal of Japan Society for Technology of Plasticity*. 2010, Vol.51, No.594, p.54.
8) K. Mori et al. *Spring Conference for the Technology of Plasticity*. 2015, p.247.
9) D. W. Fan et al. *MS&T*. 2007, p.98.
10) K. Aida. *Press Working*. 2014, Vol.52, No.8, p.34.
11) S. Morioka. *Iron & Steel Corrosion Science*. Asakura Publishing, 1972, pp.58-60.

# Characteristics of 1180MPa Grade Cold-rolled Steel Sheets with Excellent Formability

Tadao MURATA*1, Sae HAMAMOTO*1, Yukihiro UTSUMI*1, Takayuki YAMANO*2, Dr. Yuichi FUTAMURA*3, Takayuki KIMURA*4

*1 Sheet Products Development Dept., Research & Development Lab., Iron & Steel Business
*2 Process Engineering Development Dept., Research & Development Lab., Iron & Steel Business
*3 Sheet Products Marketing & Technical Service Dept., Iron & Steel Business
*4 Mechanical Engineering Research Lab., Technical Development Group

*High-strength steel sheets are being used in recent years to improve crashworthiness and to decrease weight in order to reduce automobile emissions. Higher strength is desired particularly for automotive body frame members. In response to this demand, Kobe Steel has developed a 1180 MPa grade cold-rolled steel sheet with excellent formability. This paper introduces the guidelines for the microstructural control and typical characteristics of the steel sheet. The newly developed steel exhibits favorable practical characteristics of delayed-fracture resistance, spot weldability and conversion treatability, in addition to excellent strength and formability.*

## Introduction

High-strength steel sheets are being used in recent years to improve crashworthiness and to decrease weight in order to reduce automobile emissions.[1), 2)] Against this backdrop, Kobe Steel has been offering cold-rolled/galvanized steel sheets with their processabilities optimized for the shapes of parts,[3)-6)] and these sheets have been highly valued by customers.

Meanwhile, in the case of automotive body frame members, even higher strength is being pursued to protect passengers against collision. For example, a formability equivalent to that of low strength steel sheet is required for application to the complex shape parts typified by B-pillars. The formability of steel sheets, however, tends to decline with increasing strength in general, making it difficult to apply high-strength steel sheets of 1180 MPa grade or higher to complex shape parts.

To solve this problem, Kobe Steel conducted a study on high-strength steel sheets with excellent elongation (hereinafter referred to as "EL") and developed an 1180 MPa grade high-strength steel sheet with excellent formability to be used in automotive body frames. This was a world first.[7)] The steel sheet has an excellent EL approximately twice that of a conventional dual phase (DP) steel sheet. This paper introduces the concept of microstructure control for the newly developed steel and its main characteristics.

## 1. Concept of microstructure control for newly developed steel

The newly developed steel is used in high-strength sheets intended for application to complex shape parts and combines strength and excellent press formability. To suppress cracks during press forming, the hole expansion ratio ( $\lambda$ ), an index of stretch-flangeability, is an important factor in addition to EL. It is generally difficult, however, to achieve both EL and $\lambda$ together.

For the improvement of formability, it is known to be effective to add alloying elements such as C and Si. On the other hand, the addition of these alloying elements deteriorates the joint strength of spot welding[8)] and chemical conversion treatability,[9)] both being important practical properties of auto parts. In addition, the sensitivity to delayed fracture is increased in the case of high-strength steel sheet.[10)] Hence, it is also important to secure resistance against delayed fracture. To this end, various microstructure control measures have been developed to realize a steel sheet combining high strength, excellent formability and other practical properties.

**Fig. 1** shows the mechanical properties of typical high-strength steel sheets of Kobe Steel. The company has established the production technology of high-strength steel sheets for cold working, including DP steel sheets,[2), 4), 11)] TRIP-aided bainitic ferrite (TBF) steel sheets[12)-14)] and martensite steel sheets.[15)] The newly developed steel exploits

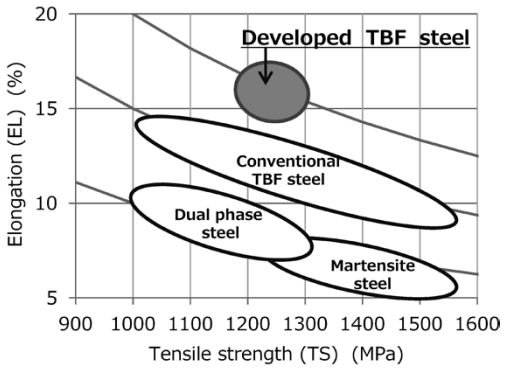


Fig. 1 Tensile strength and elongation of cold rolled steel sheets

the microstructure control technology for the conventional steel and, at the same time, applies the following microstructure control based on a further study on measures for improving the mechanical properties:

1) increasing the volume fraction of retained austenite by adjusting the additive amounts of the alloying elements (C and Si) and utilizing bainite transformation;
2) introducing martensite and refining retained austenite utilizing the transformation into martensite; and
3) introducing ferrite to provide a composite structure of soft and hard phases.

Examples of the microstructures of the newly developed steel and conventional TBF steel sheet are shown in **Fig. 2**. The newly developed steel includes ferrite existing in the matrix, which consists of bainite and martensite, and contains finely dispersed retained austenite. The newly developed steel has an excellent uniform deformability, thanks to the transformation induced plasticity (hereinafter referred to as "TRIP")[16] of retained austenite and the introduction of soft ferrite phase. In addition, the matrix consisting of bainite and martensite realizes high strength. Furthermore, the finely dispersed retained austenite reduces the void formation at the hard/soft interface between a very hard martensite, formed by the transformation of the retained austenite during deformation, and a soft phase,[12] suppressing the deterioration of the local deformability represented by the hole expansion ratio $\lambda$.

The typical mechanical properties of the newly developed steel are compared with those of the DP steel sheets (980 MPa grade and 1180 MPa grade) in

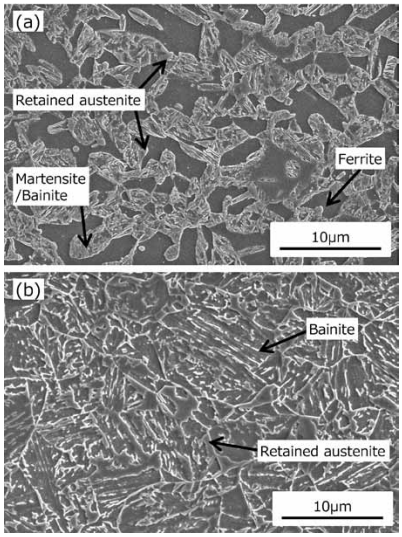


Fig. 2 Microstructure of (a) developed TBF steel, (b) conventional TBF steel

Table 1 Mechanical properties of developed TBF steel and dual phase steels

| Steel | Grade | YP (MPa) | TS (MPa) | EL (%) | λ-value (%) |
|---|---|---|---|---|---|
| Developed TBF steel | 1180MPa | 946 | 1,222 | 18 | 40 |
| Dual Phase steel | 1180MPa | 910 | 1,185 | 10 | 51 |
| Dual Phase steel | 980MPa | 640 | 1,020 | 17 | 25 |

※Specimen Thickness : 1.4mm
※Tensile Test : JIS Z 2241 (JIS Z 2201 #5 Specimen in Transverse directions)
※Stretch flanging (Hole expanding) test
Hole expanding ratio : λ-value obtained by method of JIS Z 2256

**Table 1**. The newly developed steel has very well balanced properties of TS, EL and $\lambda$, thanks to the improved uniform deformability and the suppressed deterioration of local deformability.

## 2. Main properties of newly developed steel

### 2.1 Formability

The press forming of thin steel sheets is roughly classified into 4 modes, namely, stretch flanging, bending, stretching and deep drawing. The $\lambda$ value, which is the index of stretch-flangeability, is as described above. The following describes the results of a study on the bendability, stretchability and deep drawability of the newly developed steel.

**Fig. 3** shows the typical properties of the minimum bending radius (R) of the 90° V-bending test conducted on the newly developed steel sheet, 980 MPa grade steel sheet and 1180 MPa grade DP steel sheet. In the bending test, a specimen (100 × 40 mm) was placed on a die such that the bending direction was vertical to the rolling direction, and a 90° punch with a tip radius (R) of 0 to 5.0 mm was pressed on the specimen. The minimum bending radius for no crack occurrence was taken as the index. Due to its high strength, the developed steel exhibits a bendability lower than that of the 980 MPa grade DP steel sheet; however, its bendability is equivalent to that of the 1180 MPa grade DP steel sheet. The finely dispersed retained austenite is considered to have suppressed the local concentration of strain, inhibiting the occurrence of voids, the origin points of cracks.

**Fig. 4** shows the typical stretch formability of

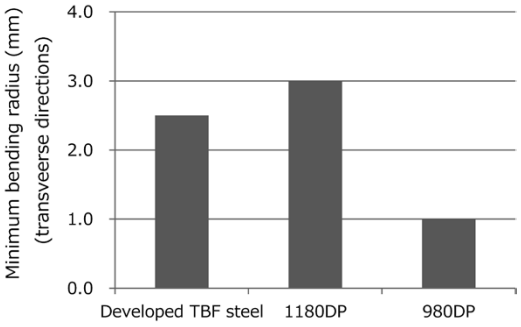


Fig. 3 Bendability of developed TBF steel and dual phase steels

the newly developed steel sheet, 980 MPa grade DP steel sheet and 1180 MPa grade DP steel sheet. The specimens were held with a blank holder force of 196 kN and formed with the die into the blank shape shown in **Fig. 5**. The stretch formability was evaluated by the maximum forming height of the stretch deformation with suppressed blank influx from the flange. The newly developed steel exhibits a maximum forming height equivalent to that of 980 MPa grade DP steel sheet, which is an effect of the improved EL achieved by the microstructure control described above.

**Fig. 6** shows the typical properties of deep drawability for the newly developed steel sheet, 980 MPa grade DP steel sheet and 1180 MPa grade DP steel sheet. The specimens were held with a blank holder force of 196kN and formed with the die into the blank shape shown in **Fig. 7**. The deep drawability was evaluated by the maximum forming height of deep drawing deformation accompanying blank influx from the flange. The newly developed steel shows a maximum forming height superior to that of the 980 MPa grade DP steel sheet. This is considered to be attributable to the excellent deep drawability achieved by the strain-induced transformation of retained austenite.

**Fig. 8** shows a forming limit diagram (FLD), comparing the newly developed steel with 980 MPa grade DP steel sheet having a thickness of 1.4 mm. The newly developed steel shows a forming limit equivalent to that of the low strength 980 MPa grade DP steel sheet, demonstrating its excellent press formability.

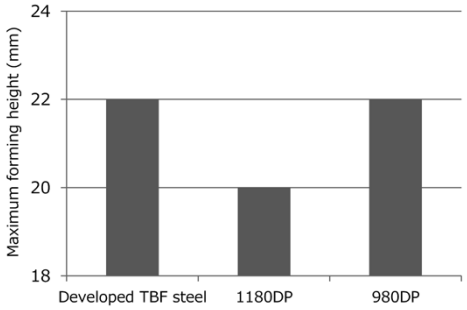


Fig. 4 Stretch formability of developed TBF steel and dual phase steels

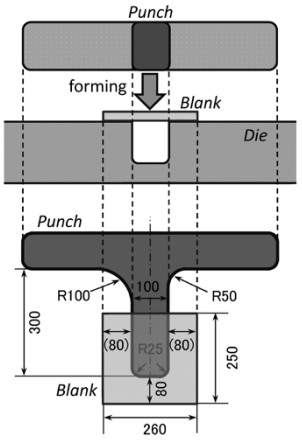


Fig. 5 Schematic illustration of measurement apparatus for stretch formability

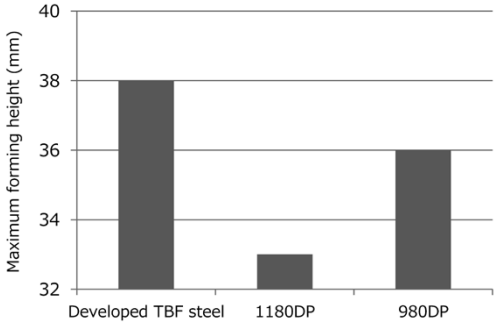


Fig. 6 Deep drawing formability of developed TBF steel and dual phase steels

## 2.2 Delayed-fracture resistance

The delayed-fracture resistance was evaluated by the occurrence of cracks on the specimens, stressed by U bending and bolt tightening and immersed in hydrochloric acid (**Fig. 9**). The results are shown

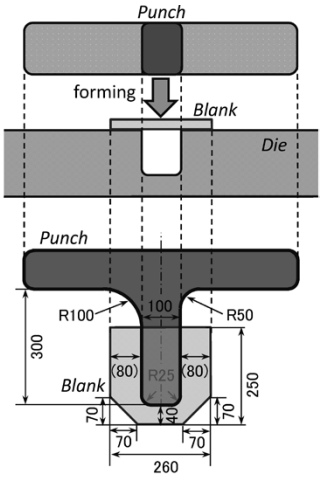


Fig. 7 Schematic illustration of measurement apparatus for deep drawing formability

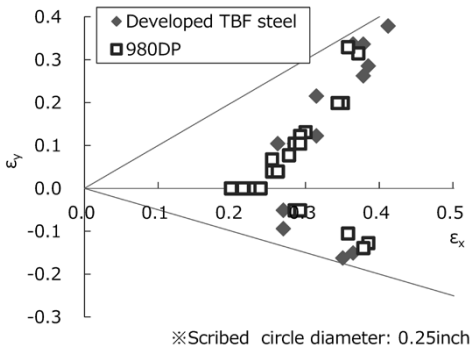


Fig. 8 Forming limit diagram of developed TBF steel and dual phase steel

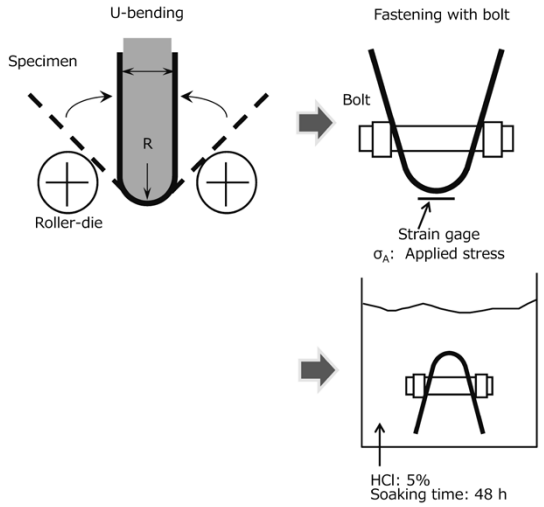


Fig. 9 Test procedure of delayed fracture resistance

Table 2 Delayed fracture properties of newly developed steel

| Steel | Applied stress (MPa) | Bending radius | |
|---|---|---|---|
| | | 5 mm | 10 mm |
| Developed TBF steel | 1,000 | ○ | ○ |
| | 1,500 | ○ | ○ |
| | 2,000 | ○ | ○ |

○:No fracture、×:Fracture

in **Table 2**. In the newly developed steel, no crack occurred even in the most severe test condition and exhibited excellent delayed fracture resistance. The retained austenite, finely dispersed in the newly developed steel, is considered to have occluded hydrogen, suppressing the crack generation due to hydrogen.[17)]

### 2.3 Spot weldability

In general, the steel sheets utilizing retained austenite require higher compositions compared with DP steel sheets, making welding nuggets harder and an interfacial fracture more likely to occur. This tendency is more remarkable especially when the nugget diameter is small, which decreases the weld joint strength. Although high electric current is effective in increasing the nugget diameter, expulsion (i.e., scattering of molten metal) becomes inevitable in the case of high composition steel, making it difficult to secure a proper current range to yield stable and favorable weld joint strength. The newly developed steel has been designed to have as low a composition, as possible, to secure weldability. In addition, a further study was conducted on the welding conditions for suppressing expulsion. In this study, a low current is energized in the first stage of two stage energization to mitigate the volume expansion of molten metal associated with the rapid rise in temperature that occurs upon the energization of high current and thus to suppress the expulsion.

As for the weld joint strength, steel sheets having a thickness of 1.2 mm were welded to evaluate tensile shear strength (TSS) and cross tensile strength (CTS). **Fig.10** shows the relationship between the welding current and TSS, while **Fig.11** shows the relationship between the welding current and CTS. In the case of the newly developed steel, the TSS satisfies the specified load of 8.78kN (JIS Z 3140 A-class) at the welding current of 5.0 kA or higher, enabling a wide appropriate range of 3.5 kA or higher to be secured for the current up to expulsion. In the cross tensile test, it was difficult to secure sufficient joint strength due to the small nugget diameter resulting from the low current condition, which caused interfacial fracture. On the other hand, increasing the welding current to expand the nugget diameter improved the fracture mode to a plug shape, which resulted in a favorable CTS. It was also possible to secure an appropriate current range of 1.5 kA or higher, indicating that a favorable welded joint can stably be formed.

### 2.4 Chemical conversion treatability

**Fig.12** shows an example of chemical conversion treatability; phosphate coatings on the surfaces of the newly developed steel and mild steel sheet.

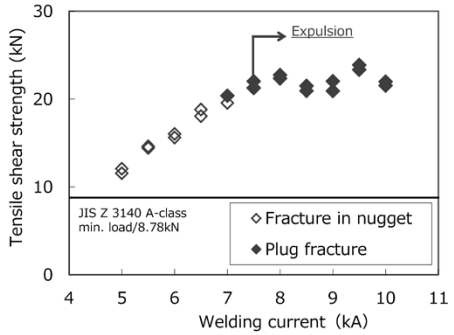


Fig.10 Relationship between tensile shear strength of spot welded joints and welding current

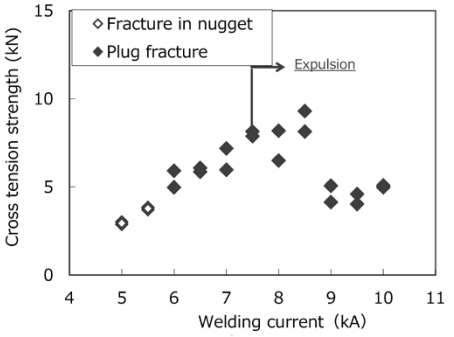


Fig.11 Relationship between cross tension strength of spot welded joints and welding current

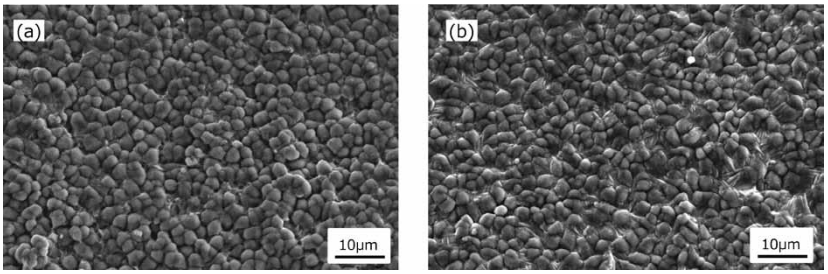


Fig.12 SEM image of phosphate coating on a) developed TBF steel, b) conventional mild steel

These coatings were formed by immersing respective sample steel sheets into a phosphate-treating agent, PALBOND-L3065, manufactured by Nihon Parkerizing Co., Ltd. Although the chemical conversion treatability generally declines as the amount of added Si increases, the newly developed steel exhibits no lack of hiding (poor formation of phosphate crystals). The grain size and forms of crystals are equivalent to those of mild steel, indicating favorable chemical conversion treatability. This is the result of applying the improvement of the practical characteristics and the improvement of the production technologies of high-Si steel sheets, accumulated through Kobe Steel's research over many years.[18)]

## Conclusions

This paper has introduced the concept of microstructure control and the main characteristics of the newly developed 1180 MPa grade cold-rolled steel sheet with excellent formability. The newly developed steel not only has favorable strength and formability but also exhibits excellent delayed fracture resistance and chemical conversion treatability, enabling the stable formation of spot welds having sufficient joint strength.

Kobe Steel positions the newly developed steel as a high formability product in its cold-rolled high-strength steel sheet menu. In addition to the high- $\lambda$ -type TBF steel sheet, the company also has a lineup including ultra-high-strength martensite steel.

Meanwhile, high-strength steel sheets will continue to be applied to automotive frames, and customers' needs for the material properties are expected to become even more stringent. Against this backdrop, Kobe Steel will strive to contribute to body weight reduction and collision safety improvement by exploiting the technologies accumulated so far, including the 1180 MPa grade cold rolled steel sheet with excellent formability introduced in this paper, to further improve the formability and practical properties of steel sheets.

## References

1) Y. Seto. *Bulletin of The Iron and Steel Institute of Japan (Ferrum).* 2013, Vol.18, No.12, p.726.
2) Y. Omiya et al. *R&D Kobe Steel Engineering Reports.* 2007, Vol.57, No.2, p.2.
3) Y. Omiya. *R&D Kobe Steel Engineering Reports.* 2002, Vol.50, No.3, p.20.
4) T. Tamura et al. *R&D Kobe Steel Engineering Reports.* 2002, Vol.52, No.3, p.6.
5) Y. Mukai. *R&D Kobe Steel Engineering Reports.* 2005, Vol.55, No.2, p.30.
6) Y. Futamura et al. *R&D Kobe Steel Engineering Reports.* 2011, Vol.61, No.2, p.41.
7) Y. Futamura. *Materials in Car Body Engineering conference proceedings.* 2015, p.211.
8) Technical Commission on Joining and Material Processing for Light Structures of Japan Welding Society. *Resistance spot welding of steel sheets and aluminum alloy sheets.* 2008.
9) S. Maeda et al. *TETSU-TO-HAGANE.* 1982, Vol.68, No.16, p.2497.
10) S. Matsuyama. *Delayed Fracture rev. 1*, The Nikkan Kogyo Shimbun, Ltd., 1989, p.203.
11) M. Miura et al. *R&D Kobe Steel Engineering Reports.* 2007, Vol.57, No.2, p.15.
12) T. Kashima et al. *R&D Kobe Steel Engineering Reports.* 2002, Vol.52, No.3, p.15.
13) M. Nakaya et al. *R&D Kobe Steel Engineering Reports.* 2009, Vol.59, No.1, p.46.
14) K. Kasuya et al. *R&D Kobe Steel Engineering Reports.* 2007, Vol.57, No.2, p.27.
15) H. Utsumi et al. *R&D Kobe Steel Engineering Reports.* 2017, Vol.66, No.2, pp.3-7.
16) I. Tamura. *TETSU-TO-HAGANE*. 1970, Vol.56, No.3, p.429.
17) T. Hojo et al. *CAMP-ISIJ*. 2005, Vol.18, p.554.
18) M. Nomura et al. *R&D Kobe Steel Engineering Reports.* 2007, Vol.57, No.2, p.74.

# Influence of Type of Loading on Fracture Behavior of High Strength Steel with Very High-Cycle Fatigue

Yusuke SANDAIJI
Materials Research Lab., Technical Development Group

*Fatigue fractures initiating in internal inclusions occurs in high-strength steel in the very high-cycle fatigue region; however, the fracture behavior under cyclic shear stress has yet to have been elucidated. This study involves ultrasonic torsional fatigue tests and ultrasonic axial fatigue tests being performed on the same bearing steel to compare the fracture behavior. The influence of the type of loading on very high-cycle fatigue characteristics is also examined. Both torsional and axial fatigue tests resulted in fractures originating in inclusions and Optically Dark Areas (ODA) were observed in the vicinity of the origins of all the fractures. However, no difference with the type of loading was recognized in the relationship between the ⊿K value, obtained from the inclusion and ODA sizes, and the number of cycles. Nevertheless, there are differences in the type of inclusions that cause fractures. It has been found that in the case of the torsional fatigue test, inclusions elongated in the rolling direction tend to be the originating points of fractures.*

## Introduction

Super high-strength steel, for example bearing steel and spring steel used in transportation machine parts and automobile engines, is known to suffer fatigue fractures that originate in non-metallic inclusions in the steel (hereinafter called "inclusions") in the very high-cycle fatigue life range of exceeding $10^7$ cycles, and many studies have been carried out to elucidate the mechanism involved.[1)-6)] It has been reported that, with very high-cycle fatigue, when a crack originating from an inclusion grows at very low speed, a characteristic area referred to as Optically Dark Area (ODA)[1)] forms around the inclusion, with its formation taking place throughout its entire lifespan.[7)] It has also been reported that the characteristics of very high-cycle fatigue are affected by both the size and type of the inclusion,[8)] however, the mechanism involved in the fracture has remained unknown.

These studies mainly took place using repeated bending stress with a rotary bending fatigue testing machine, or tensile and compressive stress with an ultrasonic axial fatigue testing machine. Meanwhile, the very high-cycle fatigue fractures in coil springs and bearings were yet to have been tested using very high-cycle fatigue life range within a practical time frame with a conventional torsional fatigue testing machine, and thus the fracture behavior and its mechanism have remained unknown. However, while the relevant studies took place due to the development of ultrasonic torsional fatigue testing machines,[9)-12)] Xue et al. performed ultrasonic axial fatigue tests and ultrasonic torsional fatigue tests on the same high-strength steel, and reported that the type of inclusion that is the origin of fractures differs in the two tests.[10)] We therefore performed ultrasonic torsional fatigue tests on bearing steel with different types of inclusions, and then reported that the crack initiation behavior depends on the type of inclusion that is the origin of the fracture.[12)]

In this paper, in order to establish material design guidelines that can be used to suppress inclusion-originating fractures in steel used which is exposed to repeated shear stress, for example coil springs and bearings, ultrasonic torsional fatigue tests under torsional load and ultrasonic axial fatigue tests under axial load were performed using bearing steel, and the fracture morphology resulting from both tests compared in examining the influence of the type of loading on inclusion-originating fatigue fracture behavior.

## 1. Experimental method

### 1.1 Test material and specimen

In making interior-originating fractures easier to occur with oxide as the originating point, an ingot based on the composition of SUJ2 bearing steel was manufactured by atmospheric melting, which increases the oxygen concentration of the molten steel, and then hot forged into a steel bar of 65 mm in diameter for use as the test material. **Table 1** shows the chemical composition of the test material. This test material was spheroiding annealing heated at 1,123 K for 20 minutes, oil quenched, and then tempered at 438 K for 150 minutes. The metallographic structure of the test material was martensite with a Vickers hardness of 698 HV at

Table 1 Chemical compositions (mass%)

| C | Si | Mn | S | Cr | Al | N | O |
|---|---|---|---|---|---|---|---|
| 0.95 | 0.25 | 0.33 | 0.0015 | 1.47 | 0.019 | 0.033 | 0.0048 |

a test load of 98 N. Mirror surface observation revealed a large number of spherical inclusions, which appeared to be oxide. The specimens used in the fatigue tests were sampled to ensure that their axial direction corresponded to the cogging direction of the test material, and then machined into the shape shown in **Fig. 1**. The torsional fatigue test used hour-glass specimens, as shown in Fig. 1 (a), and the specimens with a parallel portion, as shown in (b), were then used, in order to enable inclusion-originated fractures easier to occur by increasing the risk volume. Assuming that risk volume V corresponds to the area where 90% or more of the maximum stress was applied, then both types of the specimens used in the torsional fatigue tests would have a risk volume of 2.85 $mm^3$ and 8.71 $mm^3$, respectively, whereas the specimens used in the axial fatigue tests would have a risk volume of 33.7 $mm^3$. The specimens were mirror polished, and then shot peened to apply compressive residual stress. **Fig. 2** shows the residual stress distribution at an angle of 45° to the specimen axis measured through the X-ray diffraction method. The compressive residual stress was about 500 MPa on the specimen surface, and the maximum compressive stress about 1,200 MPa at a depth of 80 $\mu$m from the surface. The compressive stress decreased as the depth increased: being about 125 MPa at a depth of 250 $\mu$m.

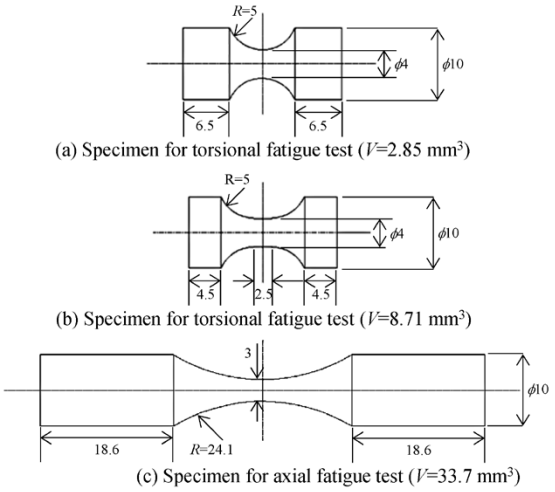


Fig. 1 Shape of specimens

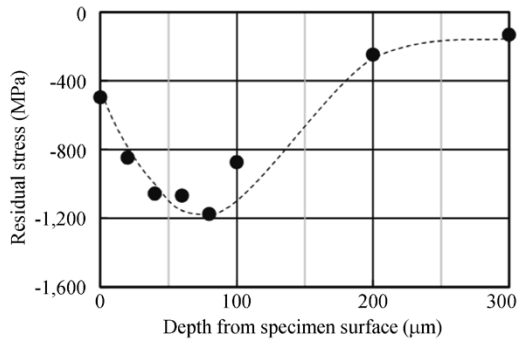


Fig. 2 Distribution of residual stress

## 1.2 Fatigue test

Both the torsional fatigue tests and axial fatigue tests were performed under alternating load and at a test frequency of 20 kHz, using ultrasonic fatigue test machines made by Shimadzu (torsional: UFT-2000T, axial: UFT-2000). Compressed air was used to suppress the heat generated during the fatigue tests. The fatigue tests also took place after having determined the intermittent test conditions, where the specimen surface temperature was maintained at below 50℃ in a preliminary test in which the oscillation stop time was varied within the range of 440 to 1,100 ms while the oscillation time was maintained at a constant of 110 ms.

## 1.3 Fracture surface observation

The fatigue fracture surface observation took place using a Scanning Electron Microscope (SEM) and an Optical Microscope (OM). The inclusion of fracture origins was identified through Energy Dispersive X-ray analysis (SEM-EDX).

The inclusion size $\sqrt{area_{inc}}$ and ODA size $\sqrt{area_{ODA}}$ were calculated using the square root of the respective areas measured through image analysis, namely SEM images and OM images from a direction perpendicular to the fracture surface.

# 2. Experimentation results

## 2.1 Fatigue test results

**Fig. 3** shows the S-N curve. The open plots in the figure represent the surface-originating fractures while the solid plots represent the interior-originating fractures. The alphabetical notations represent the type of inclusion of the origin of the

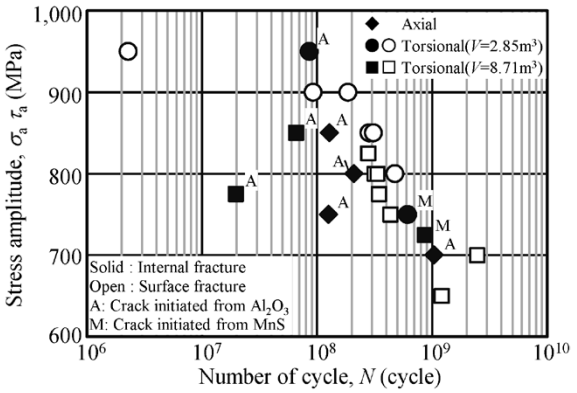


Fig. 3 Results of fatigue tests

fracture: A standing for $Al_2O_3$ based inclusions and M for MnS based inclusions, etc. The S-N curve under torsional load indicated an increase in the number of cycles with decreased stress amplitude, and no influence of the risk volume was observed apart from the fracture point at approximately 2x10$^7$ cycles that had a stress amplitude $\tau_a$ of 775 MPa. According to the fracture surface observation results, which will be described at a later stage, there were a mixture of interior-originating factures and surface-originating fractures. Sakanaka et al. performed ultrasonic torsion fatigue tests using bearing steel without shot peening, and reported that only surface-originating fractures occur at a cycle number of $10^5$ to $10^9$.[13] With respect to this paper, interior-originating fractures seem to have occurred more easily because of the increased number of inclusions due to atmospheric melting and hardened surfaces resulting from the shot peening. Meanwhile, under axial load, the number of cycles increased with decreased stress amplitude, and with all the fractures being of the interior-originating type.

In focusing on the inclusion-originating fracture behavior, this paper will describe the test results where inclusion-originating fractures actually occurred. No influence from the risk volume was observed with torsional fatigue tests specimens and therefore the test results of both types of specimens are handled without distinction.

### 2.2 Fracture surface observation results

**Fig. 4** shows an overview of the fractured specimens from the torsional fatigue tests, where the inclusion-originating fractures occurred. Under torsional load the cracks grew at an angle of 45° to the specimen axis, i.e. in a perpendicular direction to the direction of the maximum principal stress, and therefore the fracture seems to have been caused by the principal stress type crack growth. **Fig. 5** shows SEM and OM images around the origin. All the interior-originating fractures initiated in inclusions, and ODAs were observed around every fracture origin inclusion, excluding the specimen that fractured at 2x10$^7$ cycles under torsional load. When a crack grows in the maximum shear stress direction under torsional load, the fracture surfaces get smoothed out due to the abrasion between them. In this study, however, no smooth fracture surfaces were observed around the origin, but an ODA was observed in the same way as under axial load; therefore, giving rise to the conclusion that fatigue cracks grew due to the maximum principal stress.

Meanwhile, under axial load, an ODA was observed around the inclusion, and the fracture occurred due to principal stress type crack growth in the same way as reported in the past.[1), 4), 6), 7)]

**Fig. 6** shows the relationship between the inclusion size $\sqrt{area}_{inc}$ and the number of cycles $N$. Fractures occurred with inclusions of $\sqrt{area}_{inc}$ = 10 to 80 $\mu$m as the originating points under torsional load and fractures occurred with inclusions of $\sqrt{area}_{inc}$ = 5 to 20 $\mu$m as the originating points under axial load, and hence the $\sqrt{area}_{inc}$ value did not significantly depend on the fatigue life once over $10^8$ cycles. **Fig. 7** shows the relationship between the ODA size $\sqrt{area}_{ODA}$ and number of cycles N. ODAs of $\sqrt{area}_{ODA}$ = 30 to 60 $\mu$m formed under torsional load

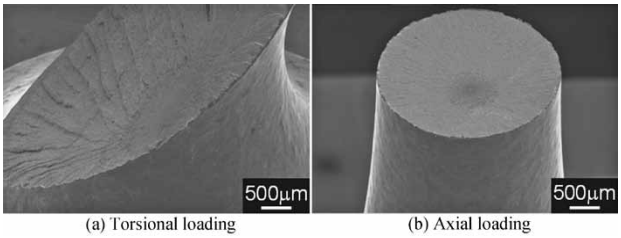

(a) Torsional loading (b) Axial loading

Fig. 4 Overview of fractured specimens

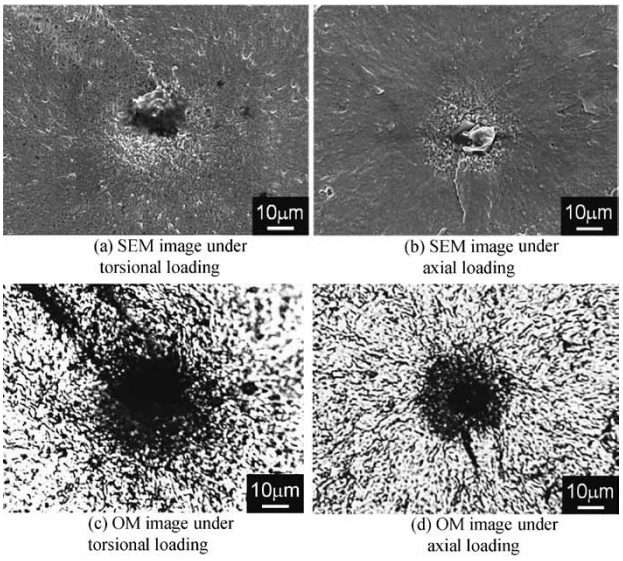

(a) SEM image under torsional loading (b) SEM image under axial loading

(c) OM image under torsional loading (d) OM image under axial loading

Fig. 5 Overview of fractured specimens

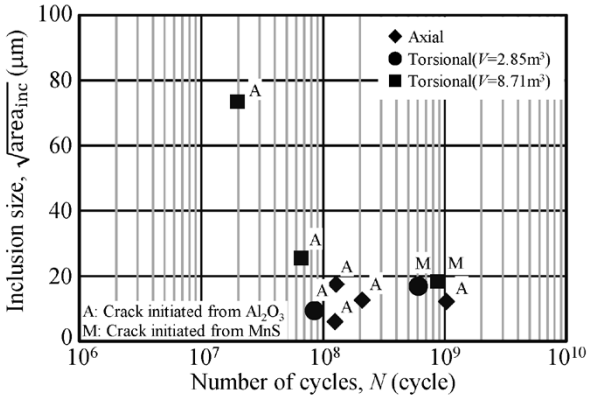


Fig. 6 Relationship between number of cycles and inclusion size

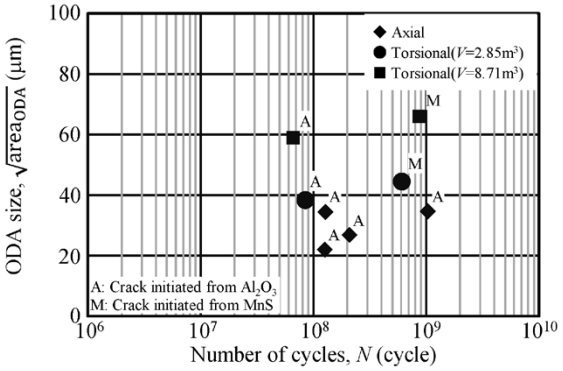


Fig. 7 Relationship between number of cycles and ODA size

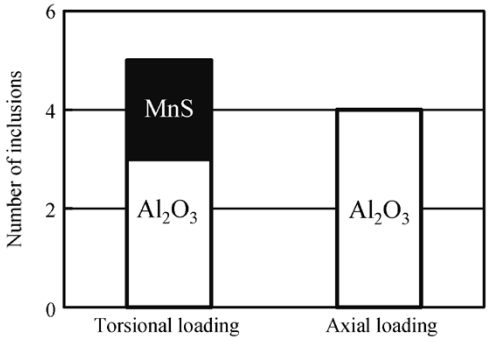


Fig. 8 Type of fracture origin inclusions

and ODAs of $\sqrt{area_{ODA}}$ = 20 to 40 $\mu$m formed under axial load, and hence no significant correlation was observed between the number of cycles and $\sqrt{area_{ODA}}$ value.

**Fig. 8** shows the type of fracture origin inclusion. Under axial load, all the fractures occurred with $Al_2O_3$ based inclusions as the originating point, whereas under torsional load, the fractures occurred with $Al_2O_3$ based inclusions and MnS based inclusions as the originating points, being basically half and half.

## 3. Discussion

### 3.1 Influence of loading type on crack initiation behavior

In addition to $Al_2O_3$ based inclusions, MnS based inclusions were also the fracture origins under torsional load. Based on cross-sectional observation of the fracture origins, we have previously reported that, under torsional load, principal stress type cracks initiate, grow, and then lead to fractures in the case of $Al_2O_3$ based inclusions, whereas shear type cracks initiate, change to principal stress type cracks, and then lead to fractures in the case of MnS based inclusions.[12] In the latter case, the shear type cracks originate from inside MnS based inclusions elongated in the direction of the maximum shear stress, and hence it would appear that the shear type cracks occurred as a result of their projection area in the direction of the maximum shear stress increasing. In this study, the specimens were sampled so that their axial direction would correspond to the cogging direction of the steel material; therefore, the MnS inclusions are elongated in the direction of the maximum shear stress. It would therefore appears that some of them became the originating points of the fractures. Meanwhile, under axial load, it would appear that they did not become the fracture origin because their projection area in the maximum principal stress direction decreased.

### 3.2 Influence of loading type on crack growth

In order to examine the influence of the loading type on the crack growth, the number of cycles was compared with the stress intensity factor range $\Delta K$, which were obtained from the size of the inclusion of the fracture origin and the ODA, under torsional load and axial load, respectively. **Fig. 9** and **Fig.10** show the relationship between the number of cycles and $\Delta K_{inc}$ and $\Delta K_{ODA}$ values, which were obtained from the size of the the fracture origin inclusion and the ODA, respectively. $\Delta K_{inc}$ and $\Delta K_{ODA}$ were calculated using Equation (1) by substituting $\sqrt{area_{inc}}$ and $\sqrt{area_{ODA}}$ for $\sqrt{area}$, respectively.

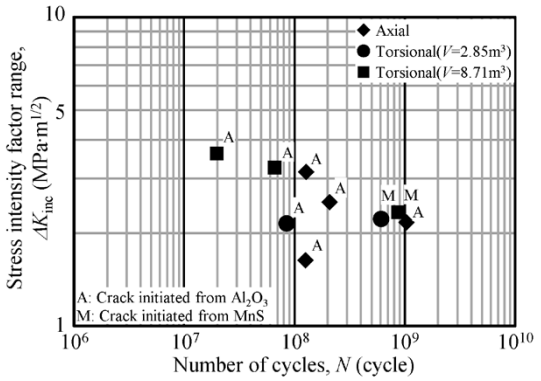


Fig. 9 Relationship between number of cycles and $\Delta K_{inc}$

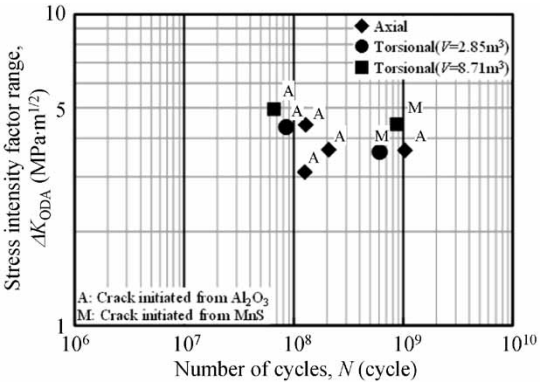


Fig.10 Relationship between number of cycles and $\Delta K_{ODA}$

$$\Delta K = 0.5 \Delta\sigma \sqrt{\pi \sqrt{area}} \quad \cdots\cdots (1)$$

Where, $\Delta\sigma$ represents the stress range applied to a crack, which was obtained by substituting the stress amplitude, assuming that only the tensile component affects the crack growth. The torsional fatigue test took place under alternating load, where the resulting fractures indicate that the cracks grew in the direction perpendicular to the maximum principal stress $\sigma_{pr.}$ as described above. For this reason, using the assumption that Equation (2) can be established, the principal stress amplitude $\sigma_{pr.eff.a}$ was obtained using Equation (3) in consideration of the stress gradient, and then $\Delta K$ by substituting the resulting value into Equation (1).

$$\sigma_{pr.a} = \tau_a \quad \cdots\cdots (2)$$

$$\sigma_{pr.eff.a} = \tau_a (1 - D/R) \quad \cdots\cdots (3)$$

Where, $\tau_a$ represents the maximum shear stress amplitude on the specimen surface, $D$ the depth of the origin from the specimen surface, and $R$ the radius of the specimen.

Under torsional load, $\Delta K_{inc}$ decreases with an increase in number of cycles (Fig. 9); however, $\Delta K_{ODA}$ does not depend on the number of cycles, and remains substantially constant in the range of 3 to 5 MPa-m$^{1/2}$, and thus indicating there to be no difference in the inclusion type (Fig.10). This tendency and the $\Delta K_{ODA}$ value correspond to those under axial load, in the same way as described in a previous report.[2] This indicates that the cracks grow very slowly while forming ODAs in the same way under axial load and bending load, but then changes to general crack growth without forming any ODAs when $\Delta K_{ODA}$ reaches a certain value, and this is because the principal stress type crack growth occurs under alternating torsional load. This means that principal stress type cracks or shear type cracks may depend on the shape of the inclusion when inclusion-originating fractures occur under torsional load; however, the fractures are caused by the principal stress type crack growth in both cases. Once an ODA has formed around the origin and $\Delta K_{ODA}$ reaches a certain value, it then changes to general crack growth, and ultimately a fracture. It has been reported that most of the entire number of cycles is spent on the crack growth that forms ODAs under axial load.[7] It would appear that this crack growth dominates the fatigue life in the same way even under torsional load. For this reason, we will aim at establishing structure design guidelines by clarifying the metallographic factors that suppress such crack growth. In addition, a study is necessary from the viewpoint of not only the metallographic structure but also inclusion control as it would appear that the shape and hardness of the inclusion affects the crack initiation life, because the crack initiation behavior depends on the shape of the inclusion under torsional load.

## Conclusions

Ultrasonic torsional fatigue tests and ultrasonic axial fatigue tests using bearing steel were performed, and the fracture behavior under torsional load and axial load compared, thereby examining the influence of the type of loading on inclusion-originating fracture behavior. The result included the following discoveries.

(1) With crack initiation under torsional load, fatigue fractures occurred with elongated inclusions, such as MnS based inclusions, as the originating point.

(2) With crack growth under torsional load, principal stress type cracks grow with the formation of ODA around the inclusions, regardless of the type of inclusion that causes the fracture, and when $\Delta K_{ODA}$ reaches a certain value, it changes to general crack growth, and then leads to fractures.

(3) The $\Delta K_{ODA}$ values under torsional load and axial load are comparable. Presumably, this is because the principal stress type crack growth occurred under both types of loading.

## References


1) Y. Murakami et al. *Fatigue & Fracture of Engineering Materials & Structures*. 1999, Vol.22, p.581.
2) K. Tanaka et al. *Fatigue & Fracture of Engineering Materials & Structures*. 2002, Vol.25, p.775.
3) C. Bathias. *Fatigue & Fracture of Engineering Materials & Structures*. 1999, Vol.22, p.559.
4) H. Mayer et al. *International Journal of Fatigue*. 2009, Vol.31, p.242.
5) K. Shiozawa et al. *Fatigue & Fracture of Engineering Materials & Structures*. 2001, Vol.24 , p.781.
6) T. Sakai et al. *Fatigue & Fracture of Engineering Materials & Structures*. 2001, Vol.25, p.765.
7) W. Ishida et al. *Transactions of the Japan Society of Mechanical Engineers A*. 2012, Vol.78, p.23.
8) Y. Furuya et al. *Metallurgical and Materials Transactions A*. 2007, Vol.38, p.1722.
9) S. E. Stanzl-Tschegg et al. *Ultrasonics*. 1993, Vol.31, p.275.
10) H. Q. Xue et al. *Engineering Fracture Mechanics*. 2010, Vol.77, p.1866.
11) Y. Shimamura et al. *International Journal of Fatigue*. 2014, Vol.60, p.57.
12) Y. Sandaiji et al. *Procedia Materials Science*. 2014, Vol.3, p.894.
13) N. Sakanaka et al. *NTN TECHNICAL REVIEW*. 2011, Vol.79, p.104.

# Mechanical and Tribological Properties of DLC Films for Sliding Parts

Dr. Hirotaka ITO*1, Dr. Kenji YAMAMOTO*1
*1 Materials Research Lab., Technical Development Group

*Diamond-like carbon (DLC) film has the advantage of having both low friction and low wear, and in recent years it has been applied to various sliding parts, such as parts for internal-combustion automotive engines. This paper presents a study on the mechanical characteristics and sliding properties of DLC films deposited by unbalanced magnetron sputtering (UBMS) equipment. It was clarified that the UBMS equipment can control the amount of hydrogen in a DLC film and as a consequence the mechanical properties of the DLC film can be changed. Furthermore, sliding tests using oil lubrication clarified that controlling the amount of hydrogen in DLC and the choice of additives in the oil are critical to achieving both low friction and low wear at the same time.*

## Introduction

Diamond-like carbon (hereinafter referred to as DLC) films have been attracting attention as a material that achieves both low friction and low wear at the same time. In recent years, the films are being increasingly used in the automotive field with a view to saving energy. Their applications include automobile engine parts such as valve lifters,[1] piston rings,[2] injectors for diesel engine common rail systems[3] and electromagnetic clutch plates.[4] In cases where DLC is used in engine oil, issues of compatibility with the engine oil have been pointed out, along with the properties of the DLC film.[1] In the future, DLC films are expected to be applied not only in the automotive field, but also in various other fields such as general mechanical parts and electronics.

Kobe Steel has a lineup of unbalanced magnetron sputtering (hereinafter referred to as "UBMS") apparatuses for depositing DLC films. This paper describes the structures and mechanical properties of DLC films deposited by a UBMS apparatus under various deposition conditions, as well as the sliding properties of the DLC films obtained.

DLC films are classified by ternary diagram based on hydrogen content and $sp^2/sp^3$ bonding ratio (**Fig. 1**).[5] The films containing no hydrogen are called hydrogen-free DLC films, or amorphous carbon (*a*-C); those with a high ratio of $sp^3$ bonding, which forms a tetrahedral structure, the crystal structure of diamond, are referred to as tetrahedral amorphous carbon (*ta*-C). The films containing hydrogen are classified as hydrogenated amorphous carbon (*a*-C:H) and hydrogenated tetrahedral amorphous carbon (*ta*-C:H). In many cases, *a*-C, *a*-C:H, *ta*-C, and *ta*-C: H are collectively referred to as DLC. The properties of the films can be controlled by introducing constituents other than hydrogen or carbon, and films containing various metals,[6] Si[4] and/or nitrogen[7] are also referred to as DLC films in a broad sense; however, these films with elements other than carbon or hydrogen cannot be included in the classification shown in Fig. 1.

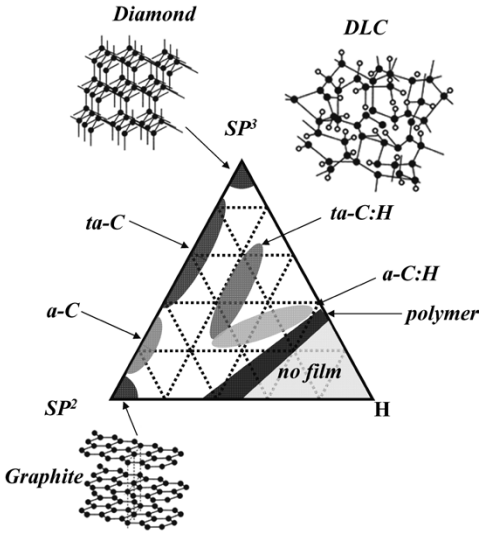


Fig. 1 Ternary diagram of DLC and schematic images of DLC structure

The UBMS process described in this paper can deposit DLC film mainly in the regions designated as *a*-C and *a*-C:H in Fig. 1. The following describes a study conducted on the advantage and sliding properties of DLC films that can be deposited by the UBMS process.

## 1. Test method

Assuming application to automobile engine parts, a sliding test in lubricating oil was conducted on DLC films deposited under various conditions of the UBMS process. This sliding test not only indicates the relationship between the deposition conditions of DLC films and their mechanical properties, but also enables the investigation of how the hydrogen content in DLC films, as well as the additives contained in the lubricating oil, influence the sliding properties.

### 1.1 Deposition method

A schematic diagram of an UBMS apparatus is shown in **Fig. 2**. The inner and outer magnets placed behind a target generate a magnetic field with asymmetric strength, the magnetic field extending to the substrate side, enlarging the plasma region. Application of bias voltage to the substrate during deposition ensures the implantation of argon (Ar) ions from the plasma near the substrate, enabling the control of film properties such as hardness and surface roughness. For the details of the UBMS process, reference may be made to published articles.[9)]

The film deposition described in this paper was accomplished using a compact UBMS apparatus (UBMS 202) manufactured by Kobe Steel. The targets used were carbon (C) and chromium (Cr) disks, each having a diameter of 6 inches. Formation of an intermediate layer is important to ensure adhesion between a substrate and DLC film, which is chemically inactive by nature. In the case of iron-based substrates, for example, the construction of Cr/WC/WC-C gradient composition/DLC film[10)] ensures the adhesion strength of the interfaces at both the substrate/intermediate layers and intermediate layer/DLC film to withstand the sliding in environments such as automobile engine parts. The experiments in this paper do not require a specific level of adhesion for actual parts and adopted a more convenient construction of Cr/WC/WC-C gradient composition/DLC film.

The DLC deposition was conducted in the apparatus with a substrate (a cemented carbide insert, a Si (100) wafer, or a SKH51 disk) installed. The chamber was evacuated to $2 \times 10^{-3}$ Pa or below, which was followed by argon (Ar) ion bombardment for substrate surface cleaning before the deposition of the intermediate layer. The intermediate layer was formed by first depositing a Cr layer, followed by the deposition of a Cr-C gradient composition layer, during which the sputtering power and the amount of introduced gas (Ar and $CH_4$) were controlled. After forming the intermediate layer of Cr/Cr-C gradient composition, a DLC layer was deposited under varying deposition conditions. During the DLC deposition, Ar and $CH_4$ gas were introduced and the total gas pressure was adjusted to 0.6 Pa. The hydrogen content in the DLC films was controlled by the flow rate ratio of the Ar and $CH_4$ gas introduced.

### 1.2 Evaluation method

The surface roughness of DLC films after deposition was measured with an atomic force microscope (hereinafter referred to as "AFM"). Hardness was measured using a nano-indenter based on the Berkovich diamond indenter, and the hardness values were calculated in accordance with the Sawa/Tanaka method[11)] with the correction for indenter tip. The structures of DLC films were analyzed by Raman spectrometry, the film density was measured using Rutherford backscattering spectrometry (hereinafter referred to as "RBS"), and the hydrogen content was analyzed by elastic recoil detection analysis (hereinafter referred to as ERDA).

The sliding test was carried out using a friction and wear tester (Tri-Bot) manufactured by Shinko Engineering Co., Ltd. **Fig. 3** shows a schematic diagram of the sliding test. Various DLC films were deposited on SKH 51 disks ($\phi$ 55 mm × 5 mm). Two vane samples (ea. 3.5 mm × 5.0 mm × 14 mm; tip radius, 5 mm) made of high-carbon chromium bearing steel (SUJ2) were used.

In the sliding test, each disk was placed on a vane in lubricating oil, and the disk was rotated while a load was applied. For lubricating oil, poly-$\alpha$-olefin (PAO), a synthetic hydrocarbon, was used as the base oil. As for additive agent, ester-type glycerin monooleate (GMO) was used; it is known to exhibit a low friction coefficient when combined with DLC

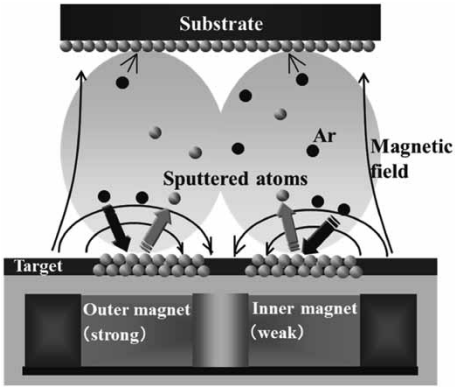

Fig. 2 Schematic image of UBMS[8)]

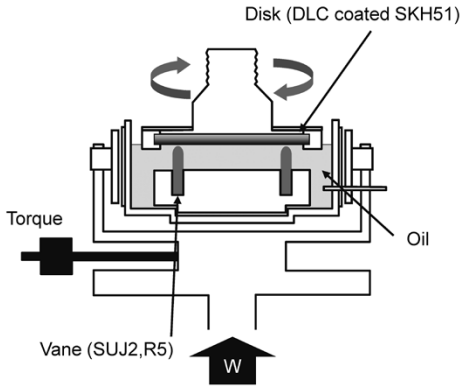

Fig. 3 Schematic image of sliding equipment

film containing no hydrogen.[1] In addition, two types of lubricating oil respectively containing 3 wt% of phosphite and amine phosphate, both being phosphorus additive agents were also used with the remainder of the base oil. The testing conditions were: applied load of 500N, lubricating oil temperature at 80℃ and sliding speed reduced step-by-step from 0.09m/s to 0.02m/s.

After the sliding test the samples were observed with an optical microscope. The wear volume was calculated by measuring the worn cross-sectional profile of each sliding part with a surface profiler. For more detailed analysis of sliding parts, the cross-sections of worn portions were observed by transmission electron microscopy (hereinafter referred to as "TEM"), while compositions were analyzed by Auger electron spectroscopy analysis (hereinafter referred to as "AES").

## 2. Test results and discussion

### 2.1 Change of DLC film properties due to deposition conditions

Controlling the bias voltage applied to substrates during DLC deposition to implant Ar has been expected to improve the quality of DLC films. **Fig. 4** shows the change in DLC film hardness when it is deposited with varying bias voltage applied to the substrates. This figure shows that the hardness of DLC films increases with enhanced negative bias voltage; however, the hardness exhibits no change when the negative bias voltage is greater than 150V. **Fig. 5** shows the results of AFM observation of the surface nanofeatures of the DLC films deposited under different bias voltage conditions. The surface roughness (Ra) was Ra=3.9nm when the bias voltage was 0V and Ra=0.43nm at -200V. It was confirmed that the surface becomes smoother with the increasing negative bias voltage. Taking into consideration the fact that the deposition rate of DLC film decreases with enhanced bias voltage, along with the results above, enhancing the bias voltage of UBMS is considered to have caused the smoothening of the surface by Ar ion etching and the hardening of DLC film by Ar ion implantation.

Next, a study was conducted on the various properties of DLC film when the bias voltage is fixed at -100V and the hydrogen content is changed. The hydrogen content was adjusted by changing the flow ratio of Ar and $CH_4$ gas during deposition. **Fig. 6** shows the change in hardness, measured by a nano-indenter, with the hydrogen content, measured by ERDA, in DLC films. The maximum hardness is reached when the hydrogen content is approximately 10 at% and decreases linearly with higher hydrogen content.

Furthermore, a study was conducted on the correlation between the film hardness and the structure of DLC films. A DLC film has an amorphous structure, not having any crystal structure. Therefore, the techniques, such as X-ray diffraction (XRD), commonly used for the structure analysis of metallic materials cannot be applied. Hence, the Raman spectrometry is generally used as

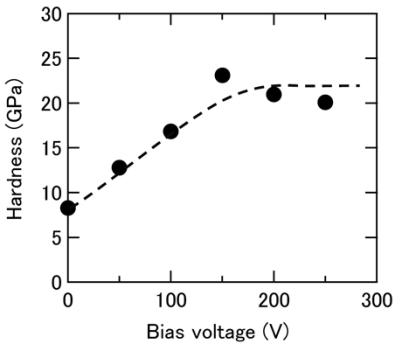


Fig. 4 Relationship between DLC film hardness and bias voltage[8]

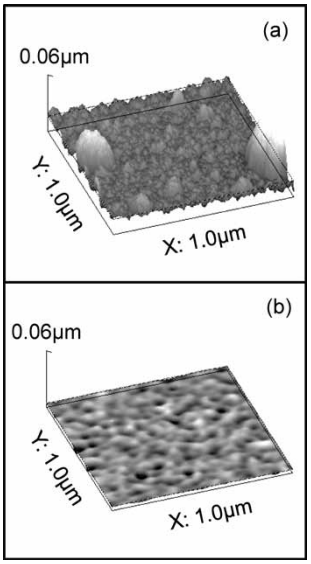


Fig. 5 AFM images of DLC film surface with negative bias voltage (a) 0V, (b) 200V[8]

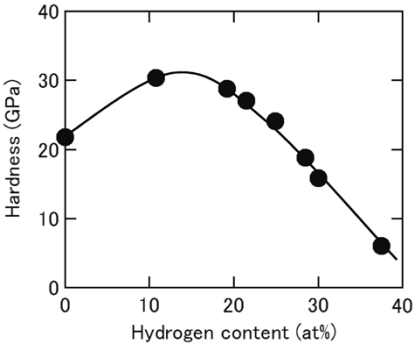


Fig. 6 Relationship between DLC film hardness and hydrogen content[8]

a convenient non-destructive technique for structure analysis. This technique includes irradiating a specimen with light of a specific wavelength and estimating the bonding state, etc., of atoms using the amount of the change in the wavelength of scattered light obtained. In the case of DLC films, the structure can be estimated from the intensity ratio and positions of the *G*-peak (near 1,560cm$^{-1}$) derived from the graphite constituent and *D*-peak (near 1,360cm$^{-1}$) showing the disorder of sp$^2$ bonding. **Fig. 7** shows a Raman spectrometry result for specimens prepared for the test shown in Fig. 6. Each specimen has a *G*-peak shaped with a gentle shoulder at the *D*-peak position and shows the peak shape of a typical DLC film. Peak fitting was carried out on the basis of Fig. 7 to determine the strength ratio of the *D*-peak/*G*-peak and the position of the *G*-peak. No difference was found in the values for each specimen. The results of the Raman spectrometry exhibited no correlation between the structure and hardness.

Next, the density of the DLC film was determined from the RBS measurement. **Fig. 8** shows the correlation between the hydrogen content and film density in a DLC film. Fig. 8 shows the same tendency as the relationship between hardness and hydrogen content shown in Fig. 6, suggesting that the hardness of the DLC film deposited by the UBMS process depends on the density of the DLC film.

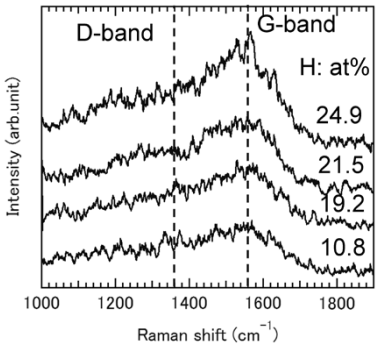


Fig. 7 Raman spectrum of DLC films with various hydrogen content[8)]

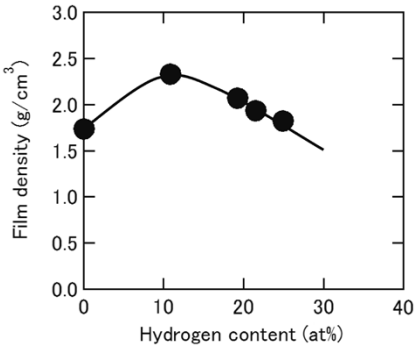


Fig. 8 Relationship between film density and hydrogen content in DLC film[8)]

### 2.2 Evaluation of sliding properties in oil

When DLC films are used in lubricating oil, the sliding properties change greatly not only in accordance with the properties of the DLC films but also by the types of agents added to the lubricating oil. A study was conducted on the combination of DLC film properties and additive agent in lubricating oil from the viewpoint of friction coefficient and wear volume. For the sliding test, the test apparatus described in Section 1.2 (Fig. 3) was used.

**Fig. 9** compares the results of friction tests at the lowest speed (0.02 m /s). The tests were conducted in four types of lubricants, i.e., base oil (PAO), PAO + GMO (3 wt%), PAO + phosphite (3 wt%), and PAO + amine phosphate (3 wt%); the relationships between the average friction coefficient and hydrogen content in the DLC film are shown. The results indicate that the base oil (PAO) exhibits a friction coefficient below 0.1 for a hydrogen content of about 10 at% or less, and the friction coefficient tends to increase with increasing hydrogen content. On the other hand, in the case of base oil with an additive agent, the friction coefficient is lower than that of base oil alone, and a reduction of the friction coefficient is observed even when the hydrogen content is in the range of 10 to 30 at%. In the case of GMO addition, it has been known that the friction coefficient is reduced by combination with hydrogen-free DLC film.[1)] The present study has shown that the same effect is at work in the film containing hydrogen. The phosphite added lubricant reduced the friction coefficient of DLC film containing as much as approximately 30 at% of hydrogen. Compared with other additive agents, the phosphite addition is shown to be effective for DLC films containing a larger amount of hydrogen.

**Fig.10** shows the wear volume of a DLC film and vanes after a sliding test in which a disk (DLC film) containing 26 at% of hydrogen was used. The

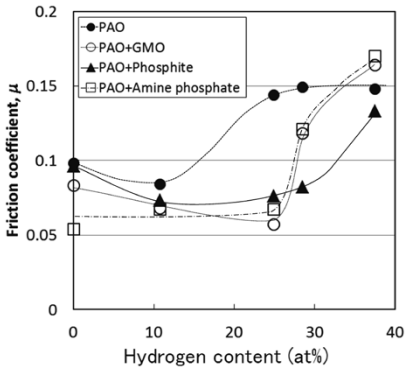


Fig. 9 Relationship between friction coefficients and hydrogen content in DLC films

wear volume of the DLC film decreases with the introduction of additive agent, and the phosphoric acid system has a greater decreasing effect on wear volume than does GMO. Regarding the wear volume of the vanes, the addition of phosphite or amine phosphate exhibits the same level of effect as the base oil without any additive agent. However, the addition of GMO results in an increase, compared with the base oil alone.

**Fig.11** shows the optical micrographs of sliding portions of the DLC films and vanes shown in Fig.10. Wear scars were observed on the DLC film surfaces except for the one tested with phosphite addition. In the observation of the wear scars on the vanes, the base oil resulted in the formation of accretion on the sliding portion, whereas the phosphite addition resulted in a slight accretion on the sliding portion and accretion on the non-sliding portion as well. Furthermore, in the cases of GMO addition and amine phosphate addition, no clear accretion was observed in the sliding portion, while accretion was observed in the non-sliding portion.

For the discussion of accretion and the behavior of friction wear, TEM observation was made on the cross-section of the sliding portions of the DLC films and vanes. **Fig.12** shows the cross-sectional TEM image of the sliding portion of the DLC film after the sliding test with the addition of amine phosphate shown in Fig.11. The figure on the left (a) is a full image, and the one on the right (b) is an enlargement of the vicinity of the outermost surface (sliding portion). No clear reaction product was confirmed on the DLC film surface after the sliding test, and only the amorphous structure of the DLC film was confirmed from the diffraction pattern of the enlarged image (figure on right (b)). Also, the composition analysis by AES shows predominantly carbon constituent derived from the DLC. The same result was obtained for other DLC film surfaces after the test, and no definite reaction product was formed on any sliding surface of the DLC films.

On the other hand, it was confirmed that accretion was formed on all the specimens, as shown in the cross-sectional TEM images of vane surface after the sliding test as shown in **Fig.13**. These accretions are considered to be tribofilms (reaction films composed of DLC film, vane (SUJ 2) and oil derived constituent, formed on the sliding surfaces during sliding). The formation of these tribofilms is considered to have greatly affected the friction wear behavior. **Table 1** summarizes the results of the sliding test, TEM observation of Fig.13 and the composition analysis of the tribofilms by AES. In the

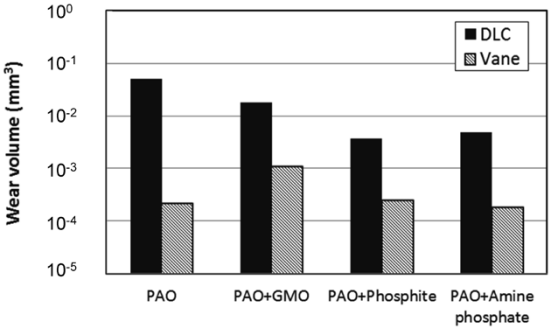


Fig.10 Wear volume of DLC disk and SUJ2 vane after sliding tests

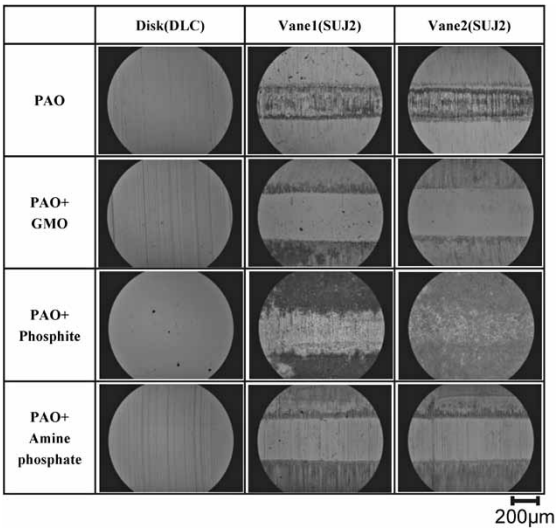


Fig.11 Optical microscope images of DLC disk and SUJ2 vane after sliding tests

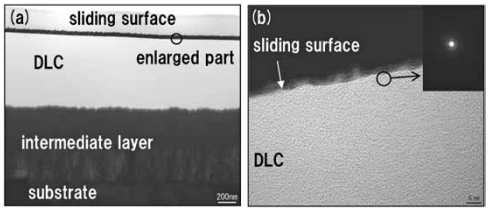


Fig.12 Cross-sectional TEM images of DLC surface after sliding test in amine phosphate additive oil

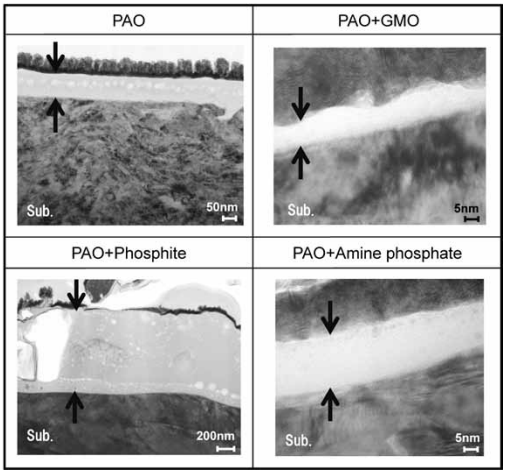


Fig.13 Cross-sectional TEM images of vane surface after sliding tests

Table 1 Results of sliding tests in various types of lubricating oil

| | Hydrogen content (μ<0.1) | Disk wear | Vane wear | Content of tribofilm | Tribofilm thickness |
|---|---|---|---|---|---|
| PAO | < 11at% | 1 | 1 | Fe-C-O | about 100 nm |
| PAO+ GMO | < 25at% | 0.36 | 5.15 | Fe-C-O | about 10 nm |
| PAO+ Phosphite | < 29at% | 0.07 | 1.16 | Fe-P-O | over 1 μm |
| PAO+ Amine phosphate | < 25at% | 0.10 | 0.86 | Fe-P-C-O | about 20 nm |

cases of the base oil and GMO addition, tribofilms based on Fe-C-O are formed on the surfaces of the vanes. When the base oil is used as is, a thick tribofilm based on Fe-C-O is formed. It is inferred that the friction coefficient became high due to the high shear resistance of this tribofilm.

On the other hand, another tribofilm, also based on Fe-C-O but having a low shear resistance, is considered to have formed when GMO is added. In the case of GMO addition, however, the wear volume of the vane is larger, and the tribofilm is as thin as about 10 nm. Thus, it is inferred that a less protective film is formed on the vane, and the wearing vane continued to supply the tribofilm based on Fe-C-O.

In the case of phosphite addition, a tribofilm based on Fe-C-O was formed as thick as 1 μm or more. This film seems to have enabled both the reduced wear volume of vanes and reduced shear resistance (low friction).

Furthermore, in the case of amine phosphate addition, a film based on Fe-P-C-O with reduced shear resistance is considered to have formed. It should be noted, however, that despite the formation of a tribofilm as thin as approximately 20 nm, amine phosphate can achieve both the reduction of vane wear volume and low friction. The phosphorus based constituent seems to have caused behavior different from that of GMO.

Although in the same phosphorus system, phosphite and amine phosphate are different in the presence of amine constituent, and the amine constituent included in amine phosphate seems to have contributed to the friction wear behavior. Hence, in order to investigate the influence of the amine constituent, time-of-flight secondary ion mass spectrometry (TOF-SIMS) apparatus was used to analyze in more detail the sliding and non-sliding portions of the DLC film surface after the sliding test in the oil containing amine phosphate, the details of which could not be confirmed by the cross-sectional TEM observation. Thus, the phosphate constituent has been confirmed as concentrating in the sliding portion of the DLC film, and the C-N based constituent derived from amine was confirmed as occurring in the entire DLC film surface irrespective of its location in the sliding portion or the non-sliding portion. From this, it is inferred that the phosphate constituent concentrating on the sliding portion improves the wear resistance and that the CN constituent present in the entire DLC film surface contributes to the reduction of the friction coefficient. The TOF-SIMS observes and analyzes the molecular bonding states at adsorption levels and captures microscopic phenomena finer than the tribofilm on the vane surfaces observed by cross sectional TEM. The correlation between the formation of tribofilm and adsorption, as well as the detailed effect of each additive agent, will be future subjects.

From the above results, it was found that both a low friction coefficient and wear resistance can be achieved at the same time by using a DLC film with controlled hydrogen content in combination with an appropriate additive agent.

## Conclusions

The UBMS apparatus can change the hydrogen content and mechanical properties in DLC films by controlling the deposition conditions. Assuming parts for automobile engines, sliding tests were performed in lubricating oil. It has been clarified that low friction and low wear can both be achieved by appropriately combining the control of hydrogen content and the additive agent in lubricating oil.
The application of this technology to sliding parts of automobile engines is expected to reduce friction loss and contribute to the improvement of fuel consumption.

## References


1) A. Erdemir et al. *Superlubricity*. ELSEVIER, 2007, pp.471-492.
2) T. Higuchi et al. Proceedings of the Society of Automotive Engineers of Japan. 2011, No.154-11, pp.13-16.
3) Y. Murakami et al. The Tribology. 2010, No.272, pp.44-47.
4) H. Tachikawa et al. Materia Japan. 2005, Vol.44, No.3, pp.245-247.
5) J. Robertson. Mater. Sci. Eng. R. Rep. 2002, Vol.37, pp.129-281.
6) K. Bewilogua et al. Thin Solid Films. 2004, Vol.447-448, pp.142-147.
7) C. Donnet et al. *Tribology of Diamond-Like Carbon Films. Springer*, 2008, pp.339-361.
8) H. Ito. The Japan Society of Plasma Science and Nuclear Fusion Research. 2016, Vol.92, No.6, pp.454-459.
9) K. Akari. R&D Kobe Steel Engineering Report. 2008, Vol.58, No.2, pp.28-31.
10) Denso Co. Ltd. et al. *DIAMONDLIKE CARBON HARD MULTILAYER FILM FORMED BODY, AND PRODUCTION METHOD THEREFOR*. JP2003171758, 2003-6-20.
11) T. Sawa et al. J. Mater. Res. 2001, Vol.16, pp.3084-3096.

# Surface Treatment Technologies of Aluminum Alloy for Automobiles

Yosuke OTA*1, Tetsuya KOJIMA*1

*1 Aluminum Sheets & Coils Research Dept,. Moka Plant, Aluminum & Copper Business

*Light materials, such as aluminum alloy sheets, are increasingly being used for the purpose of reducing weight in automotive bodies. Regarding the surface characteristics required for such aluminum alloy sheets, emphasis is being placed, especially in Europe, on bonding durability to suppress the deterioration of joints bonded using adhesive in environments such as salt water spray conditions. Titanium/zirconium (Ti/Zr) treatment is a surface treatment adopted by automotive manufacturers outside Japan to improve the bonding durability of automotive aluminum materials. In Europe, electric discharge texturing (EDT) surfaces, as well as dry lubricant, are being used in addition to Ti/Zr treatment. In order to use materials that are surface treated in accordance with European specifications, the process conditions, including conversion coating, must be optimized. Kobe Steel can provide Ti/Zr treatment, EDT surfaces and dry lubrication.*

## Introduction

With a social need to improve the fuel consumption of automobiles as a climate change mitigation measure, light materials, such as aluminum alloy sheets, are increasingly being used for reducing the weight of automotive bodies, which would be a promising measures for that purpose. Surface characteristics required for aluminum alloy sheets for automotive panels include weldability and the ability to be lubricated for forming. It is necessary to uniformly apply conversion coating, such as zinc phosphate treatment, to provide acceptable painting quality and corrosion resistance, and thereby requiring the ability to be degreased and chemical treatability. On the other hand, emphasis is now being placed, especially in Europe, on bonding durability to suppress the deterioration of joints bonded using adhesive in environments such as salt water spray conditions. Bonding with adhesive is positioned as a secondary measures for mechanical joining or welding; however, it contributes also to improvement in rigidity, safety in collisions, and NVH properties (Noise, Vibration, and Harshness). In order to improve the bonding durability of joints bonded using adhesive, a surface treatment to suppress the deterioration of the interface between adhesive and base material has been developed.

This paper evaluated the characteristics of Ti/Zr treatment as applied to Kobe Steel's products, a treatment which is extensively used especially in Europe to improve bonding durability. It examined also the application of the Electron Discharge Texturing (hereinafter referred to as EDT) method to our products, a method which controls dry lubrication and surface roughness to improve the ability to be lubricated. The results are reported below.

## 1. Ti/Zr treatment

Generally in Japan, aluminum alloy sheets for automotive panels are subject to acid pickling, etc. to remove the oxide film generated in the annealing process,[2] and then shipped as raw material. By contrast in Europe, Ti/Zr treatment is applied at the raw material stage as a surface treatment, in addition to such acid pickling treatment, etc.[1), 3)] Ti/Zr treatment is a technology that has been extensively used by overseas automotive manufacturers, including German-affiliated companies, and it features oxide films of Ti/Zr formed on the surface of aluminum alloy with oxide film removed, using oxide hexafluoride of Ti and Zr.[4] The film formed on the surface is known not to interfere with formability, weldability, and zinc phosphate treatability, in addition to its contribution to improving bonding durability.

### 1.1 Ti/Zr treatment process

**Fig. 1** shows the manufacturing and processing process of aluminum sheets for automotive panels from the viewpoint of the technologies related to surface treatment. **Fig. 2** shows the Ti/Zr treatment process that is performed in the surface treatment process shown in Fig. 1. Heat-treated cold-rolled coils require the removal of oxide film, in advance, through acid pickling to be performed after alkaline degreasing. Ti/Zr coating is then formed by spraying a chemical agent for Ti/Zr treatment and thereafter rinsing and drying. We formed the Ti/Zr coating using Gardobond® X4591 provided by Chemetall as a chemical agent for Ti/Zr treatment. **Fig. 3** shows the cross-sectional observation photo of this Ti/Zr coating. This photo shows that an oxide film of

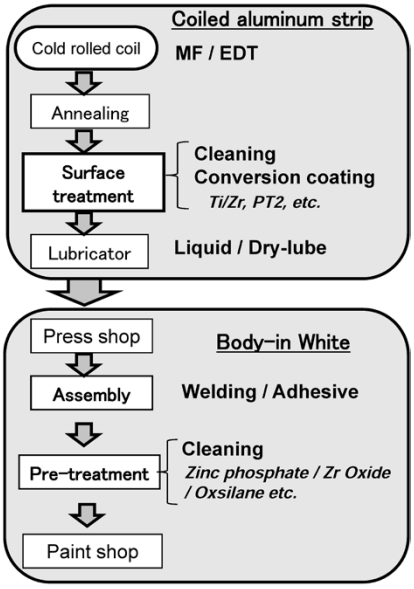


Fig. 1 Manufacturing process of automotive aluminum sheets (surface related technology)

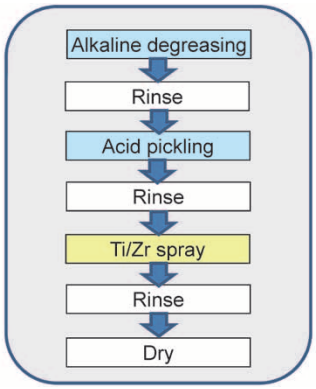


Fig. 2 Process flow of surface treatment for coiled aluminum strips

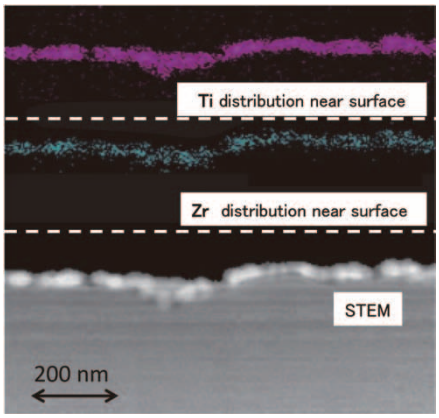


Fig. 3 Cross-sectional image and distribution of Ti, Zr in Ti/Zr conversion coating

several tens of nanometers in thickness containing Ti and Zr has been formed.

### 1.2 Bonding durability and hydration of Ti/Zr coating material

**Fig. 4** shows the evaluation results of bonding durability after salt spray tests for 3,000 hours using our 6022 alloy both with Ti/Zr coating and with acid pickling and rinsing only (hereafter referred to as material with cleaning only). Specimens for shear tests were manufactured using epoxy resin based adhesive, zinc phosphate electrodeposition coating was applied, and then shear tests were performed before and after durability tests. The results revealed that the material with Ti/Zr coating scarcely decreases in its cohesive failure rate and adhesive bonding strength, but is superior in bonding durability, when compared with the material with cleaning only.

Factors in the deterioration of bonding durability in the interface between adhesive and aluminum base material include the hydrated oxide produced on aluminum surfaces when moisture penetrates and is diffused near the interface.[1] **Fig. 5** shows the

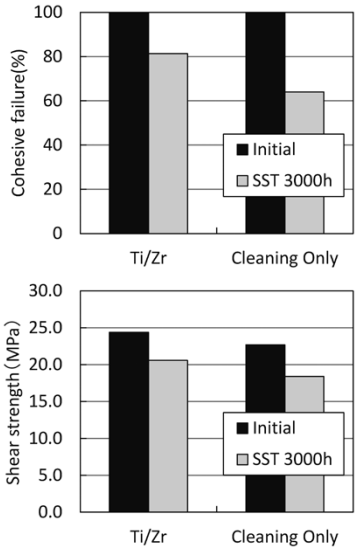


Fig. 4 Adhesive durability (cohesive failure ratio and shear strength) of 6022 alloy with and without Ti/Zr coating

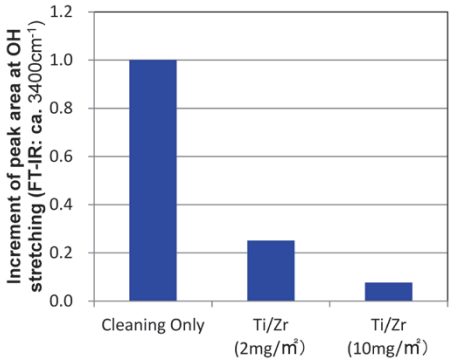


Fig. 5 Influences of Ti/Zr coating on hydration (50℃, 95%RH, 24 hrs)

influences of Ti/Zr coating on hydration. Ti/Zr coating proves that, once formed, it suppresses hydration on the base material surface that is equivalent to a bonding interface. It would appear that this difference in hydration behavior corresponds to bonding durability[5].

### 1.3 Influence of Ti/Zr coating on zinc phosphate treatment, filiform corrosion resistance, and weldability

The influence of Ti/Zr treatment on zinc phosphate treatment and filiform corrosion resistance was evaluated using 6022 alloys and general test conditions. **Fig. 6** shows the observation results of the change in the film weight of zinc phosphate coating and its morphology when varying the amount of fluoride in a zinc phosphate treatment bath, for both materials with Ti/Zr coating and with cleaning only. The results reveal that the material with Ti/Zr coating has achieved a zinc phosphate treatability equivalent to that of the material with cleaning only. However, the film weight of the zinc phosphate coating may decrease in the case of material with a large film weight of Ti/Zr coating, or depending on the conditions of zinc phosphate treatment. While chemical agents for other than zinc phosphate treatment have been used as environmental measures[6), 7)], it seems that the chemical agent for Ti/Zr treatment can be applied in place of these various chemical agents by adjusting the treatment conditions.

**Fig. 7** shows the filiform corrosion test results of material with zinc phosphate treatment and electrodeposition coating. The results revealed that the material with Ti/Zr coating achieves basically the same filiform corrosion resistance as the material with cleaning only.

**Fig. 8** shows the MIG and laser welding tests results for the weldability evaluation using Kobe Steel's 6016 alloy. During tensile tests, every specimen was fractured in the base material but not

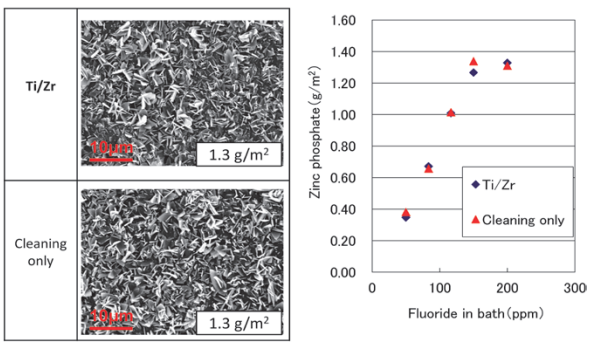


Fig. 6 Surface morphology and film weight of zinc phosphate coating

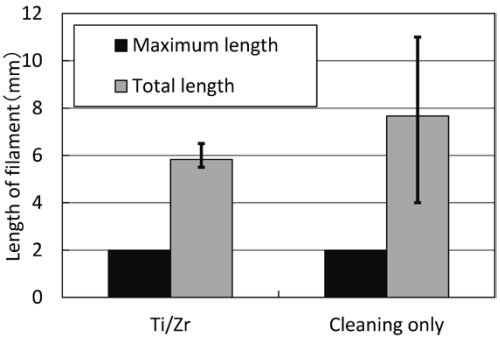


Fig. 7 Filiform corrosion test results of materials with and without Ti/Zr coating after 8 cycles
Cycle: SST 35℃×24 hrs−40℃, 85%RH×120 hrs−r.t. 24h

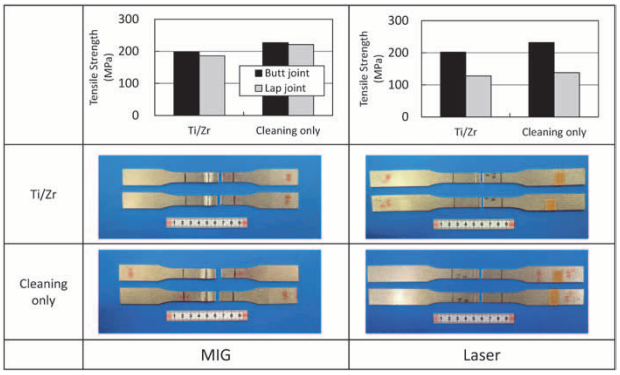


Fig. 8 Tensile strength test after welding

in the weld, showing that the level of strength was the same. It thereby proved that the material with Ti/Zr coating achieves the weldability equivalent to that of the material with cleaning only.

## 2. EDT and dry lubrication

### 2.1 Control of surface roughness by EDT

Mill Finish (hereinafter referred to as MF) material is used in Japan, whereas EDT material is extensively used in Europe. EDT features surface morphology formed by rolling with rolls that were dull electric discharge machined. **Fig. 9** shows the comparison of the surface morphology in 6022 alloy between EDT and MF. The surface morphology with EDT has no rolling line, indicating that it is a morphology having irregularity without anisotropy.

When dry lubrication is used, which will be described at a later stage, two sheets may adhere to each other in a destacking process, in which stacked aluminum sheets are lifted. However, it is known that the material surface morphology with EDT suppresses adhesion, thereby improving the workability in the destacking process.[3] The advantage of dry lubrication includes behavior that eliminates the influence of forming direction in the

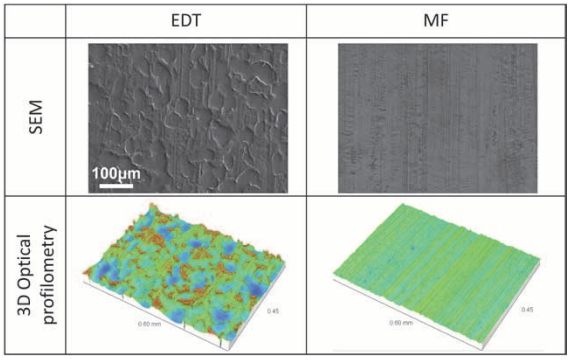


Fig. 9 Comparison of surface morphology between EDT and MF

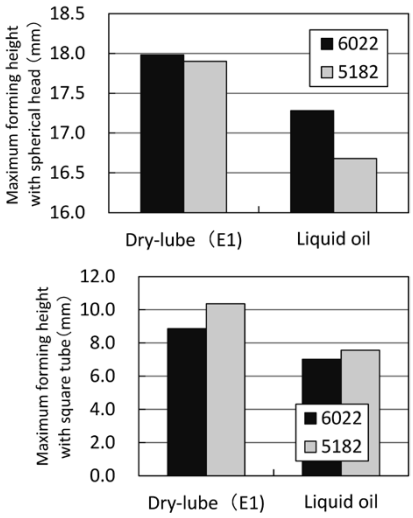


Fig.10 Influence of dry lubrication on punch stretch forming (using spherical head ($\phi$50mm) and square tube (50mm))

forming process, allows lubricant to be retained more easily, thereby contributing to improvement in formability, eliminating anisotropy in the appearance after coating, etc.[8)]

### 2.2 Improvement in formability through applying dry lubrication

In order to improve formability, paraffin wax, surfactant, etc. with a melting point of about 40 to 50℃ are used as dry lubricant. In various methods, dry lubricant is applied mostly by heating, melting, and then electrostatic spraying. **Fig.10** shows the formability when dry lubricant E1 from Zeller + Gmelin is used with 6022 alloy and Kobe Steel's 5182 alloy. The results reveals that excellent punch stretch forming height and drawing height are achieved when compared with using liquid oil. On the other hand, dry lubricant is inferior in its capacity for being degreased; therefore, dry lubricant could not be removed sufficiently using the same degreasing conditions as are used for liquid oil. It appears that when dry lubricant is applied it is necessary to adjust the concentration and temperature of a degreasing bath.

## Conclusions

Ti/Zr treatment is a surface treatment adopted by automotive manufacturers outside Japan, and it improves bonding durability of aluminum material for automobiles. In Europe, EDT surfaces, as well as dry lubricant, are being used in addition to Ti/Zr treatment. Not only in Europe but also in North America, there is a need to improve bonding durability, and chromium-free PT2 consisting of colloidal silica (developed by Novelis), ALCOA951 consisting of organic components, and new surface treatment, such as thin film anodic oxidation, also beginning to be applied, and they are currently supplied to overseas automotive manufacturers.[1)] However, when such "surface treatment agent for overseas use" is used in Japan, optimized conversion treatment conditions are required. Kobe Steel therefore promotes the development of the surface treatment technology that corresponds to the surface treatment conditions used in automotive manufacturers in Japan. Kobe Steel can provide Ti/Zr treatment material, and EDT and dry lubrication treatment materials.

## References

1) *EAA Aluminium Automotive Manual - Joining 9. Adhesive bonding*. http://c.ymcdn.com/sites/www.aec.org/resource/resmgr/PDFs/9-Adhesive-Bonding_2015.pdf, (Accessed 2016-04-26).
2) H. Ishii. *Surface Technology*. 1997, Vol.48, No.10, p.691.
3) G. M. Scamans et al. *Surface and Interface Analysis*. 2013, Vol.45, No.10, pp.1430-1434.
4) O. Lunder et al. *Surface and Coatings Technology*. 2004, Vol.184, No.2, pp.278-290.
5) T. Kojima et al. *Japan Institute of Light Metals, 127th Annual Autumn Meeting Proceedings*. 2014, pp.143-144.
6) Werner Rentsch. *Automotive Finishing JOT-International Surface Technology*. 2012, Vol.5, Issue 1, pp.16-19.
7) T. Higashii. *Coating Technology*. 2013, Vol.52, No.7, pp.51-55.
8) *The Aluminium Automotive Manual - Manufacturing - Surface finishing*. http://european-aluminium.eu/media/1529/aam-manufacturing-4-surface-finishing.pdf, (Accessed 2016-04-26)

# Highly SCC Resistant 7000-series Aluminum Alloy Extrusion

Dr. Takahiro SHIKAMA*1, Dr. Shinji YOSHIHARA*1

*1 Aluminum Extrusion & Fabrication Plant, Chofu Works, Aluminum & copper Business

*A study was conducted to develop extrusions of high-strength 7000-series aluminum alloy with excellent stress corrosion cracking (SCC) resistance. The target proof stress was 400MPa. Normally, the SCC resistance of 7000-series alloys decreases with increasing strength. This study focused on the mechanism of SCC; namely, the anodic dissolution of a boundary precipitate, $MgZn_2$. The electric potential of this precipitate was controlled to suppress its anodic dissolution and to improve the SCC resistance. In addition, the addition of Zr was confirmed to suppress recrystallization, and the surface recrystallization, which deteriorates SCC resistance, has been suppressed. This paper introduces the elemental technologies regarding the development of this alloy for achieving both high strength at the level. of 400MPa proof stress and SCC resistance.*

## Introduction

Against the backdrop of recent environmental issues, strict fuel economy standards have been established for automobiles in Japan, North America, Europe, and other countries.[1] Automobile manufacturers are promoting the weight reduction of vehicle bodies to improve fuel economy. One method of reducing vehicle body weight is to replace parts made of conventional low-strength iron with those made of high-tensile-strength steel or aluminum alloys having higher specific strength. The automobile parts that can be replaced with ones made of aluminum include bumpers, which are energy absorbing members for protecting occupants upon collision. In Japan, the use of aluminum for bumpers started in the 1990's, during which time the 6000-series alloys with a proof stress of 230MPa class were adapted, and 7000-series alloys with proof stress exceeding 300MPa have partially been used since then. In recent years, further weight reduction needs and heightened collision-safety standards are expanding the demand for 7000-series alloys with a proof stress of 400MPa class.

In the case of 7000-series alloys, which are Al-Zn-Mg based, the sensitivity to stress corrosion cracking (hereinafter referred to as "SCC") increases with increasing strength.[2] The alloy newly developed this time focuses on the balance between the two contradicting characteristics of strength and SCC resistance. **Table 1** shows the mechanical properties (typical values) of an extrusion made of the new alloy. The strength is in the class of proof stress 400MPa, which is more than 100MPa higher than the strength of the typical 7000-series alloys conventionally used for welded structures. This paper introduces the method of improving SCC resistance, which was a point of development for the new alloy.

**Table1** Mechanical properties of new alloy extrusion (Typical)

| Alloy | Temper | Yield Stress (MPa) | Tensile Strength (MPa) | Elongation (%) |
|---|---|---|---|---|
| New alloy | T7 | 400 | 450 | 14 |
| 7003 | T5 | 255 | 315 | 15 |
| 7N01 | T5 | 290 | 345 | 15 |

## 1. Occurrence mechanism of stress corrosion cracking

### 1.1 Theory for anodic dissolution of grain boundary precipitates

**Fig. 1** is a schematic diagram showing the mechanism of SCC. Stress corrosion cracking of aluminum alloy is a phenomenon in which a crack occurs at a grain boundary and propagates from there when an alloy with a high SCC sensitivity is exposed to a corrosion environment under tensile stress exceeding a critical stress. Several theories exist for the mechanism of its occurrence, including a hydrogen embrittlement theory and mechanochemical theory.[3] During the development of the present alloy, attention was paid to the so-

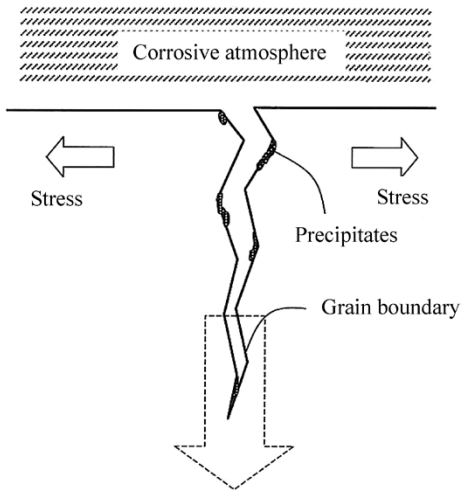


**Fig. 1** Schematic of SCC mechanism

called anodic dissolution theory,[4] which attributes the phenomenon to the dissolution of precipitates ($MgZn_2$ in the case of 7000-series alloys) on grain boundaries. To illustrate the anodic dissolution theory, a schematic diagram depicting the potential difference near the grain boundary is shown in **Fig. 2**. It is believed that the regions without precipitates, i.e. precipitate free zones (PFZs), have an electric potential higher than the potential inside grains due to the depletion of the solid solution elements, Zn and Mg. On the other hand, grain boundaries are dotted with precipitates ($MgZn_2$) sized larger than the intragranular precipitates. These grain boundary precipitates have the lowest electric potential, causing a significant potential difference with the PFZs. Once such a material is placed in a corrosive environment, the resulting potential difference causes the preferential dissolution of the grain boundary precipitates. In the development of the present alloy, the potential difference between PFZs and grain boundary precipitates was minimized to suppress the anodic dissolution of grain boundary precipitates and thus to improve SCC resistance. The method of minimizing the potential difference between PFZs and grain boundary precipitates will be described later.

### 1.2 Observation of SCC crack tip

The tip of an SCC crack that had occurred in a 7000-series alloy was observed in detail by SEM to elucidate the dissolution of $MgZn_2$ caused by anodic reaction. **Fig. 3** shows the SEM images of the SCC crack tip. The tested material was a T5-heat-treated material of a 7000-series alloy extruded for conventional bumpers. A specimen 2mm thick x 10mm wide x 50mm long was cut out from the extruded material in a direction vertical to the extrusion direction, and stress was applied using a three-point bending jig. In the SCC test, the specimen was immersed in a solution containing chromic acid ($0.3\%NaCl\text{-}3.0\%K_2Cr_2O_7\text{-}3.6\%CrO_3$), which had been heated to a range from 95 to 100℃.

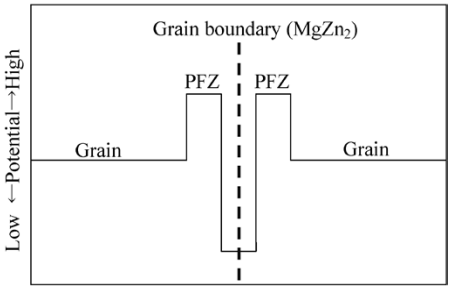


Fig. 2 Schematic of potential difference at grain boundary

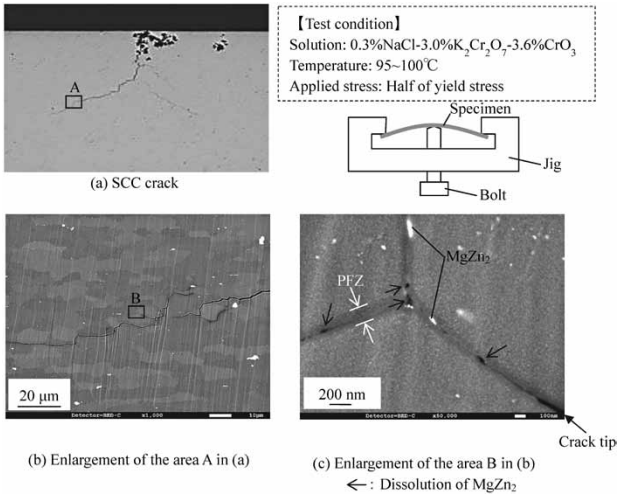


Fig. 3 SEM images of SCC crack tip (Conventional 7000-series alloy)

The specimen surface was visually observed every 2 hours, and the test was interrupted upon SCC occurrence. The specimen was then subjected to SEM observation.

As shown in Fig. 3(c), $MgZn_2$ of about 100 to 200nm is observed on grain boundaries. Cavities, presumably caused by the melting of $MgZn_2$, were observed near the crack tip. These cavities on grain boundaries, caused by anodic dissolution of $MgZn_2$, were considered to be connected and propagated by the tensile stress applied to the crack tip.

## 2. Improvement of SCC resistance for developed alloy

### 2.1 Potential difference control at grain boundaries by Cu addition

It has been known that the addition of an element with noble potential, such as Ag and Cu, to 7000-series alloys improves their SCC resistance.[5] This is because the coexistence of Ag or Cu with $MgZn_2$ on grain boundaries reduces the difference in potential with PFZ and suppresses the anodic dissolution of $MgZn_2$. In the present alloy, Cu was selected because it is commonly used in many aluminum alloys and relatively inexpensive compared with Ag. **Fig. 4** shows the effect of Cu addition on the SCC life of alloys. Three types of materials were tested: they all are in the form of extruded billet based on a 7000-series alloy and respectively contain 0%, 0.2% and 0.35% of Cu (the % expressions herein used represent weight percent). A hot-extrusion of a hollow rectangular pipe with a wall thickness of 2mm was subjected to artificial aging treatment. Specimens were cut out in the direction vertical to the extrusion direction. A three-point bending jig was used to apply stress,

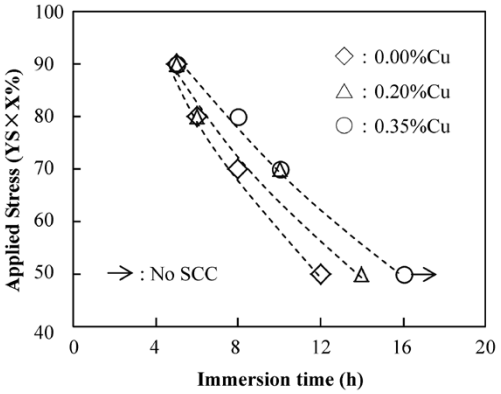


Fig. 4 Effect of Cu addition on SCC life

and immersion test was conducted in chromic acid to compare SCC life. Increasing addition of Cu was found to increase the SCC life. Comparing at an applied stress that is 50% of the proof stress, SCC occurred after 12 hours in the material with no Cu addition, whereas no SCC occurred in the material with a 0.35% Cu addition. The addition of 0.35% of Cu improved SCC life by at least 30% compared with the material without additives.

**Fig. 5** shows the EDX analysis results of grain boundary precipitates, $MgZn_2$, in the extrusions of the alloy with a Cu addition of 0.15% and 0.30% respectively. A trace amount of Cu was detected from the $MgZn_2$ on grain boundaries. The material with 0.30% Cu addition exhibits a peak that is twice higher than that of the material with 0.15% Cu addition. This indicates that the Cu content in $MgZn_2$ on grain boundaries tends to increase with the increasing addition of Cu. This effect is considered to have improved the SCC resistance.

### 2.2 Suppression of surface recrystallization

SCC is also affected by the size of grains. In 7000-series alloys, transition elements such as Mn, Cr and Zr are added to realize the pinning of grain boundaries by the precipitates of these elements. Extruded materials exhibit fibrous structures (partially with subgrains), in which grains are elongated in the direction of extrusion. On the other hand, extrusion surfaces are subjected to strong shear deformation due to friction between the dead metal and extruding die as they pass through the die. The resulting strain, along with processing heat and the heat of friction with the die, becomes the driving force to promote surface recrystallization. If the recrystallized grain generated in the extrusion surface layer is coarse, the SCC resistance is lowered. Hence, in the developed alloy, Zr was also added to suppress the surface recrystallization at the same time. **Fig. 6** shows the relationship between the amount of Zr added to the base alloy and the suppression of recrystallization in the extruded material. When the Zr content is 0.08%, partially recrystallized grains are observed, indicating insufficient suppression of recrystallization. When

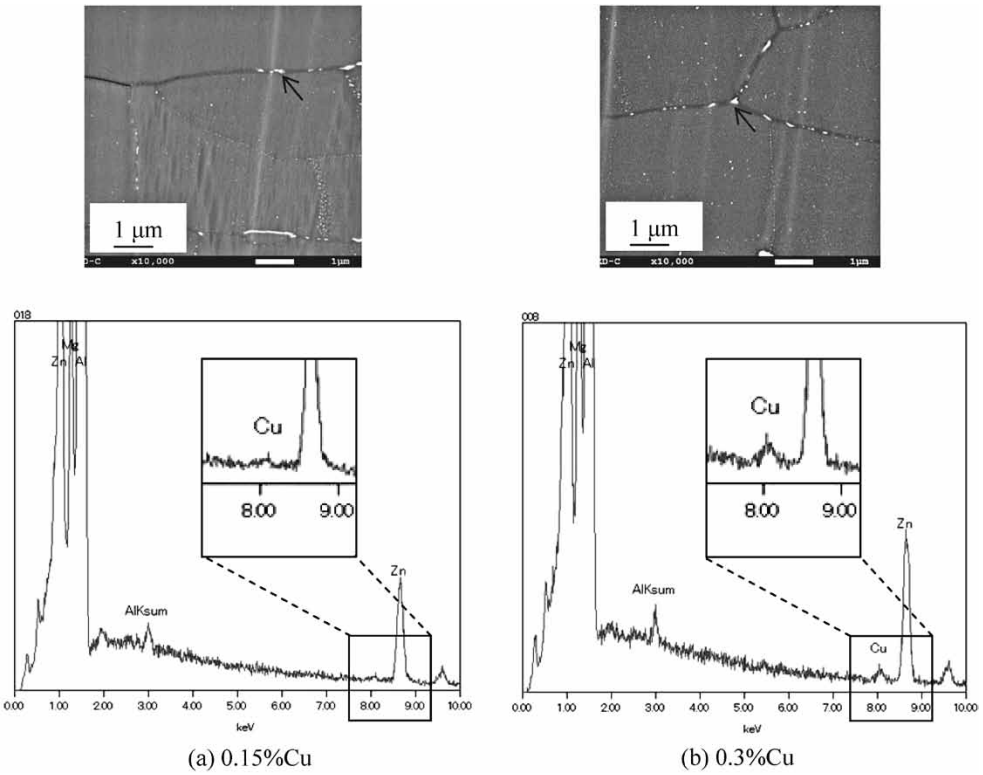


(a) 0.15%Cu (b) 0.3%Cu

Fig. 5 EDX analysis of $MgZn_2$ on grain boundary of Cu-added alloys

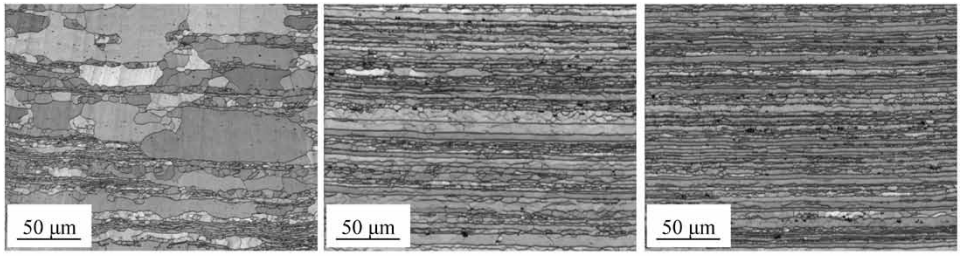


(a) 0.08% Zr (b) 0.14% Zr (c) 0.22% Zr

Fig. 6 Effect of amount of Zr addition on refinement of grain size of alloy extrusion

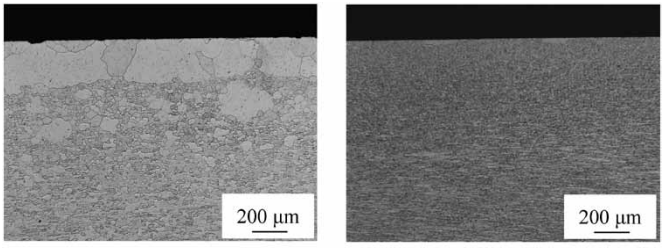


(a) 0.12% Zr (conventional alloy) (b) 0.14% Zr (new alloy)

Fig. 7 Micro structure of bumper surface made of new alloy

the Zr content is 0.14%, a fibrous structure is observed without any recrystallized grain. When the additive amount is at the maximum of 0.22%, the grain boundaries become even narrower and finer. When the additive amount of Zr exceeds 0.2%, there is a concern that the coarse primary crystals of $ZrAl_3$ may occur.[6] Hence, the additive amount of 0.2% at the maximum is considered to be appropriate. Since the microstructure control is influenced by the extrusion ratio, the optimization study was conducted on an actual bumper extrusion.

**Fig. 7** shows the optical micrographs of recrystallization on the surface of a bumper made of the new alloy. The figure compares the surface recrystallization layer of a conventional 7000-series alloy with that of the new alloy, wherein both the alloys have been extruded into the same cross section. In the newly developed alloy, the additive amount of Zr is at the minimum of 0.14%. The conventional alloy has a surface recrystallization layer with a thickness of about 300 $\mu$m. On the other hand, surface recrystallization was hardly observed when Zr was added in the amount of 0.14%. It has been confirmed that coarse surface recrystallization can be suppressed by adding 0.14% or more Zr even in the case of the material extruded to the actual bumper cross section. The practical development has been carried out on the new alloy for bumpers (proof stress 400 MPa) by incorporating the elemental technologies described above.

## Conclusions

This paper has introduced elemental technologies for improving SCC resistance, the technologies adapted in the development of a new high-strength 7000-series alloy with excellent SCC resistance. Currently, the technology for the new alloy, 7K55, with a proof stress of 400MPa class has been established. There are plans to apply this alloy in the mass production of bumpers. In the future, the bar of technology development will be even raised, since even greater strength and improved SCC resistance will be required simultaneously. Hence, we focus on these element technologies and will continue to develop excellent alloys.

## References

1) *Nikkei Automotive*. 2015, Vol.47, February, p.56.
2) H. Hirano. *Journal of Japan Institute of Light Metals*. 1991, Vol.41, No.7, p.482.
3) S. Osaki et al. *Journal of Japan Institute of Light Metals*. 1980, Vol.30, No.12, p.694.
4) S. Osaki et al. *Journal of Japan Institute of Light Metals*. 1975, Vol.25, No.5, p.173.
5) H. Hirano et al. *Journal of the Society of Materials Science, Japan*. 2000, Vol.49, No.1, pp.89-90.
6) Japan Aluminium Association. *Fundamentals of Aluminium Materials and Industrial Technology*. 1985. pp.44-45.

# Application of Aluminum Extrusions to Automotive Parts

Narikazu HASHIMOTO
Aluminum Extrusion & Fabrication Plant, Chofu Works, Aluminum & copper Business

*Recent automobiles have problems of increasing body weight due, for example, to enhanced structural strength for improving collision safety, an increase in the number of parts such as sensors and installation of large batteries. Meanwhile, it is also necessary to respond to the strengthening of fuel-efficiency regulations, and aluminum materials are being increasingly used for the purpose of weight reduction. In particular, aluminum extrusions, which enable complicated cross-sectional shapes to be obtained with relative freedom, are being increasingly applied to automotive parts such as automotive bumper systems and frame members. This paper reports on the current status and future trends of automobile parts adopting aluminum extrusions, with its main focus on a 7000-series alloy that is our main product.*

## Introduction

In recent years, environmental issues, such as global warming due to $CO_2$ emissions and the depletion of fossil fuel oil, have been drawing attention, and efforts are being made in various fields. In the field of automobiles, efforts are being continued to suppress $CO_2$ emissions by improving fuel economy through the development of vehicle bodies with reduced weight, as well as electric vehicles, fuel-cell vehicles, etc. For example, automotive structures with reduced weight are being developed using steel with tensile strength higher than that of conventional steels. Aluminum alloys are also being increasingly used to reduce the weight of structural parts conventionally made of steel. Aluminum alloy is characterized by a low specific gravity approximately one third that of steel and a high specific strength. Its quality and mass production technologies have been proven by their actual applications, in motorcycles, aircraft and Shinkansen cars, for instance.

One of the major advantages of aluminum alloy is that its stock material can be made by hot extrusion, in addition to casting, forging and rolling, the conventional means for producing steel. Wrought aluminum alloys can be hot-extruded into strips with complicated cross-sections relatively freely, and these extrusions are increasingly being used for bumper systems, frame members and other automobile parts.[1), 2)]

This paper introduces the case examples of automotive parts based on aluminum extrusions.

## 1. Background of automotive weight reduction

Regarding automotive fuel economy, there are a number of legal regulations and standards that have been around for many years, and various efforts have been made to achieve it. Since the Kyoto Protocol, adopted at the third meeting of the Conference of Parties to the United Nations Framework Convention on Climate Change in 1997, the fuel economy improvement policy, aiming at reducing $CO_2$ emissions, which are considered to be the cause of global warming, has been one of the major driving forces for regulating fuel economy.

In terms of global trends, Europe and North America are leading the world in strengthening their regulations for automotive fuel economy and curbing $CO_2$ emissions. Fuel economy regulations have also been implemented in Japan and China, and similar regulations are planned for the next decade in the Middle East, Southeast Asia and South America. The corporate average fuel efficiency (CAFE) regulations in North America and the emission standards in Europe are very strict; non-compliance can be fined. **Fig. 1** shows the transition and future target values of fuel economy regulations in Japan, Europe, China and North America from 2015 to 2030.[3)] By 2025, each automobile manufacturer must reduce $CO_2$ emissions to a level lower than 2/3 of the current level. Automotive weight reduction is regarded as the best solution for the current gasoline engines, and weight reduction is essential for vehicle models with a greater production volume. For example, the F-150 (Ford), 760,000 units of which were produced

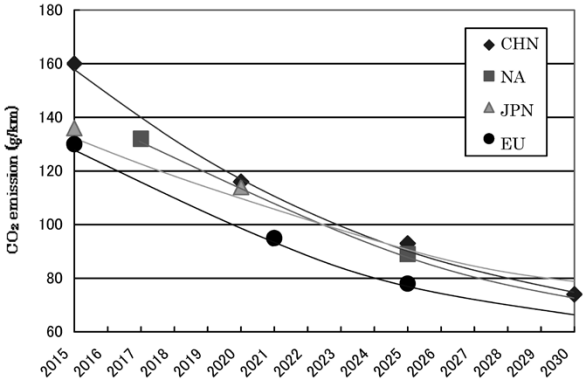


Fig. 1 Transitions of standards being strengthened for fuel economy and $CO_2$ emission (fuel economy converted into $CO_2$ emission)[3)]

in North America in 2014, uses a much greater amount of aluminum than its previous version, and has achieved a weight reduction of approximately 320 kg/unit. The CT-6 (GM) also uses aluminum at an increased rate that accounts for 62% of its vehicle body weight.

Other than these fuel economy regulations, there are the Zero Emission Vehicle (ZEV) program in California[4] and the New Energy Vehicle (NEV) program that China plans to implement after 2020. In these programs, automobile manufacturers are obligated to produce automobiles with no $CO_2$ emissions: electric vehicles and fuel-cell vehicles. Fines are to be imposed if this cannot be achieved, or else the makers must purchase credits from automobile manufacturers like Tesla, which produce only electric vehicles. The state of California stipulates a coefficient called "credit" for each vehicle on the basis of the ZEV types, such as EV, PHEV and HEV, and has established credit criteria to be achieved against their sales volumes. **Fig. 2** shows the credit that will be allocated for environmental vehicles under the ZEV regulation of 2018-2026. It is stipulated that, in 2025, more than 15% of all the vehicles in the state of California must be ones with zero $CO_2$ emissions, such as electric vehicles.

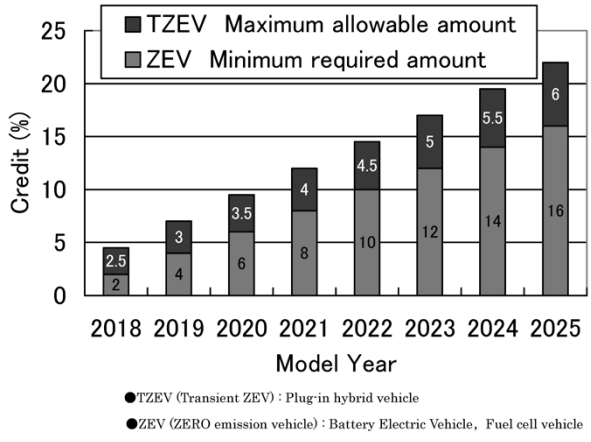


Fig. 2 ZEV credit allocated for LVMs [4]

Against the background described above, the weight reduction needs for automobile structural materials have continued to increase, and serious attempts are being made not only to replace cast iron and steel with higher-strength steel, but to replace them with light-weight materials such as aluminum and FRP.

With the aim of reducing vehicle body weight, Kobe Steel has been working on technologies for both material and processing; these efforts include improving the forming limit of aluminum alloy sheets used for panels and the performance of forged aluminum products. As described in this paper, Kobe Steel has also been promoting the development of high-strength alloys for aluminum extrusions and has launched various automotive safety members made of aluminum extrusions. This paper introduces the product family of such aluminum extrusions.

## 2. Aluminum extrusions

The application of aluminum extrusions has been expanding since the 1960s; it began with extrusions having small cross-sections, such as extruded tubes and multi-hole profiles for engine heat-exchangers. In the 1980s, aluminum alloys in the form of sheets and extruded hollow profiles began to be applied also as the structural materials of vehicle bodies, for which steel had been the main material. As aluminum applications expanded, the reduction of parts-processing costs and cold workability became issues, which have been addressed by improving the chemical compositions and microstructures of the aluminum alloys. Since the 1990s, hydroforming using hydraulic pressure has emerged to make two dimensional extrusions into 3D shapes.

Unlike steel, aluminum can be extruded in complicated cross-sectional shapes with a varying

Table 1 Applications of aluminum alloy extrusions to automotive structures

| Part name | Alloy | Adoption | Required characteristic |
|---|---|---|---|
| Door beam | 7000 Series | 1993～ | Bending strength, Energy absorption |
| Instrument panel reinforce | | 2003～ | Rigidity, Bending strength |
| IPU guard | | 2012～ | Bending strength |
| Seat back bar | | 2015～ | Axial strength |
| Front side rail | | 2016～ | Axial compressibility |
| Locker | | 2016～ | Bending strength |
| Bumper system (Fr. Rr.) | | 1992～ | Bending strength, Energy absorption |
| Side step | 6000 Series | 2007～ | Rigidity |
| Back step | | 2014～ | |
| Knee bolster | | 2005～ | Compressibility in cross section |
| Sub flame | 5000 Series | 2005～ | Rigidity |

wall thickness distribution. With their light weight, they are attracting attention as an effective means of reducing the weight of automobiles.

Kobe Steel began to apply aluminum extrusions to bumper systems and door beams in 1990 and has expanded the application to the structural members of vehicle bodies. **Table 1** summarizes the examples of applications in the past.

## 3. Bumper system

### 3.1 Overview of bumper system

Recent bumper systems mostly have structures as shown in **Fig. 3**.[2] Such a system comprises a thin shell made of resin, providing the outermost portion, and a foam resin placed therein. Inside the foam resin, a metallic bumper reinforcement is attached to the vehicle body via stays (mounting supports). Some types of vehicles have bumper reinforcing material attached directly to the vehicle bodies; however, as the collision safety standards have become more stringent, stay members are often required to have energy absorbing characteristics.[5]

The main role of a bumper system is to receive impact force first and absorb energy through its deformation. Another role is to transfer the energy that cannot be absorbed by bumper beams to stays and rear members. High-strength materials and cross-sectional shapes have been developed to absorb more energy in the light-weight structure. Recently, high-strength alloys (proof stress of 300 MPa or higher) of the 7000-series (Al-Zn-Mg system) alloys have begun to be used,[6] and there are designs of this sort that have realized a weight reduction of approximately 30% compared with the conventional 6000-series (Al-Mg-Si system) alloys. Furthermore, in response to the strengthening of collision standards, some materials with even higher strength (proof stress of 400 MPa or higher) are also being pursued.

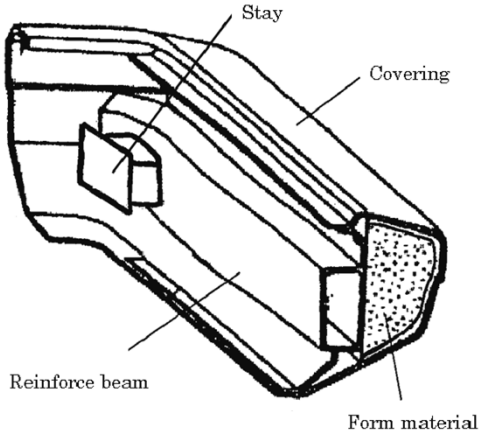

Fig. 3 Example of bumper structure

In addition, the energy absorbing members of bumper systems and the like require aluminum alloys that are immune to crack propagation upon crush. Kobe Steel has revealed that grain size and intragranular precipitates are greatly involved in such crush-cracking resistance[6] and exploits this fact in the material development.

### 3.2 Bumper beam

The cross-section of a bumper beam is based on a square hollow section without, or with one or more partition(s). **Fig. 4**. shows typical cross-sectional shapes. The shapes (curvatures) are diversified, including both-end curves. **Fig. 5** shows an example of overall shape. There is also a need to process variable cross-sections as shown in **Fig. 6** to ensure conformability to the vehicle body design. Variable cross-sections are required to address the issues of smaller overlap between barriers and vehicle bodies at the time of collision testing, as in the case of narrow offset collision.

Bumper systems are also designed to allow the attachment of hooks for towing vehicles. Their designing has become more challenging not only because of the bending compression upon collision, but also because they must incorporate functions against the tension and fatigue caused by towing.

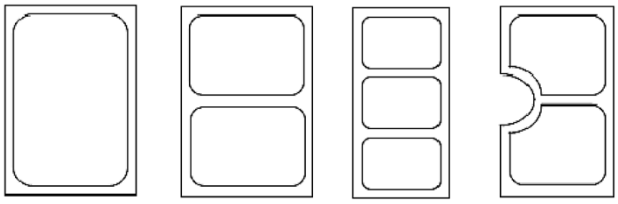
Fig. 4 Typical section type of bumper beam

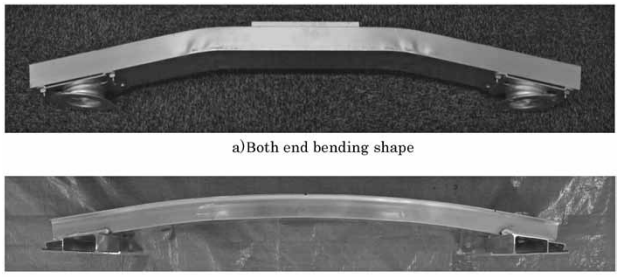

Fig. 5 Typical bending shape of bumper beam


Fig. 6 Both-ends-formed bumper beam

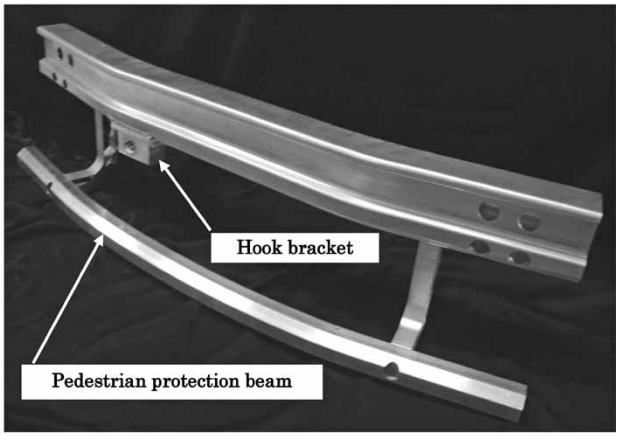

Fig. 7 Example of front bumper system

Lately, another small beam may be attached under a bumper beam for pedestrian protection (**Fig. 7**). The multi-functionalization of bumper systems is expected to be further accelerated in the future.

### 3.3 Bumper stay

With the strengthening of safety standards, bumper stays are required to have energy absorbing characteristics, and their collapse behavior upon collision must be controlled.

Steel stays have box-like shapes, welded together and mechanically fastened to aluminum bumper beams. Welded structures are mainly adopted also for commonly used aluminum stays; however, it is difficult to guarantee their strain and quality after welding, and they become costlier than the ones made of steel.

Against this backdrop, Kobe Steel has developed bumper stays made by a swaging method based on electromagnetic forming.

### 3.4 Bumper system utilizing electromagnetic forming

Electromagnetic forming is a technology for processing subject material and utilizes high magnetic field generated instantaneously when high-voltage, charged in a capacitor with a large capacitance, is discharged at once into an electromagnetic coil. This technology is suitable for forming highly conductive materials such as aluminum and copper. The forming force is applied in a contactless manner, enabling a reduction in the number of dies compared with the press forming method. This technology is expected to enable process reduction, through the simultaneous processing of forming and bonding, and the forming of complex shapes. Hence, research has been conducted to put this technology into practical use.[7)]

On the other hand, the coils are subjected to electromagnetic reaction forces, which are opposite to the forming forces, when forming the subject materials. Hence, increasing the lifetime of coils has been one of the challenges for mass production. Kobe Steel has advanced simulation technologies, such as a newly developed calculation simulator to predict the electromagnetic force distribution during tube expansion.[8)] These technologies have been exploited in--to give one example-- developing a technique to increase the durability of coils and have been applied in the mass production process. As a result, a bumper system using electromagnetically formed stays has been put into practice.[9)]

Conventional steel stays have parts welded together, a process requiring time and money; this method has the drawback of allowing the welding strain being retained in the final products. Each electromagnetically formed stay shown in **Fig. 8** has a body in the form of a hollow circular tube made of aluminum alloy. An end plate is attached to one end of the hollow circular tube, and the circular tube is electromagnetically expanded to swage-couple the plate. The other end of the circular tube is stretch formed during electromagnetic tube expansion, which simultaneously forms a mounting portion.

Although depending on the shapes of parts, the expansion and swaging of aluminum tubes with electromagnetic force eliminates the need for welding and approximately halves the number of processing steps. There is also no welding strain involved, and the number of parts for constructing a stay can be reduced. The electromagnetically formed stay has a mass approximately 1/2 that of the conventional steel stay with equivalent strength performance.

**Fig. 9** shows an example of a bumper system, in which a bumper beam and stays are directly coupled

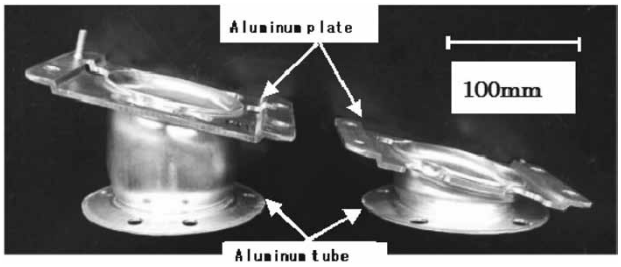

Fig. 8 Bumper stays produced by electro-magnetic forming


Fig. 9 Bumper system combining stay with beam

by electromagnetic forming without a plate. The bumper and stays are integrated by swaging, and further weight reduction has been achieved thanks to the reduced number of parts and the weldless structure.

## 4. Door beam

Door beams are one of the most important safety members for protecting passengers from the lateral collision of automobiles and are currently installed in most automotive doors. **Fig.10** shows an example of door beams.

Each door beam is required to have the ability to absorb energy upon collision and to prevent large deformation of the door. Although the final performance against lateral collision is evaluated by actual vehicle testing, each door beam is usually evaluated by a 3-point bending test with the beam simply supported at both ends. The shapes of door beams are designed with the required characteristics of maximum bending load and amount of energy absorption.

The door beams designed by Kobe Steel have a basic structure with Ⅱ-shaped cross-sections, the shape having the highest bending efficiency. For a given amount of energy absorption, a weight reduction of approximately 30% has been achieved compared with the high-tensile-strength steel pipe currently used.

The recent trends include door beams having large-R shapes to shorten the free running distance upon collision and door beams having crushed ends to improve their attachability to the door inner panel. Application of these processes means that considerable residual stress occurs. Kobe Steel reduces the risk of SCC by controlling the residual stress occurring in the process to lead to practical applications. In addition, door beams require high shape accuracy, and the improvement of processing accuracy has become a subject for the future.

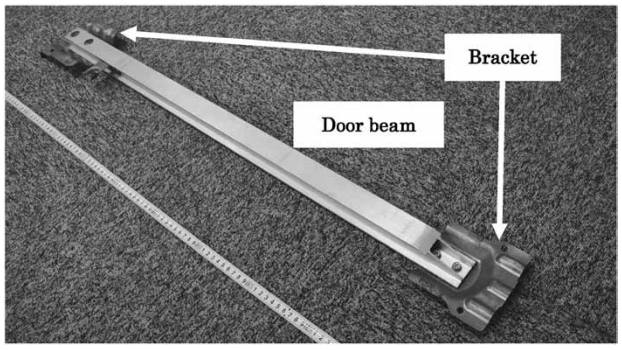

Fig.10 Aluminum door beam

## 5. Vehicle body frame member

The application of aluminum in bumper systems and door beams has been studied for approximately the past 20 years and is on the point of becoming established as a technique for reducing vehicle body weight. Future weight reduction, however, is considered to need the application of high strength aluminum extrusion in vehicle body frames.

The Cadillac CT6, unveiled at Euro Car Body 2015, applies a number of aluminum extrusions.[10] A Kobe Steel 7000-series alloy was adopted for its three components, namely, the crash can, front rail and rocker, which served as elements for reducing the body weight by approximately 100 kg. **Fig.11** shows the application portions.[10] Although 6000-series alloys were sometimes used for vehicle body frames in the past, this was the first case where a 7000-series alloy was applied.[10]

Its application in frame members arranged crosswise in vehicle bodies has also begun, in

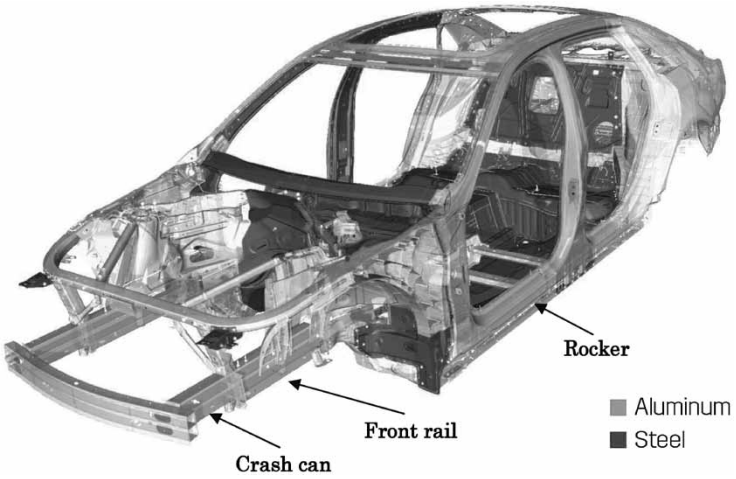

Fig.11 7000-series alloy extrusion applied to frames of production vehicles[10]

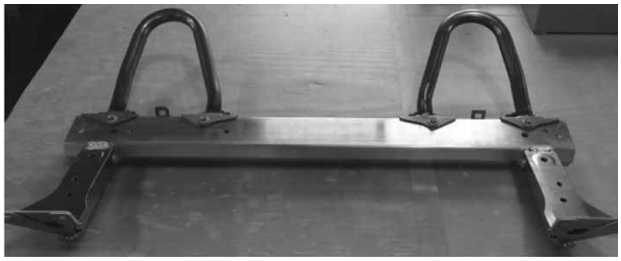

Fig.12 Seat back bar

addition to its use in the frame members of vehicle bodies arranged lengthwise, such as rockers. For example, there is a case in which a 7000-series alloy was applied to a cross member called a seat back bar (**Fig.12**). In addition to its offering more collision safety than the previous model, in which high-tensile-strength steel of 780 MPa was used, this alloy has realized a weight reduction of approximately 1.9 kg.[11)]

As large batteries are installed in vehicles, the battery frames have also begun to be made of aluminum. Kobe Steel has also manufactured a product called a guard frame. This is a type of battery frame and comprises a member for preventing the battery from penetrating into the rear seat upon rear end collision. A 7000-series alloy is adopted to achieve the strength required.

The 7000-series alloys have a strength that is 1.5 times or more higher than that of 6000-series alloy, which is advantageous for weight reduction. However, to further advance the application of 7000-series alloy in the future, it is important to solve issues such as the suppression of SCC by residual stress control, the joining of dissimilar materials and optimization of component structures.

## 6. Exterior parts

Kobe Steel manufactures side steps (**Fig.13**) and back steps for passengers getting on and off; these steps are exterior parts combining aluminum extrusion with resin and iron parts. They have structures in which PP resin is used for the appearance where design is considered to be important, and aluminum extrusions of the 6000-series are used to ensure the rigidity required for the step boards. These steps are mechanically attached by screws and/or clips.

The brackets are made of pressed iron, which is less costly, and the joints of dissimilar materials using aluminum extrusions are treated against electrolytic corrosion using cation painting. Each component requires different performance and has an arrangement of materials most suitable for each characteristic. The side step is an example of

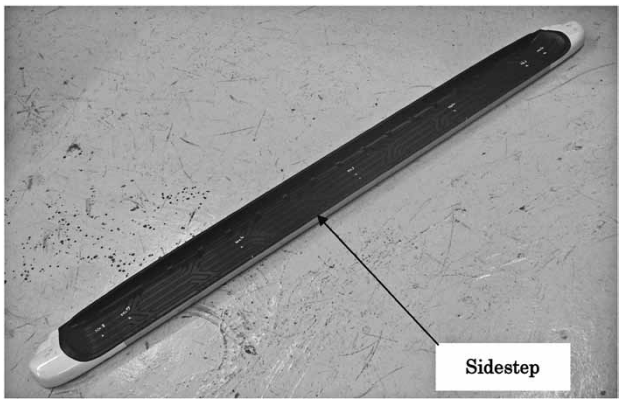


Fig.13 Side step

automotive parts designed on the basis of "specific types used in specific parts."

In order to simultaneously achieve weight reduction and minimum cost, components combining dissimilar materials are expected to increase in the future.

## Conclusions

The 7000-series aluminum extrusions can be made into high-strength materials and be formed into profiles with hollow cross-section. Hence, they are being increasingly valued as a material suitable for high-strength members. On the other hand, they cannot be subjected to complicated forming, unlike the press forming of sheets, and it is difficult in many cases to apply them by simple material replacement, imitating appearance configurations. Thus, it is important to understand the function required for each part first and optimize its shape to suit aluminum extrusion.

As the applications of aluminum extrusions to automotive parts increase in the future, there may be combinations with various materials. Hence, technologies such as joining and surface treatment will become even more important.

Kobe Steel will strive to continue to develop the application of aluminum extrusions by combining the technologies of materials, processing, designing, simulation and bonding of aluminum alloys. Aiming at a further reduction of weight and cost, Kobe Steel will continue to develop one-of-a-kind technologies to please its customers.

## Reference


1) N. Aiura et al. *R&D Kobe Steel Engineering Reports*. 2002, Vol.52, No.3, p.83.
2) T. Hashimura et al. *R&D Kobe Steel Engineering Reports*. 2002, Vol.52, No.3, p.98.
3) T. Tomioka et al. Nikkei Automotive. 2016.3, p.43.
4) *State of California AIR RESOURCES BOARD. PROPOSED*

*2014 AMENDMENTS TO THE ZERO EMISSION VEHICLE REGULATION*. 2014-09-02, p.8.
5) N. Hashimoto et al. *R&D Kobe Steel Engineering Reports*. 2002, Vol.52, No.3, p.99.
6) H. Kawai et al. *Proceedings of the 100th Spring Conference of Japan Institute of Light Metals*. 2001, p.19.
7) Al-Hassani et al. *J. Mech. Eng. Sci*. 1974, Vol.16, No.1, pp.1-9.
8) H. Hosoi et al. *R&D Kobe Steel Engineering Reports*. 2008, Vol.58, No.3, p.87.
9) N. Hashimoto et al. *R&D Kobe Steel Engineering Reports*. 2007, Vol.57, No.2, p.65.
10) *Cadillac CT6 Elevates the Science of Mass Efficiency*. http://media.gm.com/media/us/en/cadillac/racing/news_ archive.detail.html/content/Pages/news/us/en/2015/mar/0313-cadillac-ct6.html, (accessed 2015-03-13).
11) K. Uchibori et al. Mazda Technical Review. 2015, No.32, p.148.